TECHNISCHE
UNIVERSITÄT
WIEN
Vienna University of Technology

INSTITUT FÜR
MECHANIK UND
MECHATRONIK
Mechanics & Mechatronics

DISSERTATION

A real-time railway catenary model for Hardware-in-the-Loop tests

ausgeführt zum Zwecke der Erlangung des akademischen Grades
eines Doktors der technischen Wissenschaften
unter der Leitung von

Ao.Univ.Prof. Dipl.-Ing. Dr.techn. Martin Kozek

am Institut für Mechanik und Mechatronik
Abteilung für Regelungstechnik und Prozessautomatisierung

eingereicht an der Technischen Universität Wien,
Fakultät für Maschinenwesen und Betriebswissenschaften

von

Dipl.-Ing. Emir Talic
Löhnergasse 3/2
1120 Wien

Geboren am 01.03.1986
Matr.Nr.: 0625167

Wien, am 28 Juni 2016

Danksagung

Ich möchte mich bei meiner Familie nach aktueller Größe sortiert bedanken: Emma, Baisa, Eva, Enes, Fuad und Kadira. Ihr habt mich immer unterstützt und bis zum Schluss an mich geglaubt. Hvala vam puno!

Außerdem danke ich all meinen Freunden und Kollegen, insbesondere meinen Betreuern Martin Kozek und Alexander Schirrer, welche diese Zeit ebenfalls zu einer ganz besonderen gemacht haben.

Eidesstattliche Erklärung

Ich erkläre eidesstattlich, dass ich die Arbeit selbständig angefertigt, keine anderen als die angegebenen Hilfsmittel benutzt und alle aus ungedruckten Quellen, gedruckter Literatur oder aus dem Internet im Wortlaut oder im wesentlichen Inhalt übernommenen Formulierungen und Konzepte gemäß den Richtlinien wissenschaftlicher Arbeiten zitiert, durch Fußnoten gekennzeichnet bzw. mit genauer Quellenangabe kenntlich gemacht habe.

Wien, am 28 Juni 2016 Emir Talic

Kurzfassung

Die vorliegende Dissertation stellt die eigenen wissenschaftlichen Beiträge eines Projektes an der Technischen Universität Wien von November 2012 bis Dezember 2015 dar. Die enthaltenen Veröffentlichungen sind im Laufe eines Kooperationsprojektes zwischen dem Institut für Mechanik und Mechatronik (Abteilung für Regelungstechnik und Prozessautomatisierung) und der Firma SIEMENS (ehemals MELECS) als Industriepartner entstanden. Das Projekt wurde von der Österreichischen Forschungsförderungsgesellschaft (FFG Nr. 836449) gefördert.

Effizientes Testen von Bauteilen und Komponenten mit Hilfe von Hardware-in-Loop (HiL) Prüfständen ist in vielen industriellen Gebieten, wie etwa in der Automobil-, Elektronik- und Bahn-Industrie, weit verbreitet. Bei HiL-Prüfständen interagieren die zu testenden eingebetteten Prüflinge (Unit-Under-Test, UUT) mit einem virtuellen Modell mechanisch oder elektrisch über definierte Ein- und Ausgänge. Das ermöglicht realitätsnahe Tests unter Laborbedingungen, erfordert aber echtzeitfähige Modelle. In dieser Arbeit wird ein echtzeitfähiges Oberleitungsmodell vorgestellt, welches erfolgreich an einem innovativen Stromabnehmer-HiL-Prüfstand implementiert wurde.

Das echtzeitfähige Oberleitungsmodell wird mittels mathematischer Modellierung hergeleitet. Da es sich bei einer Oberleitung um ein räumlich ausgedehntes, verteilt-parametrisches System handelt, wird seine Dynamik mit partiellen Differentialgleichungen beschrieben. Diese partiellen Differentialgleichungen, die sogenannten Euler-Bernoulli-Gleichungen, beschreiben die Wellenausbreitung bei der Interaktion mit dem Stromabnehmer. Alle relevanten Komponenten einer Oberleitung, das Tragseil, der Fahrtdraht, die Hänger, welche diese beiden verbinden, und die Masten werden dabei berücksichtigt. Um die Interaktion der Oberleitung mit dem Stromabnehmer effizient zu simulieren, wird der Stromabnehmer fixiert und die Oberleitung über diesen bewegt. Dadurch muss nur die Oberleitung im Umfeld des Stromabnehmers berücksichtigt werden.
Bei einer realen Oberleitung breiten sich die Wellen, welche bei der Oberleitungs-Stromabnehmer-Interaktion entstehen, nahezu ungehindert in und gegen die Fahrtrichtung aus. Um dieses Verhalten einer „unendlich“ ausgedehnten Oberleitung zu simulieren, werden absorbierende Randbedingungen verwendet. Da für die Euler-Bernoulli-Gleichung in der Literatur keine absorbierenden Randbedingen zur Verfügung stehen, wird eine Methode zur Bestimmung von absorbierenden Randbedingungen entwickelt. Die Methode ist nicht ausschließlich auf die Euler-Bernoulli-Gleichung beschränkt, sondern eignet sich auch für andere Gleichungen, welche Wellenausbreitung beschreiben.

Um die Euler-Bernoulli-Gleichung korrekt zu parametrieren, wird eine optimierungsbasierte Identifikationsmethode entwickelt und an einem Seilprüfstand validiert. Die Methode liefert eine gute Übereinstimmung zwischen Modell- und Messdaten und garantiert die numerische Stabilität des Modells, welche für den Einsatz am HiL-Prüfstand unverzichtbar ist.

Abstract

The present PhD Thesis provides my scientific results of a research project at the Vienna University of Technology since November 2012 until December 2015. The publications originated in the course of a cooperation project between the Institute of Mechanics and Mechatronics (Division of Control and Process Automation), and SIEMENS (former MELECS) as industrial partner. The project has been funded by the Austrian Research Promotion Agency (FFG No. 836449).

Hardware-in-the-Loop (HiL) test rigs allow for efficient testing of parts and components and are widely used in automotive, electronics and train industries. The part or component, denoted as unit-under-test is embedded into the HiL test rig and interacts with a virtual model via defined electrical and/or mechanical inputs and outputs. HiL test rigs enable realistic testing under laboratory conditions, however, the (virtual) model has to be executed in real-time. This thesis presents a real-time capable railway catenary model, which has been successfully tested on an innovative HiL pantograph test rig.

The real-time capable catenary model is obtained by mathematical modeling, considering all relevant catenary parts: the carrier and contact wire, the droppers and the masts. The catenary is a spatially distributed system and as such its dynamics are described by coupled partial differential equations (the Euler-Bernoulli beam equations). These equations model the wave propagation arising from the catenary pantograph interaction. To reduce the computational effort a fixed pantograph interacts with a moving catenary. This approach has the advantage that only a limited area of the catenary has to be modeled.
At an actual catenary the waves propagate in an unimpeded manner because of its spatial extension. This "unbounded" domain is modeled for the catenary model by imposing absorbing boundary conditions. This boundary conditions have not been investigated for Euler-Bernoulli beam before. Because of that a optimization based methodology is developed to determine well-performing and stable absorbing boundary conditions. This methodology is generic and can be used for partial differential equations with wave propagation effects.
To identify the physical parameters of a Euler-Bernoulli beam, a multi-objective optimization methodology is developed and verified on an wire test rig. Stability is guaranteed for the resulting numerical model, which is crucial for HiL applications.

Contents

List of Figures

Chapter 1

Introductory Chapter

1.1 Motivation & Problem Statement

Modern high-speed passenger trains are traveling at speeds of $250\,\mathrm{km\,h^{-1}}$ and beyond. Their efficiency in connecting large cities led to massive investments especially in Europe and East Asia. Compared to air transport high-speed trains achieve a share about 80 % of passengers for travelling times below 2.5 hours. In total 1.6 billion passengers are traveling by high-speed trains annually [1].
Higher cruising velocities are also leading to higher requirements for trains, train parts and railway infrastructure as the catenary. To test railway parts such as the current collector (pantograph) actual test rides are expensive and do not allow short development cycles. A cost-effective solution are Hardware-in-the-Loop (HiL) test beds. These test beds allow to investigate the unit-under-test (UUT), here the pantograph, under close-to-reality conditions. To perform realistic test runs the catenary dynamics is emulated by the HiL test bed and dynamically interacting with the pantograph. This setup enables reproducible test runs in a laboratory environment. However, a crucial part for this approach is the use of a realistic catenary model which is particular challenging because:

- A catenary is a distributed parameter system and is modeled mathematically by coupled partial differential equations (PDEs).
- For physical trustworthiness these PDEs have to parametrized correctly.
- Efficient numerical implementation and reduction methods are needed to enable real-time computation.

The derivation and the implementation of such a real-time capable catenary model is the topic of this thesis.

1.2 Goals

The overall goal is the development and the implementation of a real-time capable catenary model on an actual HiL test bed and was achieved by

1. modeling an actual catenary setup mathematically,
2. parameterizing the catenary model with physical meaningful parameters, and
3. applying reduction methods to enhance the execution time of the model.

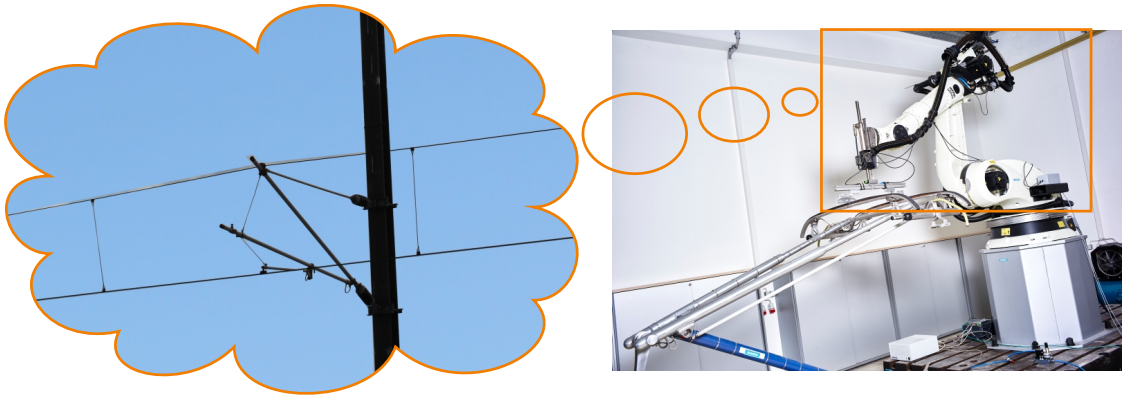

Figure 1.1: Principle of catenary emulation on Hardware-in-the-Loop (HiL) test rig. The robot arm and the linear drive mimic the catenary dynamics. The pantograph as unit-under-test (UUT) "feels" the emulated catenary.

The mechanical HiL test bed is displayed in the right part of Fig. 1.1. It consists of a robot arm and a linear drive. The linear drive is used to excite the pantograph with catenary's dynamics (symbolically displayed in the left part of Fig. 1.1). The derivation and emulation of the real-time catenary model, and its interaction with the pantograph are published in Ref. [2] (Publication C). This goal is achieved step-wise by first modeling the catenary physical setup mathematically (see top left part of Fig. 1.2). Its implementation adopted from Ref. [3] and is performed in efficient and flexible way [4]. The resulting model is not real-time capable, but allows comparison with literature and standards as the EN50318 [5]. As a second step a suitable identification method was developed to parametrize the model with realistic parameters (see top right part of Fig. 1.2). Therefore, a multi-objective optimization based identification methodology was developed and validated with simulation and measurement data (see [6] or Publication A). Finally, the real-time capability is obtained using a different reference system (pantograph-fixed coordinates) formulation and by applying absorbing layers/boundary conditions. This special boundary treatment is needed to avoid spurious reflections. A optimization based determination of absorbing boundary condition is published in Ref. [7] (Publication B)

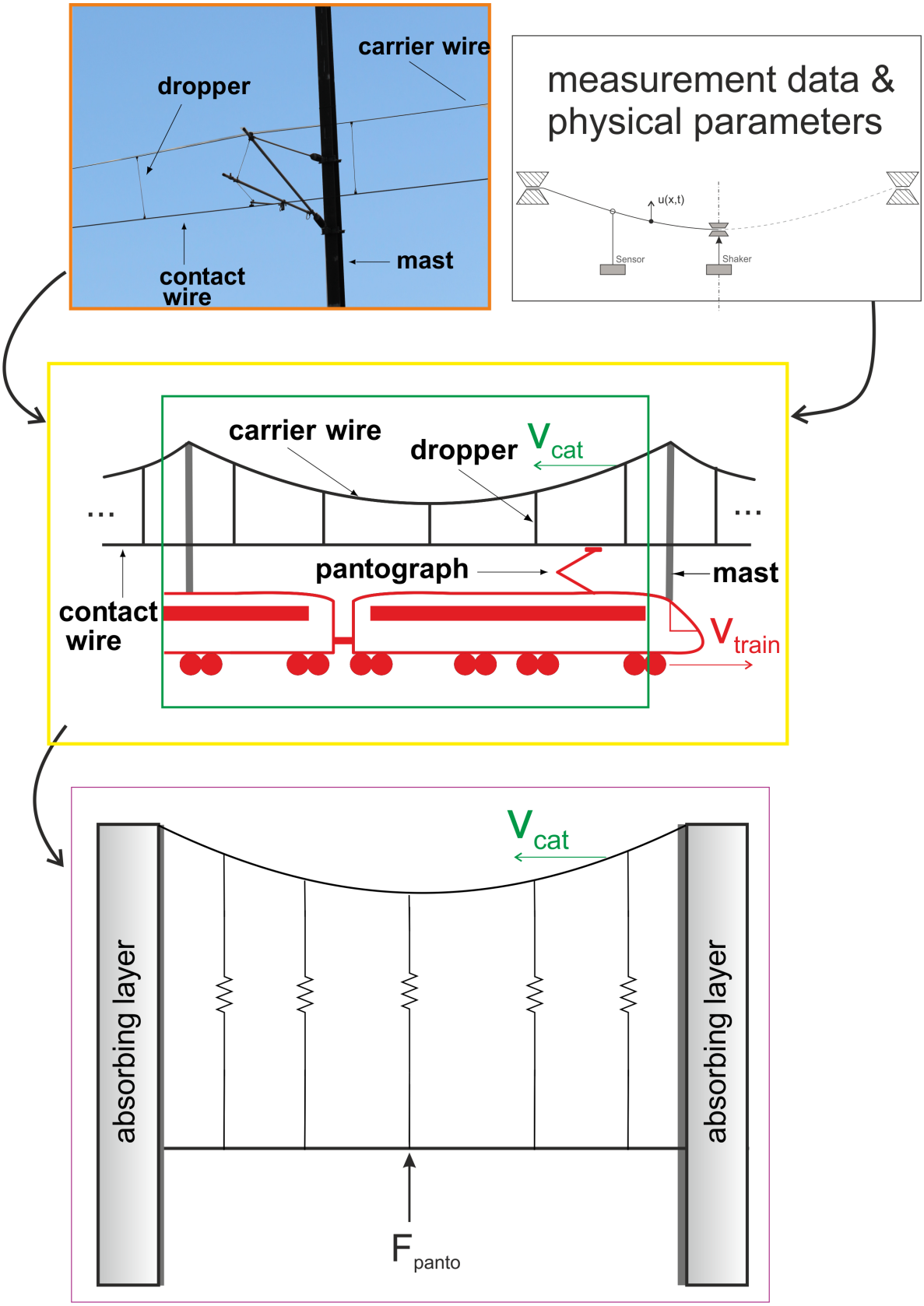

Figure 1.2: Major steps for achieving a real-time capable catenary model: modeling, identification and reduction

1.3 Methodology

The major steps of the methodology: 1) modelling, 2) identification and 3) reduction as visualized in Fig. 1.2 will be explained in the following subsections.

1.3.1 Modelling

Modelling a catenary mathematically leads to a distributed parameter system which is described by PDEs.
An actual catenary set-up is displayed in the upper left part of Fig. 1.2. This figure shows that the catenary consists of wires, droppers and masts. The upper wire, called carrier wire, is directly attached to the masts. Whereas the lower wire, called contact wire, is connected to the carrier wire via droppers. Both wires are modelled as Euler-Bernoulli beams (EBBs) under axial load, which are considered to be linear, with constant parameters.
As the droppers support the contact wire only if they are under tension, the structure of the catenary dynamics varies if a dropper is lifted up by the pantograph. This effect caused by dropper slackening leads to a variable structure system and its behaviour is described by additional algebraic constraints. Together with the EBB equations the resulting system is also denoted as partial differential algebraic equation (PDAE) [3]. This class of equations needs special treatment when solving. Several numerical approaches have been published based on spectral [8], finite element [3, 8], finite volume and finite differences (FD) approximations [3, 4, 9]. A comparison of a spectral Fourier series and an FD approximation can be found in [4].

Coordinate formulation

In this thesis two different modelling approaches by means of coordinate formulations will be pursued: a pantograph/train fixed and a catenary-fixed coordinate formulation. In the catenary-fixed formulation the catenary is fixed in space while the pantograph is moving along the catenary with the velocity v_{train} (see Fig. 1.3). This formation has the advantage that is a standard/state-of-the-art formulation and several solutions are available in literature [3, 4, 8, 9]. To simulate long runs a sufficient large number of catenary spans has to be modeled. Reflections at the boundaries are avoided by extending the computational domain. Simple clamping boundary conditions can be used. The elongation of the computational domain can be performed automatically [4, 9, 10] however, the computational effort rises. Consequently, this formulation is only partly suitable for real-time applications but allows insights into the catenary's dynamic behavior and can be used as a reference.
In the pantograph/train-fixed formulation the pantograph is fixed in space while the catenary is moving with the velocity v_{cat} (see Fig. 1.3; inner/green box). This formulation allows to take advantage of the periodical structure of the catenary. The dropper(s)

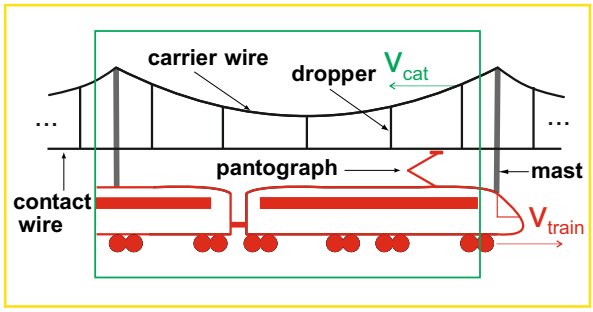

Figure 1.3: Catenary modelling: catenary-fixed ($v_{\text{cat}} = 0, v_{\text{train}} \neq 0$) vs. pantograph/train-fixed coordinate ($v_{\text{cat}} \neq 0, v_{\text{train}} = 0$) formulation.

and mast(s) are entering and leaving the computational domain periodically. In addition, only a limited domain around the pantograph must be modeled and simulated. This ensures fast computation. Additionally, the domain size and simulation duration can be chosen independently. However, the limited domain size leads to spurious reflections if standard (e.g. clamping) boundary conditions are used. To avoid numeric artifacts (i.e. reflections) special absorbing boundary conditions (ABCs) or absorbing layers are used. For that reason ABCs for the EBB equation under axial load have been developed (see [7] or Publication B).
A derivation of the coordinate transformation of the pantograph in a catenary-fixed formulation can be found in [11]. In the following section, the discretization in space and time of the EBB equations by means of FD approximation will be explained. This methodology transforms the PDE into a set of algebraic equations.

Discretization by Finite Differences

The EBB equation used for the catenary modeling is a one-dimensional PDE

$$\rho A \frac{\partial^2 u}{\partial t^2} + d_v \frac{\partial u}{\partial t} = -EI \frac{\partial^4 u}{\partial x^4} + T \frac{\partial^2 u}{\partial x^2} + f(x,t) \tag{1.1}$$

and its solution $u(x,t)$ describes the vertical displacement as a function of time t and space x (see Fig. 1.4). The constant parameters are the bending stiffness EI, the axial load T, the mass per unit length ρA, the viscous damping d_v and the distributed force $f(x,t)$. An analytic solution of (1.1) may only be obtained for special cases if possible at all. For that reason in this thesis FD approximations are used to compute the solution $u(x,t)$ numerically.
The numerical solution is obtained by:

1. discretizing the spatial and temporal derivatives by (central second order) FDs [12] on uniform grid meshes $t = [0, \Delta t, \ldots, N\Delta t]$, $x = [0, \Delta x, \ldots, K\Delta x]$, $N, K \in \mathbb{N}$ and

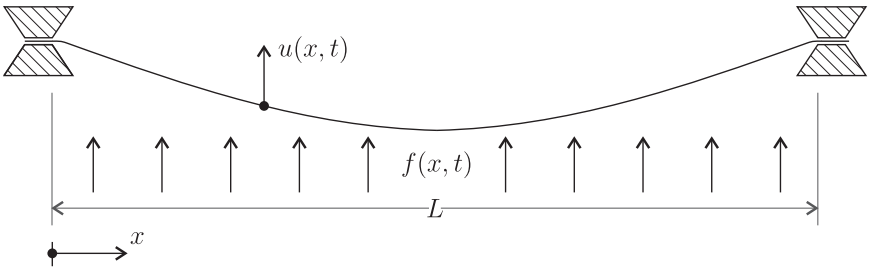

Fig. 1. Euler–Bernoulli beam with clamped–clamped boundary conditions.

Figure 1.4: Euler-Bernoulli beam with clamped boundary conditions: The solution $u(x,t)$ of this distributed parameter system is a function of space x and time t.

2. rewriting the equation to be explicit in $u_k^{n+1} := u(k\Delta x, (n+1)\Delta t)$, $k = 0, \ldots, K$.

The quantities Δt and Δx denote the temporal and spatial mesh size, respectively and N and K are the number of grid points. Unknown future displacement values are calculated as

$$u_k^{n+1} = \mathbf{f}(\mathbf{u}_k^n, \mathbf{u}_k^{n-1}, \ldots, \mathbf{u}^{n-N_t-2}) \tag{1.2}$$

with

$$\mathbf{u}_k^n = \left[u_{k-N_x}^n, \ldots, u_{k+N_x}^n\right]^{\mathrm{T}}$$

and $N_t, N_x \in \mathbb{N}$. The pattern of these relations of points in the space-time grid (1.2) is called stencil and the corresponding coefficients are denoted as stencil coefficients [7]. An illustration of the geometrical time-space-relation is given in Fig. 1.5.

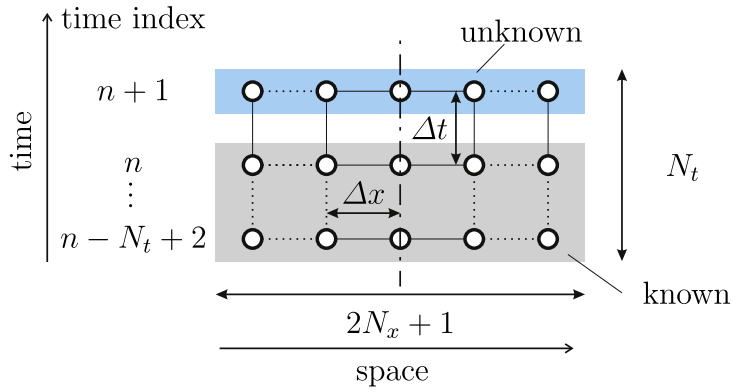

Figure 1.5: General symmetric interior stencil structure

In the actual case of the EBB equation with constant physical parameters the relation (1.2) is linear with constant stencil coefficients. A detailed derivation of (1.2) can be found in Publication A.
To obtain realistic results the discretized PDE has to be parametrized with meaningful physical parameters.

1.3.2 Identification

An MOO based identification is used to identify all parameters (the bending stiffness EI, the axial load T, the material damping d_{mat} and viscous damping d_v) simultaneously by solving the optimization problem

$$\min_{\mathbf{p}} \mathbf{J}(\mathbf{p}) = \min_{\mathbf{p}} \left[J_{\text{perf}}(\mathbf{p}), J_{\text{stab}}(\mathbf{p}) \right], \, \mathbf{p} \in D, \, \mathbf{J} \in C, \tag{1.3}$$

where J_{perf} and J_{stab} are the performance and stability objectives, respectively, D is the decision space, C is the criterion space and $\mathbf{p} = [EI, T, d_{mat}, d_v]$ is the parameter vector. A more detailed discussion on MOO is given in following section.

Multi-objective optimization

Typically, MOO problems are formulated when at least two conflicting objective such as performance and stability are traded against each other. An MOO problem can also be transformed into a single objective optimization (SOO) by choosing a relative weighting of the objectives before the optimization run (a-priori formulation of preferences/importance). Varying these relative weights, an approximation of the Pareto front is obtained. In this thesis the MOO problem solved is directly using an MOO genetic algorithm [13]. This method is categorized as a-posteriori formulation of preferences and allows to generate approximations of the Pareto front without choosing a specific weighting. A detailed review on MOO is given e.g. in [14].
Here, the MOO problem is defined for a single performance objective. For an arbitrary number of performance objectives the interested reader is referred to Publication A.
During the optimization run the MOO objective function $\mathbf{J}(\mathbf{p}) : D \rightarrow C$ from (1.3) projects the vectors of $\mathbf{p}$ from the decision space D to the criterion space C as displayed in Fig. 1.6. The stability and performance objective value of every parameter set are then compared. If a parameter vector $\mathbf{p}^* \neq \mathbf{p}$ exits that fulfills

1. $\mathbf{J}(\mathbf{p}) \leq \mathbf{J}(\mathbf{p}^*)$
2. $J_i(\mathbf{p}) < J_i(\mathbf{p}^*)$ for at least one objective function

then this vector is called Pareto optimal. All Pareto optimal vectors form the Pareto front which represents the best possible trade-off solutions.

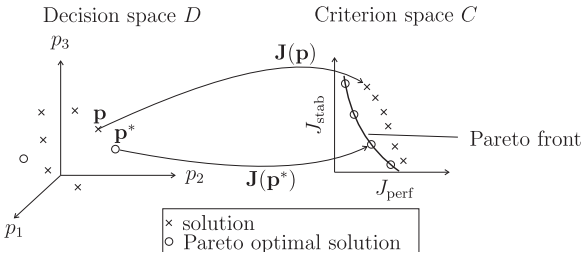

Figure 1.6: Multi-objective optimization: Two objective values are evaluated and compared for each parameter set. Pareto optimal solution $\mathbf{p}^*$ dominates a solution $\mathbf{p}$ for at least one objective value, while it is at least equal for the other objective value. All Pareto optimal solutions form the Pareto front.

Identifiability

The necessary condition for unique identifiability of a distributed parameter system such as the EBB equation is outlined in this section. For constant parameters $\mathbf{p}$ the equation (1.2) becomes linear. Collecting the displacement values u_k^n as state vector

$$\mathbf{x}^n = \begin{bmatrix} u_0^n \\ \vdots \\ u_K^n \end{bmatrix}$$

a linear time-invariant state-space system is obtained

$$\begin{aligned} \mathbf{x}^{n+1} &= \mathbf{A}\mathbf{x}^n + \mathbf{B}\mathbf{f}^n \\ \mathbf{y}^n &= \mathbf{C}\mathbf{x}^n \,. \end{aligned} \tag{1.4}$$

with parameter-dependent system matrices $\mathbf{A} = \mathbf{A}(\mathbf{p})$, $\mathbf{B} = \mathbf{B}(\mathbf{p})$ and $\mathbf{C} = \mathbf{C}(\mathbf{p})$, the state vector $\mathbf{x}$, the system output $\mathbf{y}$. By computing the output error of the model (1.4)

$$\mathbf{e}^n(\mathbf{p}) = \mathbf{y}^n(\mathbf{p}) - \hat{\mathbf{y}}^n \,, \tag{1.5}$$

with the actual measurement sequence $\hat{\mathbf{y}}^n$ of length N_t^{seq}, the Fisher information matrix can be defined as

$$\mathcal{I} = \sum_{n=0}^{N_t^{\text{seq}}} \frac{\mathrm{d}\mathbf{e}^n(\mathbf{p})}{\mathrm{d}\mathbf{p}} \left(\frac{\mathrm{d}\mathbf{e}^n(\mathbf{p})}{\mathrm{d}\mathbf{p}} \right)^{\mathrm{T}} . \tag{1.6}$$

In order to obtain a unique solution the Fisher Information Matrix $\mathcal{I}$ has to be non-singular. Furthermore, by decomposing to $\mathcal{I} = \boldsymbol{\psi}^{\mathrm{T}}\boldsymbol{\psi}$ and $\boldsymbol{\psi} = \mathbf{U}\mathbf{S}\mathbf{V}^*$, more information, such as parameter sensitivity and non-identifiability of a particular parameter can be calculated and determined, respectively.

Remark 1 *The performance objective can be directly defined using the output error* (1.5) *and Definition 2 given in Publication B. Therefore, it is omitted in this introductory chapter.*

Stability objective

The stability objective proposed in Publication A is defined as the largest magnitude of the temporal growth factor $\tau_{\max}$. Before the objective is explained two definitions are needed.

Definition 1 *The **traveling wave solution** is defined as*

$$u_k^n = \exp(In\omega_t\Delta t)\exp(Ik\omega_x\Delta x) = \tau^n\kappa^k \tag{1.7}$$

where τ is the temporal growth factor, $\omega_t \in \mathbb{C}$ is the temporal frequency, $\omega_x \in \mathbb{C}$ is the spatial frequency and I is imaginary unit.

Definition 2 *The **discrete dispersion relation (DDR)**[15] is defined as*

$$f(\tau(\omega_t\Delta t), \kappa(\omega\Delta x)) = 0\,. \tag{1.8}$$

and is derived by inserting the traveling wave solution (1.7) *into* (1.2)*.*

The DDR (1.8) describes the relation of the temporal and spatial frequencies of a discretized PDE and allows only specific combinations of (ω_t, ω_x).
The computation of the stability objective value is be performed in three steps:

1. Compute the DDR for a parameter set $\mathbf{p}$ following Definition 2 and manipulate (1.8) such that it becomes a polynomial of τ:

$$\sum_i a_i(\mathbf{p}, \omega_x\Delta x)\tau^i = 0\,. \tag{1.9}$$

2. Compute the solution of the polynomial $\tau(\omega_x\Delta x)$ for $\omega_x\Delta x \in [0, \pi]$ and

3. evaluate the stability objective as

$$J_{\text{stab}}(\mathbf{p}) = \tau_{\max} = \max_{\omega_x\Delta x} |\tau| \;, \forall\omega_x\Delta x \in [0, \pi]\;. \tag{1.10}$$

For stable system (1.4) the condition $\tau_{\max} < 1$ is fulfilled.

Remark 2 *It is noted that $\tau_{\max} < 1$ can be checked for real or complex valued polynomials efficiently using Jury [16] or Bistritz criterion [17], respectively, without computing the roots of* (1.9) *explicitly.*

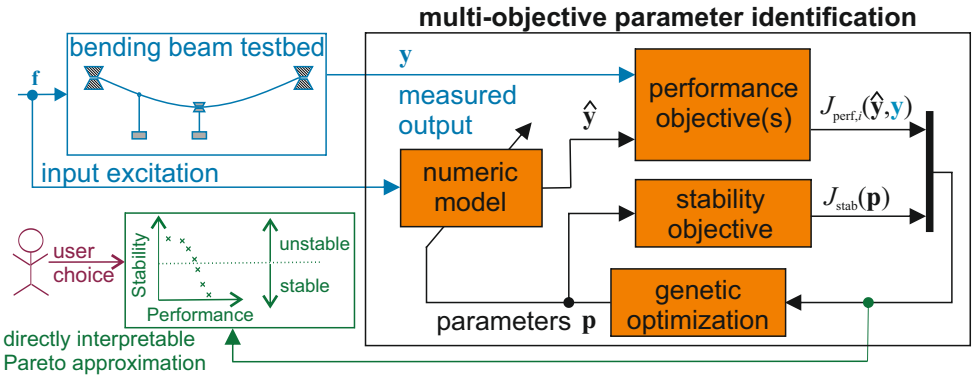

Figure 1.7: MOO identification methodology

MOO identification methodology

The major steps in MOO identification methodology are explained as follows (see Figure 1.7): First, suitable identification data (input excitation $\mathbf{f}$ and output measurement $\mathbf{y}$) have to be recorded or obtained by simulation. Then the numeric model is parametrized by a (initial) parameter vector $\mathbf{p}$. A simulation with the input excitation is used to generate the model output $\hat{\mathbf{y}}(\mathbf{p})$. The stability objective is evaluated using the parameter vector directly and the performance objective comparing $\mathbf{y}$ and $\hat{\mathbf{y}}(\mathbf{p})$ in an OE-sense (see (1.5)). Based on these objective values the genetic optimization generates a new parameter vector and repeats the procedure. The Parto optimal parameter vectors are visualized in the stability-performance-diagram. The optimization is either stopped by the user or by a pre-defined termination condition.

1.3.3 Reduction

A significant reduction of the system size can be achieved by changing the coordinate formulation from catenary- to pantograph-fixed coordinates as displayed in Figure 1.3. As described in Section 1.3.1 this formulation provides the advantage that only small parts of the catenary have to be simulated. However, so-called absorbing boundary conditions are needed. These are used to avoid spurious reflections at the boundaries and have not been developed for the EBB under axial load before. The methodology is presented in the following section.

Absorbing boundary conditions for the EBB under axial load

The major idea is that a boundary stencil (see Figure 1.8) with the ABC stencil coefficients ${}_i\mu_j^{\mathrm{T}}$ propagates a traveling wave solution (1.7) in the same way as an interior stencil (see Figure 1.5). If the wave propagation is exactly reproduced by the boundary stencil, no reflection will occur which leads to an unbounded domain solution. However, perfectly absorbing ABCs can only be derived in special cases, see e.g. [15, 18].

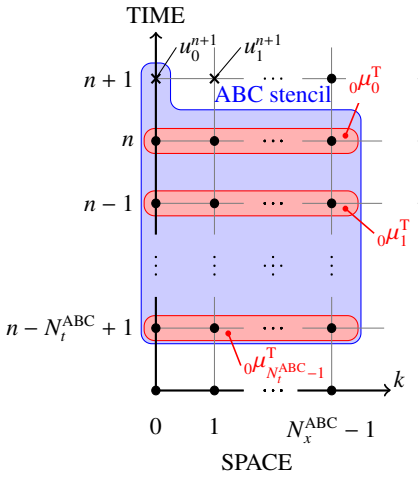

Figure 1.8: The generic ABC stencil

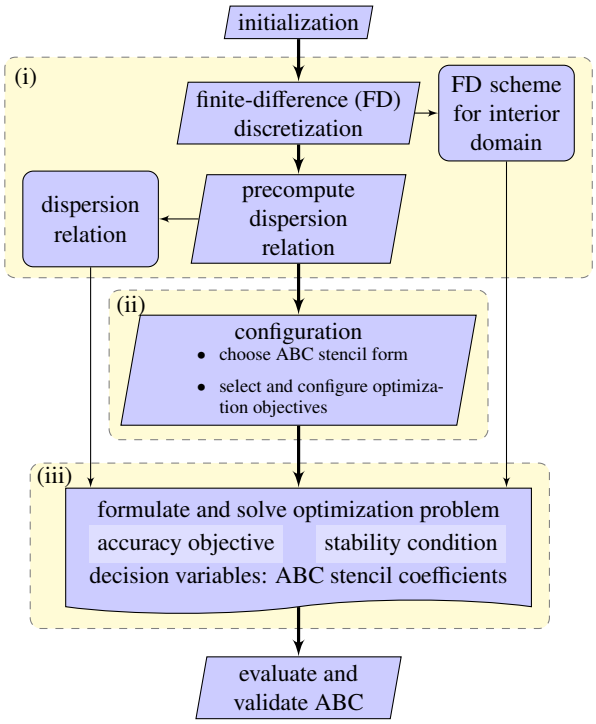

Figure 1.9: Optimization based methodology for ABC stencil determination

Here, an optimization based determination of the ABC stencil coefficients is used. The methodology is displayed in Figure 1.8 .
In step (i) the EBB (1.1) (for $d_v = 0$) is discretized leading to the equation (1.2) (denoted as "FD scheme for interior domain" in Figure 1.8). By inserting the travelling wave solution (1.7) into (1.2) the DDR (1.8) is obtained and stored for the evaluation of the performance objectives. In step (ii) the ABC stencil form is chosen by defining N_t^{ABC} and N_x^{ABC}. Then the optimization is set up by choosing one of the performance objectives and the stability objective (proposed in the next paragraph). In step (iii) the MOO is performed and the results are the ABC stencil coefficients ${}_i\mu_j^{\mathrm{T}}$.

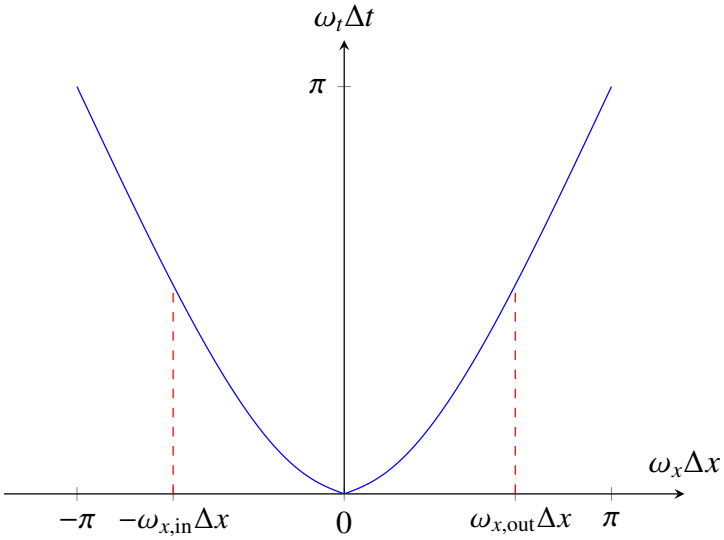

Figure 1.10: DDR for the parameters: $EI = 150$, $T = 15000$ and $\rho A = 1$.

In Figure 1.10 the DDR of an EBB equation with typical parameters of a catenary contact wire is illustrated. As one can clearly see, the DDR of an EBB is a non-linear relation of the spatial and temporal frequencies. Because of that, higher frequency waves are traveling faster than lower frequency ones which is a typical property of the EBB. This makes the development of ABCs particular challenging compared to the wave equation (obtained from (1.1) for $EI = 0$) which has a linear DDR.
For the left-sided ABC stencil (see Figure 1.8) the DDR has two branches. The branch $\omega_t\Delta t(\omega_x\Delta x)$ with the same sign for $\omega_x\Delta x$ and $\omega_t\Delta t$ represents the outgoing and that with a different sign the incoming wave parts[1].

[1]This corresponds to negative and positive group velocity v_{group}, respectively

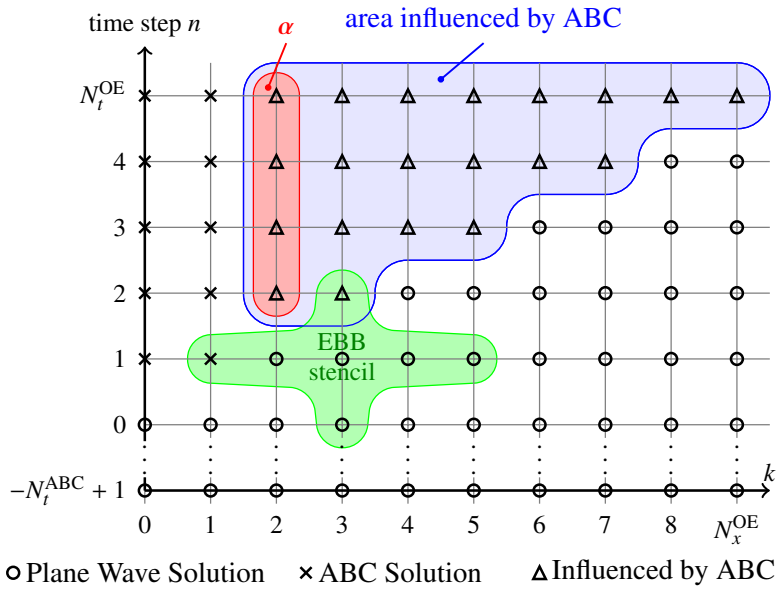

Figure 1.11: OE-based performance objective

Stability and Performance objectives

The **stability objective** is obtained by directly evaluating the eigenvalues of the state space representation of the FD-discretized EBB equation (1.4) with ABCs in place. To render the system stable all eigenvalues must lie be inside the unit circle. Thus, the eigenvalue with the largest magnitude is crucial for stability and is used as stability objective value.
The first **performance objective** is based on the **reflection coefficient** [19]. Starting with a pre-computed and stored DDR the reflection coefficient is computed as follows:

1. Transform the discrete dispersion relation (1.8) into the form

$$B_k(\tau,\kappa)u_k^{n+1} = 0\,, \quad k = 0,\ldots,N_{\mathrm{ABC}}$$

   where N_{ABC} is the number of boundary points.

2. Evaluate $B_k(\tau,\kappa)$ for κ_{in} and κ_{out} and compute the reflection coefficient

$$R_k = -B_k(\tau,\kappa_{\mathrm{out}})/B_k(\tau,\kappa_{\mathrm{in}})$$

Perfect absorption is given for $R_k = 0$ and any $B_k(\tau,\kappa_{\mathrm{in}}) \neq 0$.
The second **performance objective** evaluates the traveling wave solution in an **output error** (OE) sense. The cumulated deviation is used as performance objective value. Therefor, the traveling wave solution is simulated on a small test domain with ABCs in place and compared to that of the unbounded domain (directly available from (1.8)).

Figure 1.11 sketches the concept for an EBB explicit interior stencil (green). Each grid point u_n^k is first initialized with (1.8) (marked by $\circ$). For $n > 0$ the ABC stencil is used to compute the boundary point solutions (marked by $\times$). For the remaining grid points ($k > 2$) the interior stencil is evaluated. Simulating forward in time, some interior grid points are influenced by the ABC (blue area; marked by $\triangle$). The deviation of the solution using ABC from the traveling wave solution (1.7) in the red area is evaluated for pre-stored values of the DDR.

Results

The absorbing properties of the ABCs have been tested using the set-up depicted in Figure 1.12a for several time instants $t = 0 < T_1 < \ldots < T_8$. On the left side of the computational domain ABCs are applied, whereas on the right clamping boundary conditions are used. Clamping boundary conditions are worst possible ABCs and lead to total reflection. The computational results are shown in Figure 1.12b. As displayed, the initial wavelet ($t = 0$) first splits up into left- and right-traveling packets ($t = T_1, T_2$). The higher frequency waves travel faster than the lower frequency waves. This is due to the non-linear DDR (see Figure 1.10). At $x = 0$ the ABC absorbs the incoming wave packages nearly perfectly ($t = T_3, T_4$). At the clamped end of the EBB ($x = 100\,\mathrm{m}$) the wave package is completely reflected and travels back towards the ABC ($t = T_5, T_6, T_7$). At time instant $t = T_8$ the reflected part is absorbed by the ABC and the remaining reflections from ABC imperfections are very small.
The presented ABC showed very good results for the non-moving EBB equation ('catenary-fixed formulation'). For the pantograph-fixed formulation the absorbing layer presented in [20] led to better results. Additionally, they are very robust against droppers entering and leaving the computational domain. For that reason the best available solution [20] is used in adopted form for the real-time catenary.

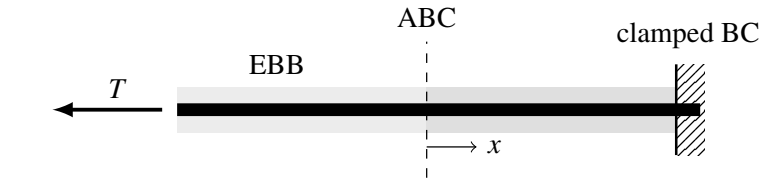

(a)

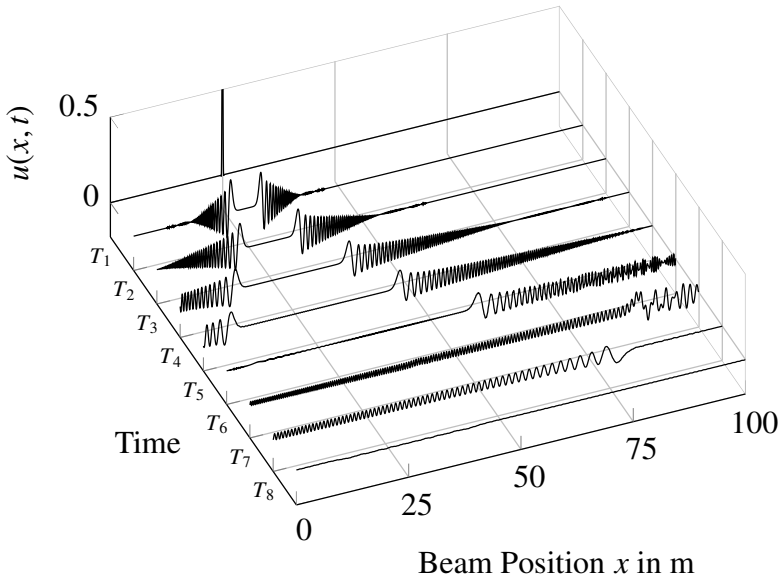

(b)

Figure 1.12: Validation of the absorption properties: (a) ABC test set-up. (b) Initial excitement leads to two wave packets (right- and left-wards traveling), which are reflected or absorbed by the clamped BC or ABC, respectively.

Real-time catenary model

The real-time catenary model displayed in Figure 1.13 is obtained by

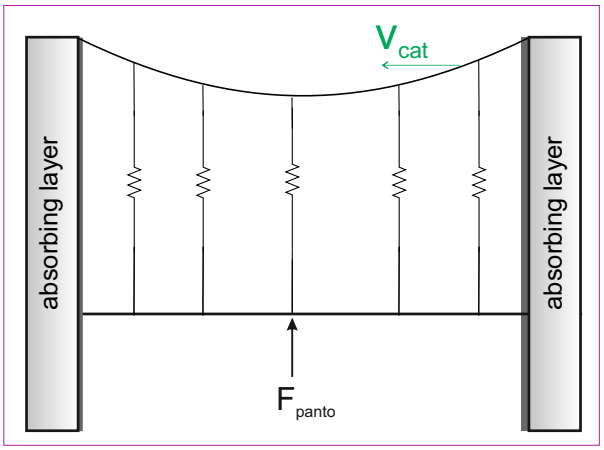

Figure 1.13: Real-time catenary model: utilizes pantograph-fixed coordinate formulation, droppers as linear springs and absorbing layers.

1. using the pantograph-fixed coordinate formulation (see Section 1.3.1 and [2, 11]),
2. modeling the droppers as linear springs,
3. employing a Crank-Nicolson-type [21] implicit integration formulation of the dropper stiffness terms
4. and applying absorbing layers [20].

By modeling droppers as linear springs, the catenary model becomes linear. This permits to pre-compute the system matrices $\mathbf{A}$, $\mathbf{B}$ and $\mathbf{C}$ (see (1.4)) and, thus, decreases computational demand significantly. To retain the system stability especially for high dropper stiffness coefficients an implicit Crank-Nicolson-type integration is used. This leads to a linear periodically time-varying system

$$\mathbf{A}^n = \mathbf{A}^{n+N_{\text{per}}}, \quad \mathbf{B}^n = \mathbf{B}^{n+N_{\text{per}}},$$

where N_{per} is the periodicity of the model. The absorbing layers are adopted from [20] and used instead of the proposed ABCs to avoid shocks imposed by droppers when they are entering or leaving the computational domain. Furthermore, these layers are easier to parametrize and better suited for the pantograph-fixed coordinate formulation.
The real-time catenary model is validated by comparing it with a catenary-fixed model. The results of this comparison is displayed in Figure 1.14 for the velocity $v_{\text{cat}} = 60\,\text{m/s}$ and a catenary span length of 60 m. The remaining physical and simulation parame-

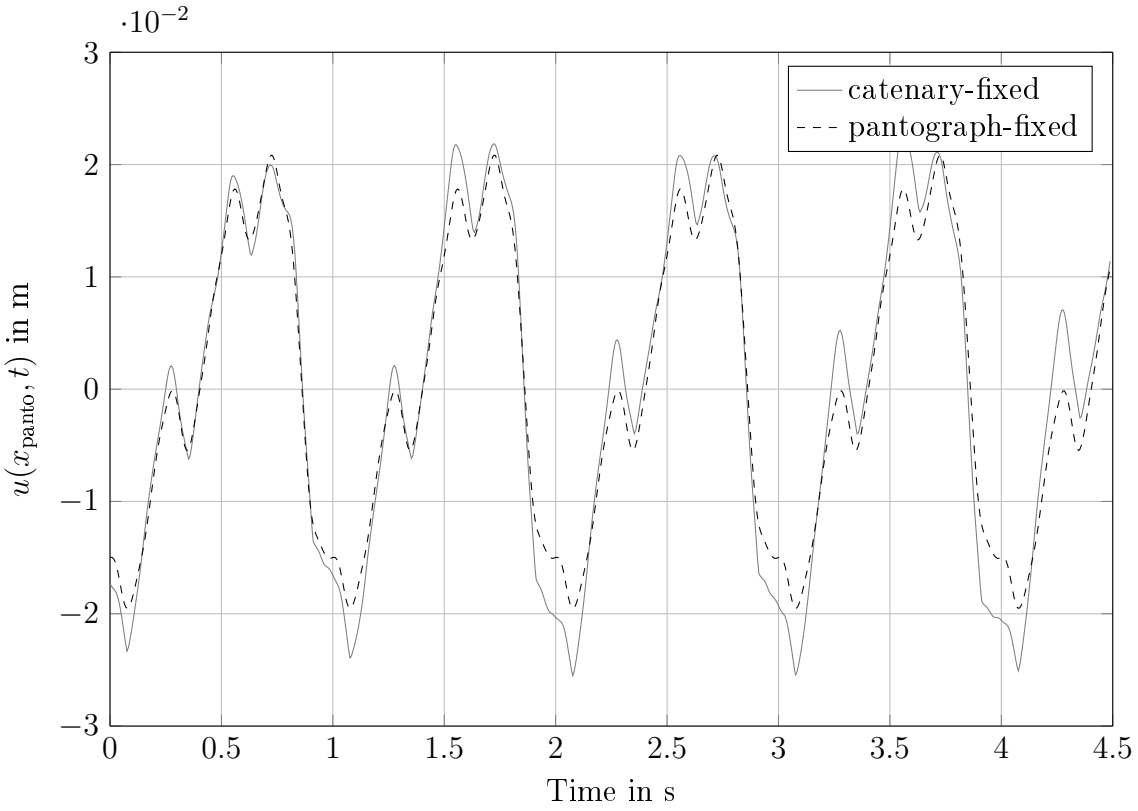

Figure 1.14: Comparison of the catenary-fixed and the pantograph-fixed model: Displacement $u(x, t)$ at the contact point $x = x_{\text{panto}}$.

ters are summarized in Table 1.1. This Figure shows that the pantograph-fixed model has an overall very good agreement with the catenary-fixed model. The observed deviation from the catenary-fixed formulation arises from a substantially coarser spatial discretization (see Table 1.1). The pantograph-fixed formulation shows the following advantages:

- 6.25 times less states per span for similar fidelity,
- smaller simulation domain: For this setup a 5 s-run of the catenary-fixed formulation requires a simulation area of 15 spans (900 m) to avoid reflections versus 1 span (60 m) of the pantograph-fixed formulation.
- a speed-up factor of > 5500: each second simulated of the pantograph-fixed formulation takes about ≈ 83 ms compared to 460 s of the catenary-fixed formulation[2].

Taking these facts into account, the proposed coordinate transform and the use of absorbing layers lead to a very good trade-off between computational effort and accuracy and is, therefore, well-suited for real-time applications.

wire	ρA kg/m	β kg/s/m	EI N m^2	T N
contact	1.35	0	150	20×10^3
carrier	1.35	0	0	20×10^3
j	1	2	3	4
j-th dropper position	5 m	21.67 m	38.33 m	55 m
j-th dropper stiffness	10 000 N/m	10 000 N/m	10 000 N/m	10 000 N/m
	F_{panto}	Δt	Δx	
pantograph-fixed	100 N	1/170 s	1.5 m	
catenary-fixed	100 N	1/68 000 s	0.24 m	

Table 1.1: Physical and simulation parameters of the proposed 60 m catenary span

[2] on a standard PC (Intel i7 3.2 GHz)

1.4 Summary of the Scientific approaches

In Publication A an MOO identification methodology is presented, which allows to identify the material parameters including damping of an EBB under axial load using single measurement and a known excitation signal. The MOO approach allows to trade conflictive objectives such as performance and stability which are specified and optimized simultaneously. Performance is rated by means of the output-error of an FD discretized EBB equation. Stability is quantified in terms of the solution's time growth factor. The optimization result is a Pareto front approximation where each solution represents a parameter set. To verify identifiability the regularity of the Fisher information matrix is checked. The methodology is validated on an actual laboratory test bed.

Publication B presents an optimization methodology for the determination of highly absorbing and stable ABCs. ABCs are used to obtain the unbounded domain solution of wave propagation problems described by linear PDEs. These PDEs are discretized by FDs. The ABCs are designed for the spatial and temporal discretized PDEs. The accuracy of the ABCs is quantified in an output-error-sense and by computing the reflection coefficient of the ABCs. Those measures are used as a performance objective in the optimization problem. Stability was explicitly considered as constraint. This constraint ensures that all eigenvalues of the fully discrete PDE with ABCs in place are inside the unit circle. The method's flexibility is shown for the EBB under axial load and for the two-dimensional wave equation.

In Publication C a real-time catenary model is presented, designed for pantograph HiL testing. This catenary model is obtained by physical modeling, which enables simple parametrization. A pantograph-fixed coordinate formulation is used. In this coordinate formulation the pantograph is fixed and interacts with a moving catenary. This reduces the numerical effort drastically because only a section fore and aft of the pantograph has to be considered. To avoid unrealistic reflections at the boundaries, absorbing layers are attached. The catenary model is implemented on a real-time target to emulate the catenary dynamics on a Hil test rig interacting with an actual pantograph.

1.5 Scientific Contributions of this Thesis

The scientific contributions of this work can be summarized as:

- Development of a flexible MOO based identification methodology which includes
  - Suitable performance and stabilizing cost functions and a stability criterion for the physical parameters
  - A necessary identifiability condition

  - Validation by means of simulation and measurement data

- A generic optimization approach for determination of ABCs
  - Two performance objectives combined with a stability objective allow the ABC optimization for a generic wave propagation problem
  - The method was validated on an EBB under axial load and on the two-dimensional wave equation

- A real-time catenary model for pantograph HiL testing
  - Is obtained by physical modeling and using pantograph-fixed coordinates
  - Allows simple parametrization
  - Spurious reflection are eliminated using absorbing layers
  - Yields good accuracy-efficiency-trade-off

Bibliography

[1] UIC. High speed. 2016. URL `http://www.uic.org/highspeed`.

[2] Aschauer Guilherme, Emir Talic, Alexander Schirrer, Martin Kozek, and Stefan Jakubek. A mimo-mpc based impedance control formulation of hardware-in-the-loop test rigs for high-speed pantographs. *xx*, xx(x):xx, xx.

[3] M Arnold and B Simeon. Pantograph and catenary dynamics: a benchmark problem and its numerical solution. *Applied Numerical Mathematics*, 34(4):345–362, 2000.

[4] Alexander Schirrer, Emir Talic, and Martin Kozek. A flexible matlab-based simulation framework for dynamic catenary-pantograph interaction and co-simulation. In *Modelling and Simulation (EUROSIM), 2013 8th EUROSIM Congress on*, pages 288–293. IEEE, 2013.

[5] European Committee for Electrotechnical Standardization. Railway applications – Current collection systems – Validation of simulation of the dynamic interaction between pantograph and overhead contact line, 2002.

[6] Emir Talic, Alexander Schirrer, Martin Kozek, and Stefan Jakubek. Multi-objective parameter identification of euler–bernoulli beams under axial load. *Journal of Sound and Vibration*, 341:86–99, 2015.

[7] A Schirrer, E Talic, G Aschauer, M Kozek, and S Jakubek. Optimization based determination of highly absorbing boundary conditions for linear finite difference schemes. *Journal of Sound and Vibration*, 365:45–69, 2016.

[8] A Facchinetti and S Bruni. Hardware-in-the-loop hybrid simulation of pantograph–catenary interaction. *Journal of Sound and Vibration*, 331(12):2783–2797, 2012.

[9] Lars Finner, Gero Poetsch, Bernhard Sarnes, and Michael Kolbe. Program for catenary–pantograph analysis, prosa statement of methods and validation according en 50318. *Vehicle System Dynamics*, 53(3):305–313, 2015.

[10] Angelines Alberto, Jesús Benet, Enrique Arias, David Cebrian, Tomás Rojo, and Fernando Cuartero. A high performance tool for the simulation of the dynamic pantograph–catenary interaction. *Mathematics and Computers in Simulation*, 79 (3):652 – 667, 2008.

[11] Daniel Ritzberger, Emir Talic, and Alexander Schirrer. Efficient simulation of railway pantograph/catenary interaction using pantograph-fixed coordinates. *IFAC-PapersOnLine*, 48(1):61–66, 2015. ISSN 2405-8963. 8th Vienna International Conference on Mathematical Modelling, MATHMOD 2015.

[12] R. LeVeque. *Finite Difference Methods for Ordinary and Partial Differential Equations: Steady-State and Time-Dependent Problems (Classics in Applied Mathematics Classics in Applied Mathemat)*. Society for Industrial and Applied Mathematics, Philadelphia, PA, USA, 2007. ISBN 0898716292, 9780898716290.

[13] K. Deb, A. Pratap, S. Agarwal, and T.A.M.T. Meyarivan. A fast and elitist multiobjective genetic algorithm: Nsga-ii. *Evolutionary Computation, IEEE Transactions on*, 6(2):182–197, 2002.

[14] R.T. Marler and J.S. Arora. Survey of multi-objective optimization methods for engineering. *Structural and Multidisciplinary Optimization*, 26(6):369–395, 2004.

[15] Robert Higdon. Numerical absorbing boundary conditions for the wave equation. *Mathematics of Computation*, 49(179):65–90, 1987.

[16] E. I. Jury. A simplified stability criterion for linear discrete systems. *Proceedings of the IRE*, 50(6):1493–1500, June 1962. ISSN 0096-8390. doi: 10.1109/JRPROC.1962.288193.

[17] Yuval Bistritz. A circular stability test for general polynomials. *Systems & control letters*, 7(2):89–97, 1986.

[18] Björn Engquist and Andrew Majda. Absorbing boundary conditions for numerical simulation of waves. *Proceedings of the National Academy of Sciences*, 74(5):1765–1766, 1977.

[19] Robert Higdon. Radiation boundary conditions for dispersive waves. *SIAM J. Numer. Anal.*, 31(1):64–100, February 1994. ISSN 0036-1429.

[20] Daniel Ritzberger, Alexander Schirrer, and Stefan Jakubek. Absorbing boundary layer control for axially moving materials. *Journal of Vibration and Control (under review)*, 2016.

[21] J. Crank and P. Nicolson. A practical method for numerical evaluation of solutions of partial differential equations of the heat-conduction type. *Mathematical Proceedings of the Cambridge Philosophical Society*, 43:50–67, 1 1947. ISSN 1469-8064.

Chapter 2

Publications

List of selected journal publications:

Publication A

Emir Talic, Alexander Schirrer, Martin Kozek, Stefan Jakubek
Multi-objective parameter identification of Euler-Bernoulli beams under axial load
Journal of Sound and Vibration, Volume 341, 2015, Pages 86-99, ISSN 0022-460X,
DOI: 10.1016/j.jsv.2014.12.012

Publication B

Alexander Schirrer, Emir Talic, Guilherme Aschauer, Martin Kozek, Stefan Jakubek,
Optimization based determination of highly absorbing boundary conditions for linear finite difference schemes
Journal of Sound and Vibration, Volume 365, 2016, Pages 45–69, ISSN 0022-460X
DOI: 10.1016/j.jsv.2015.12.006

Publication C

Guilherme Aschauer, Emir Talic, Alexander Schirrer, Martin Kozek and Stefan Jakubek.
Catenary Emulation for Hardware-in-the-Loop Pantograph Testing with a Model Predictive Energy-Conserving Control Algorithm
Mechatronics, accepted with minor revision

Publication A

Emir Talic, Alexander Schirrer, Martin Kozek, Stefan Jakubek
Multi-objective parameter identification of Euler-Bernoulli beams under axial load
Journal of Sound and Vibration, Volume 341, 2015, Pages 86-99, ISSN 0022-460X,
DOI: 10.1016/j.jsv.2014.12.012

Author's contribution

Problem analysis, selection of methods, execution of the solution, development and programming of algorithms, post-processing of measurement data, performing simulation studies, and structuring, writing and editing of the manuscript was done by the applicant.

Journal of Sound and Vibration 341 (2015) 86–99

Contents lists available at ScienceDirect

Journal of Sound and Vibration

journal homepage: www.elsevier.com/locate/jsvi

Multi-objective parameter identification of Euler–Bernoulli beams under axial load

Emir Talic*, Alexander Schirrer, Martin Kozek, Stefan Jakubek

Division of Control & Process Automation, Institute of Mechanics & Mechatronics, Vienna University of Technology, Getreidemarkt 9, 1060 Vienna, Austria

ARTICLE INFO

Article history:
Received 9 May 2014
Received in revised form
4 December 2014
Accepted 6 December 2014
Handling Editor: K. Shin
Available online 14 January 2015

ABSTRACT

Identification of physical parameters of the partial differential equation describing transverse vibrations of an axially loaded Euler–Bernoulli beam (EBB) is proposed via a multi-objective optimization formulation and solved by a genetic algorithm. Conflicting objectives such as performance and stability are specifically formulated and optimized simultaneously. Stability is quantified in terms of the solution's time growth factor. Physical parameter sets in the resulting Pareto front approximation represent best trade-offs with respect to the multiple objectives. To compute output error performance objectives, the EBB equation is discretized via finite differences in space and time and reformulated to a state space system. Identifiability is verified by checking regularity of the so-called Fisher information matrix. The identification methodology is capable of determining material parameters, including damping, as well as the axial load from few, spatially concentrated measurements. Its features are demonstrated and successfully validated on specific simulation data and measurement data obtained from a laboratory testbed.

1. Introduction

Many engineering disciplines rely on model-based strategies for system design, simulation, or control. Therefore, models of optimal quality need to be obtained with limited modeling effort. Generic conflicting objectives for the modeling process are high model quality for the system quantities in the relevant domain, consistency of properties such as system stability, low modeling effort, low model complexity, easy parametrization, parameter interpretability, and flexibility with respect to system parameter changes. The modeling process is particularly challenging for distributed-parameter systems, that is, systems whose dynamics are governed by partial differential equations (PDEs).

The main contributions of this paper are (i) the development of a multi-objective optimization methodology to identify physical parameters of an Euler–Bernoulli beam (EBB) model of transverse beam vibrations under constant (but unknown) axial load and known traversal excitation, (ii) the development of suitable performance and stabilizing cost functions including a stability criterion for the physical parameters, and (iii) the formulation of a necessary identifiability condition with respect to the performance objectives. To solve the multi-objective parameter optimization problem, a multi-objective

* Corresponding author.
E-mail addresses: emir.talic@tuwien.ac.at (E. Talic), alexander.schirrer@tuwien.ac.at (A. Schirrer), martin.kozek@tuwien.ac.at (M. Kozek), stefan.jakubek@tuwien.ac.at (S. Jakubek).

http://dx.doi.org/10.1016/j.jsv.2014.12.012
0022-460X/

genetic algorithm is employed. After the optimization the best possible trade-offs of the represent physical parameter sets are available. The approach aims to keep the necessary measurement effort as small as possible while obtaining high model quality. It is successfully validated at both specific simulation data and measurement data from a laboratory testbed.

Identification of parameters of beam equations has been investigated in various ways. Given the displacement field of a vibrating beam, the authors of Ref. [1] study the identification of the forcing location (forcing function) by the experimental, localized force analysis technique (FAT). Rigid-body parameters (mass, center-of-gravity, inertia tensor) of a softly suspended flexible structure have been identified based on measured vibration data by a modal analysis approach in Ref. [2]. Various techniques to identify viscous damping parameters in linear dynamic models and to assess these methods in an experimental setting in terms of frequency-domain and spatial fit are investigated in Ref. [3]. In Ref. [4], solutions for flexural vibrations in cylindrical rods, both for slender and thick geometries and also considering axial forces are given numerically and are verified by experiments. Refs. [5–7] propose identification approaches to determine the axial loads and boundary condition parameters of Euler–Bernoulli beams from sufficiently many vibration measurements. The required number of spatially distinct measurement positions depends on the number of unknowns in the boundary conditions. In Ref. [8] the authors identify the axial force and stiffness of an Euler–Bernoulli beam under compressive axial load from measured displacement data based on a modal decomposition via a regularized least-squares approach. In Ref. [9] the mechanical properties of a laminated beam are identified using a Ritz–Galerkin approach and the inverse problem is solved by a multi-start global search algorithm. In Ref. [10], a modal inverse method is proposed to identify material parameters of sandwich composite beams considered as Timoshenko beams. The work [11] surveys vibration-based damage identification methods which comprise a special case of the parameter identification problem in elastic structures. More recently, beam structure damage identification has been treated for example in Ref. [12] which focuses on the change of wave propagation properties when damage is present.

In the field of structural model identification and damage detection, multi-objective optimization formulations are used and solved by evolutionary algorithms like genetic algorithms [13–16]. All of these references use Finite Element models. In [13] a multi-objective framework is proposed to identify multiple modal properties (modal frequencies and shapes) simultaneously using the Strength Pareto Evolutionary Algorithm [17]. To quantify and localize the structural damage of beams, the authors of [14] use the modal flexibility [18] as first objective and the quotient between a mode shape change and a frequency change (which only depends on the location of the damage [19]) as a second objective, respectively. The resulting multi-objective optimization problem is solved by the Niched Pareto Genetic Algorithm [20]. A special parameter selection method based on the parameter sensitivity was introduced in [21] in addition to a Finite Element model updating both integrated in a multi-objective optimization framework.

In contrast to the aforementioned works, this contribution aims at obtaining all physical problem parameters (stiffness, damping, axial force, density) of an EBB simultaneously from one or more measurement signals plus the known excitation signal, the problem geometry, and the boundary conditions. Performance and stability of the resulting system discretization are explicitly considered in the multi-objective optimization problem formulation.

The multi-objective identification methodology in this paper is developed in Section 2. First, the EBB equation under axial load with initial and boundary conditions is defined. To perform the multi-objective optimization a simulation model of the EBB equation is needed. The simulation model should be flexible with respect to sensor and actor configurations and effective with respect to simple implementation and numerical accuracy in the context of noisy measurement data. An effective choice for the numerical approximation of the EBB equation is the finite difference (FD) method because its implementation is simple yet flexible, and the accuracy of the second-order approximations is sufficient when applying FD to approximate the temporal and spatial partial derivatives, a system of (implicit) algebraic equations is obtained. To increase flexibility with respect to variations of sensor and actor placement these equations are reformulated into a discrete state space representation.

High model quality can be obtained by minimizing the model output error (the difference between the time signal of the model output and the measured output) for an output error configuration. Identifiability of the parameters is verified by checking regularity of the so-called Fisher information matrix [22,23]. A necessary condition of identifiability is stated. In the next step, the multi-objective parameter identification problem is defined and performance objectives are formulated to minimize the model output error. If only performance objectives are utilized, the identified parameter set may lead to unstable system dynamics even if the model output error is low and the original process is stable. This justifies the formulation of a stabilizing objective (instead of a stability constraint), illustrating the trade-off between performance and stability margin. A stability criterion is defined by utilizing a discrete fundamental solution to the unbounded discretized PDE and by obtaining the so-called dispersion relation [24]. This dispersion relation is a complex polynomial in the temporal growth factor, and its coefficients are functions of the physical parameters. The roots of this polynomial all have to reside inside the unit circle to ensure stability. To formulate bounds for the physical parameters that ensure stability, the Bistritz criterion [25] is used. The stabilizing objective proposed in this paper ensures stability and is also a quantitative measure of stability of the identified parameter set. The multi-objective optimization problem is solved by means of a multi-objective genetic algorithm which produces an approximation of the Pareto front. This enables the engineer to select efficient physical parameter sets without re-optimization and eases understanding of the multi-objective problem.

In Section 3 the developed identification methodology is demonstrated by means of simulation data generated with an undamped beam model as well as actual measurement data from a laboratory testbed. The simulation data example demonstrates the pairing of a performance and a stability objective, whereas the measurement data test case considers two

different performance objectives. In both cases it is possible to fit all relevant physical parameters with one prescribed displacement or forcing input excitation and one displacement measurement to produce high model fit in validation. The paper closes with a conclusion in Section 4.

2. Methodology

In this section a methodology for parameter identification of an EBB model will be presented by means of multi-objective optimization.

First, assumptions for the validity of EBB theory are summarized and the EBB equation is displayed. The EBB equation is discretized by finite differences (FD) leading to a system of (generally implicit) difference equations. Here, FD are chosen to discretize EBB because their implementation is simple, flexible, and their accuracy is sufficient. To evaluate if the discretized system is identifiable with respect to physical parameters, the Fisher information matrix is formulated and checked for regularity.

Multi-objective optimization is then applied to ensure stability of the discretized system for the identified parameter set as well as to maximize model output fit.

2.1. The Euler–Bernoulli beam equation under axial load

The EBB equation describes transverse vibrations of beams under a distributed force load, which uses linear isotropic theory of elasticity and neglects the effects of rotary inertia and shear deformation [26,27]. EBB theory can be used if the following assumptions are satisfied [28]:

- the cross sections of a beam are rigid in their plane,
- they remain plane after deformation, and
- they remain perpendicular to the deformed axis.

A general form of the linear non-homogeneous Euler–Bernoulli beam equation under axial load with constant coefficients is given by

$$\rho A\frac{\partial^2 u}{\partial t^2}+d_v\frac{\partial u}{\partial t}+d_{\mathrm{mat}}\frac{\partial^5 u}{\partial x^4\partial t}=-EI\frac{\partial^4 u}{\partial x^4}+T\frac{\partial^2 u}{\partial x^2}+f(x,t) \tag{1}$$

with the spatial variable $x\in[0,L]$, where $L\in\mathbb{R}$, the time variable $t\in\mathbb{R}$ and the traversal displacement $u=u(x,t)$. The constant coefficients in Eq. (1) are the mass per length unit ρA, viscous damping coefficient d_v, material damping coefficient d_{mat}, bending stiffness EI, tensile force T and external traversal force density $f(x,t)$. Eq. (1) will be solved for the clamped–clamped testbed setup displayed in Fig. 1 which leads to the boundary conditions:

$$u(x,t)\big|_{x=0}=u(x,t)\big|_{x=L}=0 \tag{2}$$

$$\frac{\partial u}{\partial x}(x,t)\big|_{x=0}=\frac{\partial u}{\partial x}(x,t)\big|_{x=L}=0. \tag{3}$$

A numeric solution for EBB with suitable initial conditions $u(x,0)=u_0$ and $(\partial u/\partial t)(x,0)=v_0$ is required. This can be achieved in various ways. Here, a numeric approximation by the finite difference method is chosen to allow flexibility with respect to boundary conditions, system coupling and spatial parameter dependence. Note that other discretization methods (e.g. Finite Element and Finite Volume methods) can be directly used. The identification problem is structurally equivalent.

2.2. Approximation by finite differences

Finite differences are a simple and effective method to approximate (partial) derivatives. The FD approximations can be derived for any derivative and any error truncation order [29,30]. For real-world applications it is important to find

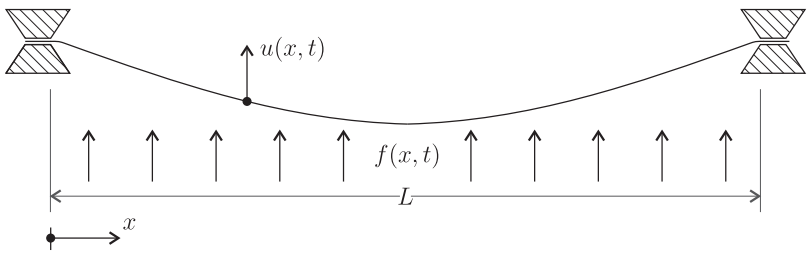

Fig. 1. Euler–Bernoulli beam with clamped–clamped boundary conditions.

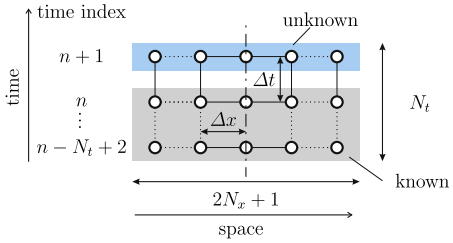

Fig. 2. Spatially symmetric stencil.

a trade-off between accuracy and insensitivity to numerical errors. Here, the FD approximation for all partial derivatives are chosen with a truncation error of order two.

A general stencil is displayed in Fig. 2 with the temporal extension N_t and the spatial extension $2N_x+1$. Denoting $u(x_k,t_n)=u_k^n$ and assuming an equidistant temporal and spatial grid with $t=[0,\Delta t,2\Delta t,\ldots,N_T\Delta t]$, $x=[0,\Delta x,2\Delta x,\ldots,N_L\Delta x=L]$ with fixed $\Delta t,\Delta x\in\mathbb{R}^+$ and $N_t,N_T,N_x,N_L\in\mathbb{N}$, the partial derivatives in Eq. (1) for the interior of the problem domain are efficiently approximated by standard central difference coefficients:

$$\frac{\partial^2 u}{\partial x^2}(x_k,t_n)\approx\frac{u_{k-1}^n-2u_k^n+u_{k+1}^n}{(\Delta x)^2},\quad \frac{\partial^2 u}{\partial t^2}(x_k,t_n)\approx\frac{u_k^{n-1}-2u_k^n+u_k^{n+1}}{(\Delta t)^2},$$

$$\frac{\partial^4 u}{\partial x^4}(x_k,t_n)\approx\frac{u_{k-2}^n+4u_{k-1}^n+6u_k^n-4u_{k+1}^n+u_{k+2}^n}{(\Delta x)^4},$$

$$\frac{\partial^5 u}{\partial x^4\partial t}(x_k,t_n)\approx\frac{\frac{\partial^4 u}{\partial x^4}(x_k,t_{n+1})-\frac{\partial^4 u}{\partial x^4}(x_k,t_{n-1})}{2\Delta t}. \tag{4}$$

Inserting these approximations from Eq. (4) into Eq. (1), a system of difference equations is obtained for the interior of the problem domain ($k=N_x,\ldots,(N_L-N_x)$):

$$\boldsymbol{\mu}_1^{\mathrm{T}}\mathbf{u}_k^{n+1}=\boldsymbol{\mu}_0^{\mathrm{T}}\mathbf{u}_k^n+\boldsymbol{\mu}_{-1}^{\mathrm{T}}\mathbf{u}_k^{n-1}+\eta f_k^n. \tag{5}$$

Thereby the force density is denoted by $f_k^n=f(x_k,t_n)$ and the coefficients $\boldsymbol{\mu}_j=\boldsymbol{\mu}_j(\mathbf{p},\Delta x,\Delta t)$, $\eta=\eta(\mathbf{p},\Delta x,\Delta t)$ for the relative time level j depend on the parameters $\mathbf{p}$. Note that here Δx, Δt are chosen a priori so that a stable scheme is obtained for the expected and initial physical parameter values. Instead, they could also be considered as free decision variables, increasing the number of identification parameters. The coefficients $\boldsymbol{\mu}_j$ are defined for $j=-1,0,1$ as

$$\boldsymbol{\mu}_1=\begin{bmatrix}\mu_{1,N_x}\\ \vdots\\ \mu_{1,N_x}\end{bmatrix},\quad \boldsymbol{\mu}_0=\begin{bmatrix}\mu_{0,N_x}\\ \vdots\\ \mu_{0,N_x}\end{bmatrix},\quad \boldsymbol{\mu}_{-1}=\begin{bmatrix}\mu_{-1,N_x}\\ \vdots\\ \mu_{-1,N_x}\end{bmatrix}. \tag{6}$$

Finally, the vectors of the approximated solution values are

$$\mathbf{u}_k^{n+1}=\begin{bmatrix}u_{k-N_x}^{n+1}\\ \vdots\\ u_{k+N_x}^{n+1}\end{bmatrix},\quad \mathbf{u}_k^{n}=\begin{bmatrix}u_{k-N_x}^{n}\\ \vdots\\ u_{k+N_x}^{n}\end{bmatrix},\quad \mathbf{u}_k^{n-1}=\begin{bmatrix}u_{k-N_x}^{n-1}\\ \vdots\\ u_{k+N_x}^{n-1}\end{bmatrix}, \tag{7}$$

and the vector of physical parameters is given by

$$\mathbf{p}=[\rho A,d_v,d_{\mathrm{mat}},EI,T]. \tag{8}$$

The values at the remaining grid points $k=0,\ldots,N_x-1,N_L-N_x+1,\ldots,N_L$ are determined using the boundary conditions. Here, the boundary conditions given in Eqs. (2) and (3) are approximated by FD with a truncation error of order one

$$u(x,t)\big|_{x=0}=u(x,t)\big|_{x=L}=u_0^n=u_{N_L}^n=0 \tag{9}$$

$$0=\frac{\partial u}{\partial x}(x,t)\big|_{x=0}\approx\frac{-u_0^n+u_1^n}{\Delta x}\rightarrow u_1^n=0 \tag{10}$$

$$0=\frac{\partial u}{\partial x}(x,t)\big|_{x=L}\approx\frac{u_{N_L}^n-u_{N_L-1}^n}{\Delta x}\rightarrow u_{N_L-1}^n=0. \tag{11}$$

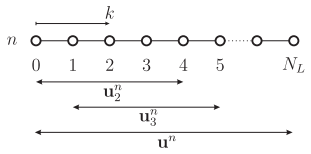

Fig. 3. Vector notation for $N_x=2$.

Summarizing Eqs. (5) and (9)–(11) and denoting $\mathbf{u}^n$ as in Fig. 3 an implicit system of difference equations in state space is obtained as

$$\underbrace{\begin{bmatrix}\mathbf{I} & \mathbf{0}\\ \mathbf{0} & \tilde{\mathbf{M}}_1\end{bmatrix}}_{\mathbf{M}(\mathbf{p})}\underbrace{\begin{bmatrix}\mathbf{u}^n\\ \mathbf{u}^{n+1}\end{bmatrix}}_{\mathbf{x}^{n+1}}=\underbrace{\begin{bmatrix}\mathbf{0} & \mathbf{I}\\ \tilde{\mathbf{M}}_{-1} & \tilde{\mathbf{M}}_0\end{bmatrix}}_{\mathbf{A}(\mathbf{p})}\underbrace{\begin{bmatrix}\mathbf{u}^{n-1}\\ \mathbf{u}^n\end{bmatrix}}_{\mathbf{x}^n}+\mathbf{B}(\mathbf{p})\mathbf{f}^n, \tag{12}$$

$$\hat{\mathbf{y}}^n=\mathbf{C}\mathbf{x}^n \tag{13}$$

with the state vector $\mathbf{x}^n$, the input (force) vector $\mathbf{f}^n=[f_0^n,f_0^n,\ldots,f_{N_L}^n]^{\mathrm{T}}$, the system matrix $\mathbf{A}(\mathbf{p})$, the input matrix $\mathbf{B}(\mathbf{p})$, the output matrix $\mathbf{C}$ and the model output vector $\hat{\mathbf{y}}^n$. The model output vector $\hat{\mathbf{y}}^n=[\hat{y}_0^n,\hat{y}_1^n,\ldots,\hat{y}_{N_y}^n]^{\mathrm{T}}$ defines all measurable values as linear combinations of the state vector $\mathbf{x}^n$, where N_y denotes the number of outputs. Eq. (12) includes the implicit FD case with coefficients of the form

$$\tilde{\mathbf{M}}_q=\begin{bmatrix}\mathcal{B}_q^l\\ \mathcal{M}_q\\ \mathcal{B}_q^r\end{bmatrix}, \tag{14}$$

$$\mathcal{M}_q(\mathbf{p})=\begin{bmatrix}\ddots & \ddots & \ddots & & & & & & & \\ 0 & \cdots & 0 & \mu_{q,N_x} & \cdots & \mu_{q,N_x} & 0 & \cdots & \cdots & 0\\ 0 & \cdots & \cdots & 0 & \mu_{q,N_x} & \cdots & \mu_{q,N_x} & 0 & \cdots & 0\\ & & & & & & & \ddots & \ddots & \ddots\end{bmatrix}, \tag{15}$$

with $q=\{1,0,-1\}$ as well as the explicit FD-case for $\mathcal{M}_1=\mathbf{I}$, where $\mathbf{I}$ is the identity matrix. The matrices $\mathcal{B}_q^r$ and $\mathcal{B}_q^l$ summarize those rows of $\tilde{\mathbf{M}}_q$ which result from the left and right boundary conditions, respectively.

Remark 1. For clarity of exposition Eqs. (12)–(15) are displayed for time-invariant parameters. In a time-varying setting, the parameter dependence on absolute time needs to be considered by formulating Eq. (5) separately for each absolute time index n with absolute-time-dependent coefficients $\boldsymbol{\mu}_q^n$. Analogously, smoothly spatially varying parameters can be considered by FD.

Remark 2. The proposed methodology directly supports other discretization methods like Finite Element or Finite Volume methods. By substituting $\boldsymbol{\mu}_1^{\mathrm{T}}$, $\boldsymbol{\mu}_0^{\mathrm{T}}$, $\boldsymbol{\mu}_{-1}^{\mathrm{T}}$ and η in Eq. (5) with the corresponding Finite Element and Finite Volume stencil coefficients, the developments in the following sections can be applied directly.

2.3. Identifiability

A necessary condition for the unique identifiability of parameters of partial differential equations (PDEs) from measured output signals is that the considered (measured) model outputs are in fact affected by the parameters to be identified. This is formalized by the Fisher information matrix [31,22]. For the output error configuration [32], consider the following linear time-invariant parameter-dependent model (corresponding in its form to the explicit FD scheme of the EBB)

$$\mathbf{x}^{n+1}=\mathbf{A}(\mathbf{p})\mathbf{x}^n+\mathbf{B}(\mathbf{p})\mathbf{f}^n$$

$$\hat{\mathbf{y}}^n=\mathbf{C}\mathbf{x}^n. \tag{16}$$

The output error signal is defined as the deviation of the model output signal $\hat{\mathbf{y}}^n(\mathbf{p})$ from a measured output signal $\mathbf{y}^n$,

$$\mathbf{e}^n=\hat{\mathbf{y}}^n(\mathbf{p})-\mathbf{y}^n, \tag{17}$$

where the model output sequence is generated by a known input signal $\mathbf{f}^n$ for time indices $n=0,\ldots,N_T$.

Definition 1. A necessary condition for a unique solution of the parameter identification problem based on the output error equation (17) is that the Fisher information matrix of the output error [23],

$$\mathcal{I} = \frac{1}{\sigma^2}\sum_{n=0}^{N_T} \frac{\mathrm{d}\hat{\mathbf{e}}^n(\mathbf{p})}{\mathrm{d}\mathbf{p}} \left(\frac{\mathrm{d}\hat{\mathbf{e}}^n(\mathbf{p})}{\mathrm{d}\mathbf{p}}\right)^{\mathrm{T}} = \frac{1}{\sigma^2}\sum_{n=0}^{N_T} \frac{\mathrm{d}\hat{\mathbf{y}}^n(\mathbf{p})}{\mathrm{d}\mathbf{p}} \left(\frac{\mathrm{d}\hat{\mathbf{y}}^n(\mathbf{p})}{\mathrm{d}\mathbf{p}}\right)^{\mathrm{T}}, \tag{18}$$

is non-singular [22]. Note that the total differential requires a recursive computation which can be realized in a time-marching manner similar to the actual solution of the state-space system equation (16).

The eigenvalues of $\mathcal{I} = \mathcal{I}(\mathbf{p})$ are affected especially by (i) the selection and placement of the sensors and actuators, (ii) the initial data and input sequence, and (iii) the parameter values $\mathbf{p}$. Quantitative measures of identifiability have been established in the field of the optimal design of experiments. They are scalar functions of $\mathcal{I}$, notably

- the trace of the inverse of $\mathcal{I}$ (minimization objective for A-optimality),
- the determinant of $\mathcal{I}$ (maximization objective for D-optimality), and
- the smallest eigenvalue of $\mathcal{I}$ (maximization objective for E-optimality).

Optimal design-of-experiment methodologies address the optimal placement of sensors and actors and the optimal shaping of input/excitation sequences to maximize identifiability. They are not detailed in this work; instead, the interested reader is referred to [22,31–33].

For a scalar time signal f^n, the Fisher information matrix in Eq. (18) can be written as $\mathcal{I} = (1/\sigma^2)\boldsymbol{\Psi}^{\mathrm{T}}\boldsymbol{\Psi}$ with

$$\boldsymbol{\Psi} = \left[\frac{\mathrm{d}\hat{\mathbf{y}}^0(\mathbf{p})}{\mathrm{d}\mathbf{p}}, \frac{\mathrm{d}\hat{\mathbf{y}}^1(\mathbf{p})}{\mathrm{d}\mathbf{p}}, \ldots, \frac{\mathrm{d}\hat{\mathbf{y}}^{N_T}(\mathbf{p})}{\mathrm{d}\mathbf{p}}\right] = \mathbf{USV}^*. \tag{19}$$

Thereby, the non-negative diagonal matrix $\mathbf{S}$ contains the singular values σ_i $(i = 1, \ldots, N_{\mathrm{param}})$ of $\boldsymbol{\Psi}$ and $\mathbf{V}^*$ is the conjugate transpose of $\mathbf{V}$. The left and right singular vectors are the columns of $\mathbf{U}$ and $\mathbf{V}$ associated to the corresponding singular value, respectively. The singular values of $\boldsymbol{\Psi}$ are closely related to the eigenvalues of $\mathcal{I}$ and therefore are directly interpretable as a quantitative measure for identifiability of the corresponding parameter. The right singular vectors connect the parameters of $\mathbf{p}$ to the measure of σ_i. A singular value $\sigma_i = 0$ indicates a non-influential right-singular vector, which in turn corresponds to non-identifiable parameter(s) of $\mathbf{p}$.

2.4. Multi-objective data-based parameter identification

Multi-objective optimization (MOO) is used to optimize a problem with conflicting objectives such as performance and stability. In this chapter a performance objective in terms of an *output error minimization objective* and a stabilizing objective in terms of quantifying the *exponential decay rate* are defined. Then these types of objectives are combined to form a multi-objective data-based parameter identification problem.

2.4.1. Performance objectives

Output error performance objective functions are defined in the following for a single-input–single-output system configuration which covers the practically important case of one (known) excitation point force and one displacement measurement signal. Curly symbols denote spatially concentrated signals in time (forcing input, model outputs and measurement output signals).

Definition 2. The i-th *performance objective* $J_{\mathrm{perf},i}$ is the output error minimization objective

$$J_{\mathrm{perf},i} = \frac{\|\mathcal{Y}_i - \hat{\mathcal{Y}}_i(\mathbf{p})\|_2^2}{\|\mathcal{Y}_i\|_2^2}, \tag{20}$$

where the considered measurement sequence of the spatially concentrated signal is denoted $\mathcal{Y}_i$ and the model output sequence is denoted $\hat{\mathcal{Y}}_i$,

$$\mathcal{Y}_i = \left[y_k^0, y_k^1, \ldots, y_k^{N_{T,i}}\right]\Big|_{x_k = x_y} \tag{21}$$

$$\hat{\mathcal{Y}}_i = \left[\hat{y}_k^0(\mathbf{p}), \hat{y}_k^1(\mathbf{p}), \ldots, \hat{y}_k^{N_{T,i}}(\mathbf{p})\right]\Big|_{x_k = x_y}. \tag{22}$$

The system excitation is considered as

$$\mathcal{F}_i = \left[f_k^0, f_k^1, \ldots, f_k^{N_{T,i}}\right]\Big|_{x_k = x_u} \tag{23}$$

at spatial position x_u. Both $\mathcal{Y}_i$ and $\hat{\mathcal{Y}}_i$ are measured/modeled at x_k=x_y and a simple, spatially concentrated time-varying input signal acting at $x = x_u$ is considered. The number of time steps of the i-th sequence is denoted by $N_{T,i}$.

Note that the calculation of Eq. (20) requires the solution of Eq. (12) to obtain the model outputs equation (13). A sufficient condition for the existence of such solution is that **M** in Eq. (12) be non-singular. Furthermore, the measurement and input positions x_y and x_u in Definition 2 have to be interpolated adequately and with sufficient accuracy if they are not part of the spatial grid.

2.4.2. Stabilizing objective

In discretized PDEs instability can arise either because of inherent instability of the original PDE, or, if the PDE is stable per se as in the considered case, instability can appear through discretization. Furthermore, the parameter identification with short and noisy measurement sequences as well as for low-damped systems may lead to parameters which cause instability. In these cases a stable parameter set can be enforced by adding a stabilizing objective or a stabilizing constraint. On the one side using a stabilizing constraint a single objective optimization problem occurs and its solution is a stable candidate (parameter set). Depending on the single-objective optimization method and the starting point of the optimization a global minimum of the performance objective can be obtained. On the other side choosing a stabilizing objective results in a multi-objective optimization problem. Its solution is a set of candidates, where performance and stability can be traded against each other. Furthermore, the stability objective proposed here allows one to interpret the value of the stability objective as the reciprocal of the stability margin. The stabilizing objective allows one to decide if an identified parameter set is stable or not, which is of high value in practice. A necessary stability condition is summarized in the next theorem.

Theorem 1. *Let the discrete fundamental solution*

$$u_k^n = \left(\mathrm{e}^{\mathrm{i}\omega_x \Delta x}\right)^k \tau^n \tag{24}$$

be a solution of an unbounded discretized PDE with constant coefficients, with exponential decay rate $\tau \in \mathbb{C}$*, the spatial frequency* $\omega_x \in \mathbb{R}_0^+$ *and the imaginary unit* i*. This discretization is stable if the corresponding dispersion relation*

$$\tau^{N_t-1} - \sum_{i=0}^{N_t-2} b_i(\omega_x \Delta x)\tau^{-i} = 0 \tag{25}$$

with coefficients $b_i \in \mathbb{C}$ *satisfies*

$$\forall \omega_x \Delta x \in [0, \pi]\colon |\tau(\omega_x \Delta x)| < 1. \tag{26}$$

Proof. The dispersion relation [24] is a polynomial of order $N_t - 1$ with complex coefficients. It is derived by extending Eq. (5) for a general temporal extension N_t (see Fig. 2)

$$\underbrace{\boldsymbol{\mu}_1^{\mathrm{T}}\mathbf{u}^{n+1}}_{u_k^{n+1}} = \sum_{i=0}^{N_t-2} \boldsymbol{\mu}_{-i}^{\mathrm{T}}\mathbf{u}^{n-i} \tag{27}$$

and inserting Eq. (24) into Eq. (27). This yields

$$\left(\boldsymbol{\mu}_1^{\mathrm{T}}\boldsymbol{\kappa}\tau^1 - \sum_{i=0}^{N_t-2} \boldsymbol{\mu}_{-i}^{\mathrm{T}}\boldsymbol{\kappa}\tau^{-i}\right) u_k^n = 0 \tag{28}$$

with

$$\boldsymbol{\kappa}^{\mathrm{T}} = \left[\kappa^{-N_x}, \kappa^{-N_x+1}, \ldots, \kappa^{N_x-1}, \kappa^{N_x}\right] \tag{29}$$

and

$$\kappa = \mathrm{e}^{\mathrm{i}\omega_x \Delta x}. \tag{30}$$

Eq. (28) holds for non-trivial u_k^n only if the discrete dispersion relation

$$\underbrace{\boldsymbol{\mu}_1^{\mathrm{T}}\boldsymbol{\kappa}}_{a_1(\omega_x \Delta x)}\tau^1 - \sum_{i=0}^{N_t-2} \underbrace{\boldsymbol{\mu}_{-i}^{\mathrm{T}}\boldsymbol{\kappa}}_{a_{-i}(\omega_x \Delta x)}\tau^{-i} = 0 \tag{31}$$

is fulfilled. By multiplying Eq. (31) by τ^{N_t-2} and dividing it by a_{n+1} one can obtain a characteristic equation for τ, parametrized in $\omega_x \Delta x$:

$$\tau^{N_t-1} - \sum_{i=0}^{N_t-2} \underbrace{\frac{a_{-i}}{a_1}}_{b_i(\omega_x \Delta x)}\tau^{-i} = 0. \tag{32}$$

It is clear that for stability the solutions τ of Eq. (32) must satisfy $|\tau| < 1$, otherwise exponential growth of the solution in Eq. (24) in time would occur. □

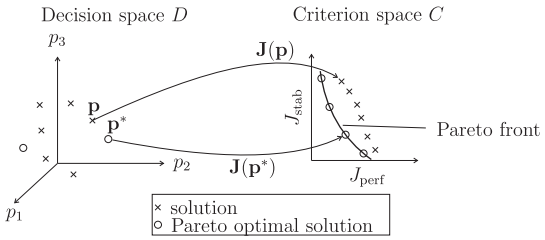

Fig. 4. Approximation of a Pareto front for $N_{\text{perf}} = 1$.

The coefficients b_i of Eqs. (25) and (32) are complex-valued for asymmetric stencils and real-valued for symmetric stencils. Conditions for b_i to satisfy Eq. (26) can be obtained by applying the Bistritz criterion. This criterion indicates that if the zeros of a complex polynomial with complex coefficients are inside or outside the unit circle [25].

Theorem 2 (*Bistritz [25] criterion*). *Given a polynomial with complex coefficients of order n*

$$B_n(z) = b_0 + b_1 z + \cdots + b_n z^n, \quad B_n(1) \in \mathbb{R}\backslash\{0\} \tag{33}$$

and the polynomials

$$T_n(z) = B_n(z) + \overline{B}_n(z) \tag{34}$$

$$T_{n-1}(z) = \frac{B_n(z) - \overline{B}_n(z)}{z-1} \tag{35}$$

$$T_{j-2}(z) = \frac{1}{z}\left[\left(\delta_j + \overline{\delta}_j\right) T_{j-1}(z) - T_j(z)\right], \quad j = n, \ldots, 2 \tag{36}$$

with

$$\delta_j = \frac{T_j(0)}{T_{j-1}(0)}, \quad j = n, \ldots, 2 \tag{37}$$

where $\overline{(\cdot)}$ *denotes complex conjugation. The number of zeros inside and outside the unit circle of* $B_n(z)$ *is* $n - v$ *and* v*, respectively with*

$$v = \text{Var}\{T_n(0), T_{n-1}(0), \ldots, T_0(0)\}. \tag{38}$$

Var *denotes the number of sign changes in the displayed sequence of real numbers in Eq. (38). A proof is omitted here but given in* [25].

Theorem 2 is feasible if $B_n(1) \in \mathbb{R}\backslash\{0\}$ and $T_{j-1}(0) \neq 0$ are fulfilled. $B_n(1) = 0$ implies that the polynomial has a zero on the unit circle and because of this violates the stability condition equation (26). $B_n(1) \in \mathbb{R}$ may be obtained by rescaling of $B_n(z)$ e. g. its multiplication by $\overline{B}_n(1)$. The second condition $T_{j-1}(0) \neq 0$ is necessary to perform the division in Eq. (37) and excludes singular cases. There are two types of singularities: the first type of singular cases leads either to roots on the unit circle or to reciprocal pair zeros and the second type implies zeros outside the unit circle. However, both singular cases violate Eq. (26) and will not be investigated further. The interested reader is referred to [25].

In the scope of this work the roots are computed for a finite number of $\omega_x \Delta x \in [\omega_{x,\min}, \pi]$, $\omega_{x,\min} > 0$, for the system equation (13) with $N_t = 1$, and symmetric stencils. It can be solved directly and the stability target is fulfilled if $\tau_{\max} = \max(|\tau_j|) < 1$ with $j = 1, 2$ and leads to the stability objective

$$J_{\text{stab}} = \tau_{\max}. \tag{39}$$

Remark 3. The stability criterion presented in this section only provides information on absolute stability. It is possible to implement relative stability criteria which effectively shape a desired frequency response, however, this approach adds artificial damping to the system dynamics.

Remark 4. The roots were computed at spatial frequencies $\omega_x \geq \omega_{x,\min} > 0$ to avoid the rigid body mode (integrator with $\tau_{\max}(\omega_x = 0) = 1$).

2.4.3. Multi-objective optimization problem

Using the performance and stability objectives defined by Eqs. (20) and (39), respectively, the multi-objective optimization problem

$$\min_{\mathbf{p}} \mathbf{J}(\mathbf{p}), \quad \mathbf{p} \in D, \ \mathbf{J} \in C \tag{40}$$

with

$$\mathbf{J} = \left[J_1(\mathbf{p}), \ldots, J_{N_{\text{perf}}+1}(\mathbf{p})\right] = \left[J_{\text{perf},1}(\mathbf{p}), \ldots, J_{\text{perf},N_{\text{perf}}}(\mathbf{p}), J_{\text{stab}}(\mathbf{p})\right] \tag{41}$$

is obtained, where N_{perf} represents the number of performance objectives, D is the *decision space*, C is the $N_{\text{perf}}+1-$dimensional *criterion space* and the objective function value vector $\mathbf{J}: D \rightarrow C$. A solution $\mathbf{p}$ of the MOO problem equation (40) generally cannot minimize all objective functions simultaneously if the objective functions are conflicting [34]. Interpreting the objective function value vector $\mathbf{J}(\mathbf{p})$ of any solution $\mathbf{p}$ in the criterion space, relative solution quality can be discriminated (see Fig. 4). Those solutions which cannot be improved in any objective without degrading at least one of the other objectives are called *Pareto optimal solutions* (see Definition 3).

Definition 3 (*Pareto optimal solution, Marler and Arora [35]*). A solution $\mathbf{p}^* \in D$ is Pareto optimal iff there does not exist another point $\mathbf{p} \neq \mathbf{p}^* \in D$ such that $\mathbf{J}(\mathbf{p}) \leq \mathbf{J}(\mathbf{p}^*)$, and $J_i(\mathbf{p}) < J_i(\mathbf{p}^*)$ for at least one objective function.

The set of all Pareto optimal solutions is called the Pareto front which describes the best possible, *efficient* trade-offs in the MOO problem. Pareto optimality is understood in a global sense, however, local notions of Pareto optimality can arise if the MOO problem is constrained [35]. Additionally, depending on the chosen MOO solution method, convergence to local optima may be an issue.

The existing MOO solution methods can mainly be categorized into methods of a priori and/or a posteriori articulation of preferences [35]. With a priori articulation, the relative weights (importance) of the objective functions is defined before running the optimization and the MOO problem is transformed into a single-objective optimization problem. Each iteration aims to improve the solution such that the weighted, scalar objective value is minimized. By varying the weights, different Pareto optimal solutions can be obtained. However, the main disadvantages of a priori articulation of preferences is that each new weighting requires re-optimization, one has to specify the weightings in advance without knowing the implied objective trade-off, and local convergence could prevent the algorithm from obtaining a Pareto optimal solution [35]. On the other hand, a posteriori articulation of preferences aims to produce a representation of the Pareto front itself, so that the final choice of a solution can be made when the efficient tradeoff topology is known. One of the a posteriori methods is the so-called multi-objective genetic algorithm [36]. The genetic algorithm is an evolutionary algorithm that mimics nature's evolutionary principles and uses a population of many solutions. These are improved over the iterations (generations).

In this paper the state-of-the-art multi-objective genetic algorithm “NSGA-II” [37] is chosen to solve the MOO problem equation (40) because it is capable of handling non-smooth objectives and constraints, and it is able to obtain an evenly spread, sampled approximation of the Pareto front. Furthermore it allows a posteriori articulation of preferences thus showing the objective trade-offs, and it is (or, can be tuned to be) insensitive to converging to local optima too quickly.

3. Validation

The identification methodology proposed in this paper is validated by an example based on simulation data and an example based on real-world measurement data. For both validation examples identifiability is fulfilled. This is verified by formulating the Fisher information matrix equation (18); their eigenvalues are strictly positive.

First the EBB parameter identification from simulated, noisy data of an undamped EBB equation is explained. This example will show a typical optimization run for railway contact wire parameters. The stability in terms of decay rate and performance in terms of model output fit will be traded against each other. The result is a evenly spread Pareto front, where each candidate represents a stable solution.

The second example is parameter identification based on measurement data. An actual, heavy beam is clamped under pretension. It is dynamically excited and displacement is measured. In consequence of the large damping of the tested beam, stability of the identification results is not an issue. Instead, two performance objectives are optimized simultaneously.

In both examples the parameter sensitivity will be analyzed.

3.1. Undamped beam

3.1.1. Problem setup

In this validation example, simulation results of an undamped beam model (1) with $d_v = d_{\text{mat}} = 0$) will be fed into the proposed multi-objective methodology to obtain a well-fitting, stable model. The boundary conditions of the initial simulation are

$$u(x,t)\big|_{x=0} = u(x,t)\big|_{x=L} = 0 \tag{42}$$

$$\frac{\partial u}{\partial x}(x,t)\big|_{x=0} = \frac{\partial u}{\partial x}(x,t)\big|_{x=L} = 0 \tag{43}$$

with $L = 7.5$ m as the beam length and the initial conditions are chosen as

$$u(x,t)\big|_{t=0} = 0, \quad \frac{\partial u}{\partial t}(x,t)\big|_{t=0} = 0. \tag{44}$$

The chosen initial parameter values $\mathbf{p}_{\text{init}} = [EI, T, \rho A, d_{\text{mat}}] = [150, 15\,000, 1, 0]$ are typical railway contact wire parameters. As input and output indices $\text{idx}_{\text{in}} = 18$ and $\text{idx}_{\text{out}} = 10$ were defined, where the number of grid points is $N_L = 23$ and temporal step size is $\Delta t = 8 \times 10^{-6}$ s. Using a band-limited white noise signal (std. deviation $\sigma \approx 460$ N) force input signal f, a noise-less displacement output signal y_{nl} was generated. To obtain a more realistic output sequence y, a band-limited white noise signal (std. deviation $\sigma \approx 0.01$ m) was added to y_{nl}.

3.1.2. Identifiability and parameter sensitivity

The identifiability of this example has been tested by means of regularity of the Fisher information matrix. This condition is fulfilled. Additionally one can obtain the parameter sensitivity by analyzing the singular values and right singular vectors (see Eq. (19)) for the parameter vector $\mathbf{p} = [EI, T, \rho A, d_{\text{mat}}]$ using the parameter values $\mathbf{p}_{\text{init}}$:

$$\mathbf{S} = \begin{bmatrix} 4.164 \times 10^{2} & 0 & 0 & 0 \\ 0 & 4.167 \times 10^{1} & 0 & 0 \\ 0 & 0 & 6.254 \times 10^{-2} & 0 \\ 0 & 0 & 0 & 9.196 \times 10^{-3} \end{bmatrix}, \tag{45}$$

$$\mathbf{V} = \begin{bmatrix} -1.000 & -2.164 \times 10^{-3} & \approx 0 & \approx 0 \\ \approx 0 & \approx 0 & 9.949 \times 10^{-1} & -1.011 \times 10^{-1} \\ \approx 0 & \approx 0 & 1.011 \times 10^{-1} & 9.949 \times 10^{-1} \\ -2.164 \times 10^{-3} & 1.000 & \approx 0 & \approx 0 \end{bmatrix}. \tag{46}$$

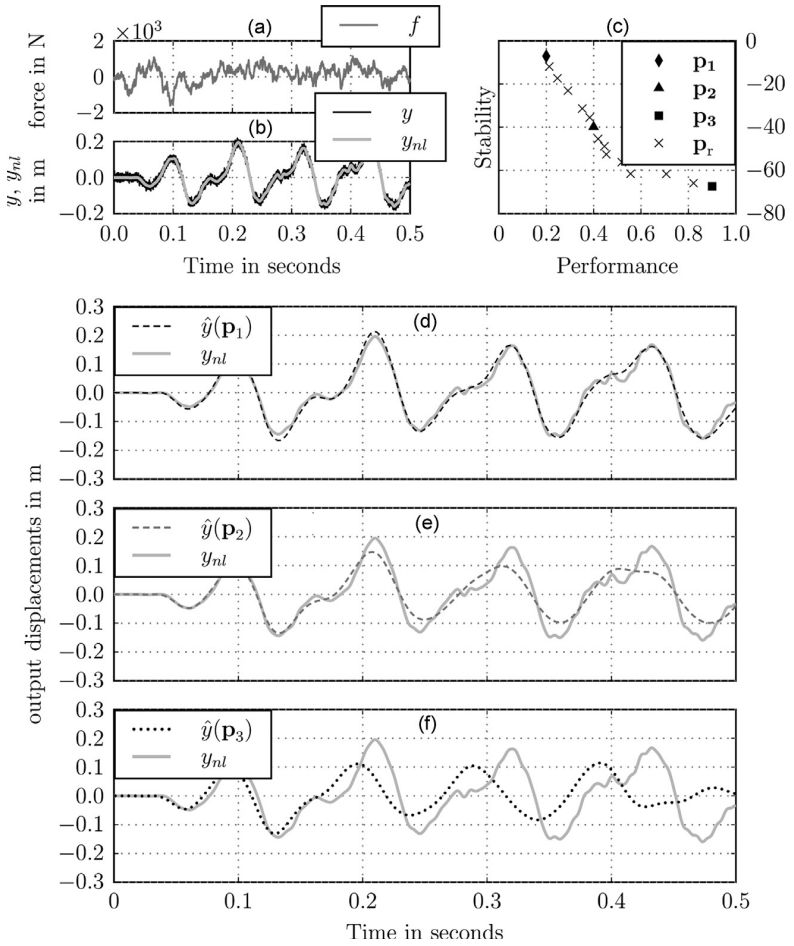

Fig. 5. Identification results with noisy model output data for an undamped pretensioned Euler–Bernoulli beam.

As one can see all parameters can be identified (singular values $\sigma_i > 0$ for $i = 1, \ldots, 4$) for this sensor and actuator placement and the chosen input sequence. The parameter ρA has the largest singular value, thus it is the most sensitive parameter and is coupled with the material damping d_{mat} (the second most sensitive parameter). The third and fourth columns of $\mathbf{V}$ indicate that the parameters bending stiffness EI and tensile force density T are coupled, whereby EI is more sensitive than T.

3.1.3. Identification results and optimization setup

The identification results are displayed in Fig. 5. The input signal f and the output signals y and y_{nl} are displayed in Fig. 5 (a) and (b). Fig. 5c displays the approximated Pareto front with the modified stability objective

$$\mathbf{J}_{\text{stab}} = \lambda = \ln(\tau_{\max})/(\Delta t) \tag{47}$$

on the ordinate, where the continuous-time decay rate λ is obtained from the relation

$$\tau_{\max} = \mathrm{e}^{\lambda \Delta t}. \tag{48}$$

The objective value λ can be directly interpreted as decay rate or eigenvalue of the corresponding continuous time model and $\lambda < 0$ denotes a stable system. On the abscissa of Fig. 5c one can see the performance objective values. The remaining parameter sets in Fig. 5c are denoted by $\mathbf{p}_r$. Additionally, the model output $\hat{y}$ for three different parameter sets $\mathbf{p}_1$, $\mathbf{p}_2$ and $\mathbf{p}_3$ is compared with y_{nl} in Fig. 5d-f, respectively.

Fig. 5d shows the model with the best fit. The model output $\hat{y}$ in Fig. 5e has a lower performance value but a higher decay rate and Fig. 5f shows the parameter set with the highest decay rate. As displayed in Fig. 5f this model has a poor performance compared to Fig. 5d and e.

The parameter values of $\mathbf{p}_{\text{init}}$, $\mathbf{p}_1$, $\mathbf{p}_2$ and $\mathbf{p}_3$ are summarized in Table 1. The lower part of Table 1 shows the parameter bounds of the NSGA-II genetic algorithm [37]. The lower parameter bounds have been chosen as displayed in Table 1 to avoid numerical problems (e.g. division by zero). The upper bounds were set because the tensile force T and the mass per unit length ρA are usually well known, whereas the bending stiffness EI and especially the material damping d_{mat} have to be identified experimentally. Furthermore ρA is constrained in a narrow band because it is the most sensitive parameter (see Section 3.1.2).

For this optimization a population size of 50 has been used and the average time per generation is $t \approx 0.2$ s on a standard PC (Intel i7). The displayed parameter sets were obtained after 100 generations.

Multiple runs using randomized initial values have been performed leading to overall good and consistent results even with noisy output data. The results of the optimization run displayed in Fig. 5 have been chosen to show a typical result with a evenly spread Pareto front, where all found parameter sets are stable.

This example shows that this multi-objective optimization based parameter identification is able to find stable solutions with optimal fit under difficult conditions (noisy and short data sequences). Furthermore, it is possible to directly decide if a solution is stable without requiring expert knowledge on the PDE or the parameter set itself. The performance-stability trade-off is clearly illustrated.

Table 1
Upper part: Parameter values of the initial and the identified parameters. Lower part: Parameter bounds used in this optimization run.

Parameter set	EI (N m^2)	T (N)	ρA (kg/m)	d_{mat} (N m^2 s)
$\mathbf{p}_{\text{init}}$	1.50×10^2	1.50×10^4	1.00	0.00
$\mathbf{p}_1$	2.88×10^2	1.24×10^4	1.32	8.47×10^{-1}
$\mathbf{p}_2$	2.85×10^2	1.38×10^4	7.38	9.19×10^{-1}
$\mathbf{p}_3$	2.82×10^2	1.49×10^4	1.25×10^1	8.40×10^{-1}
Parameter bounds				
Lower bound	10	1.00×10^4	0.5	0.00
Upper bound	∞	2.00×10^4	1.50	∞

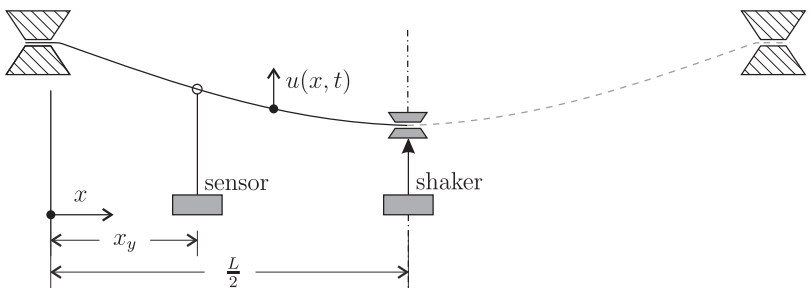

Fig. 6. Experimental setup for beam parameter identification.

3.2. Parameter identification using real measurement data

3.2.1. Problem setup and the testbed

In this validation example the multi-objective optimization will be performed for two performance objectives with two different sequences of excitation and measurement data. Each performance objective represents the fit for a different measurement sequence. A stability objective is not considered in this test case because the actual system is significantly damped and the model equation (13) is always stable for these measurement data.

The data have been measured on a laboratory testbed which was set up as shown in Fig. 6. The beam in this experimental setup fulfills the assumptions for the EBB theory from Section 2.1, so the model equation (1) can be used [38, Figs. 5.8, 5.9]. The beam has been mounted on a supporting frame. Static sag is not considered and removed in a data preprocessing step. To dynamically excite the beam, a shaker was positioned in the middle of the beam at $x = L/2$, where L is the beam length. Additionally, a sensor was placed at $x = x_y$. Due to the placement of the shaker at the middle, symmetry can be used and only one-half of the beam needs to be considered (the highlighted part in Fig. 6). Then, the shaker excitation can be modeled using a dynamic boundary condition (shaker *displacement* $f(t)$):

$$u(x,t)\big|_{x=0} = 0, \quad \frac{\partial u}{\partial x}(x,t)\big|_{x=0} = 0 \tag{49}$$

$$u(x,t)\big|_{x=L/2} = f(t), \quad \frac{\partial u}{\partial x}(x,t)\big|_{x=L/2} = 0. \tag{50}$$

The initial conditions are chosen as

$$u(x,t)\big|_{t=0} = 0 \tag{51}$$

$$\frac{\partial u}{\partial t}(x,t)\big|_{t=0} = 0. \tag{52}$$

Note that Eq. (51) is zero because the static sag (and gravity force terms) have been removed, thus u models the dynamic deviation from the static solution. With the boundary and initial condition equations (49)–(52), the EBB equation in Eq. (1) is well-defined and a state-space system equation (13) can be obtained.

3.2.2. Identifiability and parameter sensitivity

Due to the fact that only the displacement trajectory is available for excitation, it turns out that one parameter needs to be fixed to maintain identifiability. Then, the eigenvalues of the Fisher information matrix equation (18) for the resulting parameters have been verified to be strictly positive values, so the necessary identifiability condition in Definition 1 is fulfilled. Thus the Fisher information matrix is non-singular. The singular value decomposition equation (19) for the

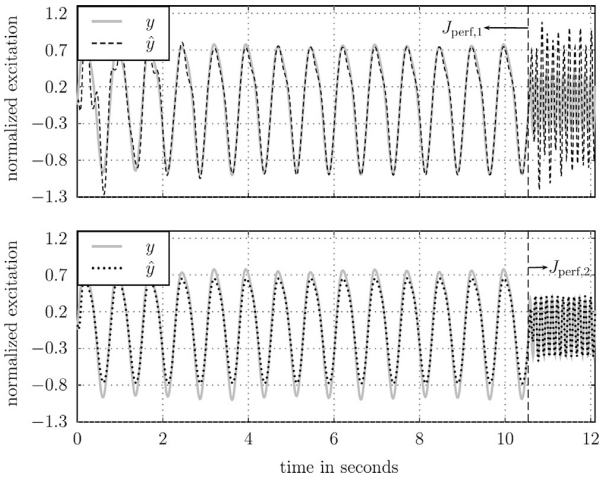

Fig. 7. Identification results for a pretensioned Euler–Bernoulli beam with measurement data. The best fit for $J_{\text{perf},1}$ (top) and the best fit for $J_{\text{perf},2}$ (bottom).

parameter vector $\mathbf{p} = [EI/\rho A, T/\rho A, d_{\mathrm{mat}}/\rho A]$ (d_v is assumed to be zero) yields

$$\mathbf{S} = \begin{bmatrix} 1.5901 \times 10^{-1} & 0 & 0 \\ 0 & 1.8187 \times 10^{-3} & 0 \\ 0 & 0 & 1.9067 \times 10^{-5} \end{bmatrix}, \tag{53}$$

$$\mathbf{V} = \begin{bmatrix} \approx 0 & 9.5871 \times 10^{-1} & 2.8439 \times 10^{-1} \\ \approx 0 & 2.8439 \times 10^{-1} & -9.5871 \times 10^{-1} \\ -1.0000 & \approx 0 & \approx 0 \end{bmatrix}. \tag{54}$$

These matrices show that the parameter $d_{\mathrm{mat}}/\rho A$ is most sensitive and the other two are coupled. Note that if parameter vector $\mathbf{p} = [\rho A, EI, T, d_{\mathrm{mat}}]$ would have been chosen, the material damping d_{mat} would not have been be identifiable. Thus the number of parameters is reduced by dividing by ρA on both sides of Eq. (1).

3.2.3. Identification results

Fig. 7a and b shows the comparison between the measured y and simulated model $\hat{y}$ outputs. Note that the identified data can be divided into two sequences. The chosen parameter sets are the best fit for the first sequence and the best for the second sequence, respectively. All other found parameter sets are a trade-off between these solutions. In the lower upper part of Fig. 7 the first sequence with a frequency at $f_1 \approx 1.5$ Hz is fitted better than the second sequence at $f_2 \approx 7.8$ Hz. The lower part of Fig. 7 shows a good fit for f_2.

The displayed parameter sets were obtained after 200 generations, with a average time per generation $t \approx 1.1$ s and a population size of 50.

The main advantage in using multiple performance objectives is that the model can be tuned for certain frequency ranges or signal forms a posteriori (i.e., without re-optimization).

4. Conclusions

A multi-objective parameter identification methodology of the bending dynamics for axially loaded Euler–Bernoulli beams is proposed. The identification problem is viewed from a multi-objective perspective which helps to understand the involved trade-off relations of the objectives.

Output error performance objectives as well as a stabilizing objective are proposed and developed, and criteria for unique identifiability (based on the Fisher information matrix) and for stability of the discretized solution are developed. Typically, few, simple measurements are sufficient to successfully identify the physical parameters.

A multi-objective genetic algorithm is utilized to solve the identification problem. It yields an approximation of the Pareto front of solutions.

Two specific test cases demonstrate the utility of the proposed multi-objective approach and the types of proposed objective functions: first, the stabilizing objective is seen to effectively produce stable solutions if only short, noisy data sequences produced by an undamped system are available. Also, a clear trade-off between performance and stability (margin) becomes evident. Second, measurement data of a real beam testbed are utilized to identify the beam model's parameters with low- and high-frequency performance objectives, clearly illustrating the performance trade-off.

Acknowledgment

This work has partially been financed by the Austrian Research Promotion Agency (FFG) under Grant no. 836449.

References

[1] Q. Leclère, C. Pézerat, Vibration source identification using corrected finite difference schemes, *Journal of Sound and Vibration* 331 (6) (2012) 1366–1377.
[2] R. Almeida, A. Urgueira, N. Maia, Identification of rigid body properties from vibration measurements, *Journal of Sound and Vibration* 299 (4–5) (2007) 884–899.
[3] A.S. Phani, J. Woodhouse, Experimental identification of viscous damping in linear vibration, *Journal of Sound and Vibration* 319 (3–5) (2009) 832–849.
[4] A. Bayón, F. Gascón, R. Medina, F. Nieves, F. Salazar, On the flexural vibration of cylinders under axial loads: numerical and experimental study, *Journal of Sound and Vibration* 331 (10) (2012) 2315–2333.
[5] N. Tullini, F. Laudiero, Dynamic identification of beam axial loads using one flexural mode shape, *Journal of Sound and Vibration* 318 (1–2) (2008) 131–147.

[6] G. Rebecchi, N. Tullini, F. Laudiero, Estimate of the axial force in slender beams with unknown boundary conditions using one flexural mode shape, *Journal of Sound and Vibration* 332 (18) (2013) 4122–4135.
[7] S. Li, E. Reynders, K. Maes, G.D. Roeck, Vibration-based estimation of axial force for a beam member with uncertain boundary conditions, *Journal of Sound and Vibration* 332 (4) (2013) 795–806.
[8] S. Law, Z. Lu, Time domain responses of a prestressed beam and prestress identification, *Journal of Sound and Vibration* 288 (4–5) (2005) 1011–1025.
[9] C. Lee, T. Kam, Identification of mechanical properties of elastically restrained laminated composite plates using vibration data, *Journal of Sound and Vibration* 295 (3–5) (2006) 999–1016.
[10] Y. Shi, H. Sol, H. Hua, Material parameter identification of sandwich beams by an inverse method, *Journal of Sound and Vibration* 290 (3–5) (2006) 1234–1255.
[11] S. Doebling, C. Farrar, M. Prime. A summary review of vibration-based damage identification methods, *Shock and Vibration Digest* 30 (2) (1998) 91–105.
[12] J. Park, Identification of damage in beam structures using flexural wave propagation characteristics, *Journal of Sound and Vibration* 318 (4–5) (2008) 820–829.
[13] Y. Haralampidis, C. Papadimitriou, M. Pavlidou, Multi-objective framework for structural model identification, *Earthquake Engineering Structural & Dynamics* 34 (6) (2005) 665–685.
[14] R. Perera, A. Ruiz, C. Manzano, An evolutionary multiobjective framework for structural damage localization and quantification, *Engineering Structures* 29 (10) (2007) 2540–2550.
[15] R. Perera, A. Ruiz, C. Manzano, Performance assessment of multicriteria damage identification genetic algorithms, *Computers & Structures* 87 (1) (2009) 120–127.
[16] S. Jung, S.-Y. Ok, J. Song, Robust structural damage identification based on multi-objective optimization, *International Journal for Numerical Methods in Engineering* 81 (6) (2010) 786–804.
[17] E. Zitzler, L. Thiele, Multiobjective evolutionary algorithms: *a comparative case study and the strength Pareto approach*, *IEEE Transactions on Evolutionary Computation* 3 (4) (1999) 257–271.
[18] A. Pandey, M. Biswas, Damage detection in structures using changes in flexibility, *Journal of Sound and Vibration* 169 (1) (1994) 3–17.
[19] H. Lam, J. Ko, C. Wong, Localization of damaged structural connections based on experimental modal and sensitivity analysis, *Journal of Sound and Vibration* 210 (1) (1998) 91–115.
[20] J. Horn, N. Nafpliotis, D.E. Goldberg, A niched Pareto genetic algorithm for multiobjective optimization, *Proceedings of the First IEEE Conference on Evolutionary Computation, 1994. IEEE World Congress on Computational Intelligence*, IEEE, Orlando, Florida, 1994, pp. 82–87.
[21] G.-H. Kim, Y.-S. Park, An improved updating parameter selection method and finite element model update using multiobjective optimisation technique, *Mechanical Systems and Signal Processing* 18 (1) (2004) 59–78.
[22] G. Goodwin, R. Payne, *Dynamic System Identification: Experiment Design and Data Analysis*, Academic Press, New York, 1977.
[23] C. Hametner, M. Stadlbauer, M. Deregnaucourt, S. Jakubek, T. Winsel, Optimal experiment design based on local model networks and multilayer perceptron networks, *Engineering Applications of Artificial Intelligence* 26 (1) (2013) 251–261.
[24] R. Higdon, Absorbing boundary conditions for difference approximations to the multi-dimensional wave equation, *Mathematics of Computation* 47 (176) (1986) 437–459.
[25] Y. Bistritz, A circular stability test for general polynomials, *Systems & Control Letters* 20 (1986) 89–97.
[26] S. Rao, *Vibration of Continuous Systems*, Wiley, Hoboken, New Jersey, USA, 2007.
[27] X. Yang, *Applied Engineering Mathematics*, Cambridge International Science Publishing Limited, Cambridge, UK, 2007.
[28] O. Bauchau, J. Craig, *Euler–Bernoulli beam theory, Solid Mechanics and its Applications*, vol. 163, Springer, Netherlands, 2009.
[29] R. LeVeque, *Finite Difference Methods for Ordinary and Partial Differential Equations: Steady-State and Time-Dependent Problems (Classics in Applied Mathematics Classics in Applied Mathematics)*, Society for Industrial and Applied Mathematics, Philadelphia, PA, USA, 2007.
[30] J. Strikwerda, *Finite Difference Schemes and Partial Differential Equations*, Wadsworth Publ. Co., Belmont, CA, USA, 1989.
[31] S. Kay, *Fundamentals of Statistical Signal Processing: Estimation Theory*, Prentice-Hall, Inc., Upper Saddle River, NJ, USA, 1993.
[32] L. Ljung (Ed.), *System Identification*: *Theory for the User*, 2nd ed. Prentice Hall PTR, Upper Saddle River, NJ, USA, 1999.
[33] L. Pronzato, Optimal experimental design and some related control problems, *Automatica* 44 (2) (2008) 303–325.
[34] K. Deb, D. Kalyanmoy, *Multi-Objective Optimization Using Evolutionary Algorithms*, John Wiley & Sons, Inc., New York, NY, USA, 2001.
[35] R. Marler, J. Arora, Survey of multi-objective optimization methods for engineering, *Structural and Multidisciplinary Optimization* 26 (6) (2004) 369–395.
[36] J.H. Holland, *Adaptation in Natural and Artificial Systems*, The University of Michigan Press, Oxford, England, 1975.
[37] K. Deb, A. Pratap, S. Agarwal, T. Meyarivan, A fast and elitist multiobjective genetic algorithm: *Nsga-ii*, *IEEE Transactions on Evolutionary Computation* 6 (2) (2002) 182–197.
[38] M. Sadd, *Wave Motion and Vibration in Continuous Media*, University of Rhode Island, Kingston, RI, 2009.

Publication B

Alexander Schirrer, Emir Talic, Guilherme Aschauer, Martin Kozek, Stefan Jakubek,
Optimization based determination of highly absorbing boundary conditions for linear finite difference schemes
Journal of Sound and Vibration, Volume 365, 2016, Pages 45–69, ISSN 0022-460X
DOI: 10.1016/j.jsv.2015.12.006

Author's contribution

Problem analysis, selection of methods, development of theoretical results, execution of the solution, development and programming of algorithms and performing simulation studies for the Euler-Bernoulli beam. Structuring, writing and editing of the manuscript was done by the applicant.

Journal of Sound and Vibration 365 (2016) 45–69

Contents lists available at ScienceDirect

Journal of Sound and Vibration

journal homepage: www.elsevier.com/locate/jsvi

Optimization based determination of highly absorbing boundary conditions for linear finite difference schemes

A. Schirrer, E. Talic*, G. Aschauer, M. Kozek, S. Jakubek

Inst. of Mechanics & Mechatronics, Vienna University of Technology, Getreidemarkt 9, 1060 Vienna, Austria

ARTICLE INFO

Article history:
Received 8 April 2015
Received in revised form
1 December 2015
Accepted 2 December 2015
Handling Editor: I. Lopez Arteaga
Available online 19 December 2015

Keywords:
absorbing boundary condition,
wave propagation

ABSTRACT

Many wave propagation problems (in acoustics or in railway catenary or cable car dynamics, for example) can be solved with high efficiency if the computational domain can be truncated to a small region of interest with appropriate absorbing boundary conditions. In this paper, highly absorbing and stable boundary conditions for linear partial differential equations discretized by finite difference schemes are directly designed using a flexible, optimization-based formulation. The proposed optimization approach to the computation of the absorbing boundary conditions is capable of optimizing the accuracy (the absorbing quality of the boundary condition) while guaranteeing stability of the discretized partial differential equations with the absorbing boundary conditions in place. Penalty functions are proposed that explicitly quantify errors introduced by the boundary condition on the solution of the bounded domain compared to the solution of the unbounded domain problem. Together with the stability condition the described approach can be applied on various types of linear partial differential equations and is thus applicable for generic wave propagation problems. Its flexibility and efficiency is demonstrated for two engineering problems: The Euler–Bernoulli beam under axial load, which can be used to model cables as well as catenary flexural dynamics, and a two-dimensional wave as commonly encountered in acoustics. The accuracy of the absorbing boundary conditions obtained by the proposed concept is compared to analytical absorbing boundary conditions.

1. Introduction

Many physical applications that show wave propagation phenomena, such as pressure waves in fluids, acoustic problems, or vibrations in strings and beams, are modeled by partial differential equations (PDEs) on bounded domains (clamped beam, sound waves in a chamber) or unbounded domains (long cables or catenaries, free sound wave propagation). To approximate the analytical solution the PDE is often discretized over a limited computational domain although the original problem may be defined on a much larger space. In order to obtain a well-posed problem suitable boundary conditions (BCs) and initial conditions (ICs) are needed. Choosing simple homogeneous BCs (Dirichlet/Neumann BCs respectively clamped BCs) is unsuitable in this setting because they fully reflect outgoing waves back into the domain. To avoid such spurious reflections into the domain of interest, the computational domain would have to be vastly expanded which

* Corresponding author. Tel.: +43 158801 325524.
E-mail addresses: alexander.schirrer@tuwien.ac.at (A. Schirrer), emir.talic@tuwien.ac.at (E. Talic), guilherme.aschauer@tuwien.ac.at (G. Aschauer), martin.kozek@tuwien.ac.at (M. Kozek), stefan.jakubek@tuwien.ac.at (S. Jakubek).

http://dx.doi.org/10.1016/j.jsv.2015.12.006
0022-460X/

drastically increases computational effort. Special so-called absorbing boundary conditions (ABCs) [1] have been proposed which ideally absorb outwards-traveling waves without reflections or the need to expand the computational domain. However, the analytic formulation of ABCs is not straightforward at all and heavily depends on the underlying PDE.

The finite difference (FD) method is one widely used technique to approximate the solution of the continuous PDE problem [2]. Its simple and flexible formulation relies on approximating the occurring partial derivatives by, for example, central differences, yielding an algebraic set of equations whose solution approximates the PDE's solution.

In this paper, an optimization-based method to obtain the unknown coefficients of a general explicit linear stencil for an ABC in the fully time/space-discretized FD problem is proposed. The method is illustrated by two examples — the Euler–Bernoulli beam (EBB) equation under axial load as well as the two-dimensional scalar wave equation.

ABCs for the wave equation have been investigated over the last decades. Well-known ABC formulations were developed by Engquist and Majda [3] and by Bayliss and Turkel [4]. The first approach is based on a factorization of the wave equation and leads to a non-local ABC, which must be transformed to a local ABC using pseudo-differential calculus in combination with truncated Taylor series, and the latter is based on a far-field asymptotic solution of the wave equation [5]. In Ref. [6] ABCs are developed for the FD approximation of a two-dimensional wave equation using the discrete dispersion relation. The same author developed radiation BCs for elastic and dispersive waves in the Refs. [7] and [8], respectively. Improvements led to local high-order ABCs [9], which have been applied on different types of wave equations, such as the time-dependent [10] and dispersive [11] cases. A review on high-order ABCs can be found in Givoli [12]. A different approach is the formulation of absorbing layers that expand the computational domain by an area with dissipating properties. These so-called sponge layers increase the damping in the absorbing layer to attenuate incident waves and can also be combined with ABCs [13]. In Ref. [14] sponge layers were used for the aeroacoustic time-reversal method to localize sound sources. A more advanced approach is the Perfectly Matched Layer (PML) [15] which uses a complex change of coordinates [16] to achieve high absorption performance, however at the cost of a considerable number of additional equations and variables to be solved in a time-marching scheme. The authors of Ref. [17] adopted the PML from Ref. [15] for the transition line method. The close relation of ABCs and PMLs is discussed in Ref. [9], and a combination of ABCs and PMLs has recently been presented in Hagstrom [18]. A historical overview on ABCs and PMLs is given in Berenger [19].

Developments related to ABCs for the EBB have been made in the field of boundary control of PDEs [20,21]. However, in Ref. [20] no axial load was considered when ABCs for the EBB were derived. The authors of Ref. [22] have successfully applied boundary control on an axially moving EBB under axial load, but their goal was to suppress vibrations by maximizing damping and energy absorption. In the present paper, ABCs for the FD-discretized EBB equation will be generated (in contrast to Ref. [20] an axial load is considered here). The goal of the optimized ABCs is to approximate the unbounded domain solution (not absorb energy as fast as possible as done in Lee [22]).

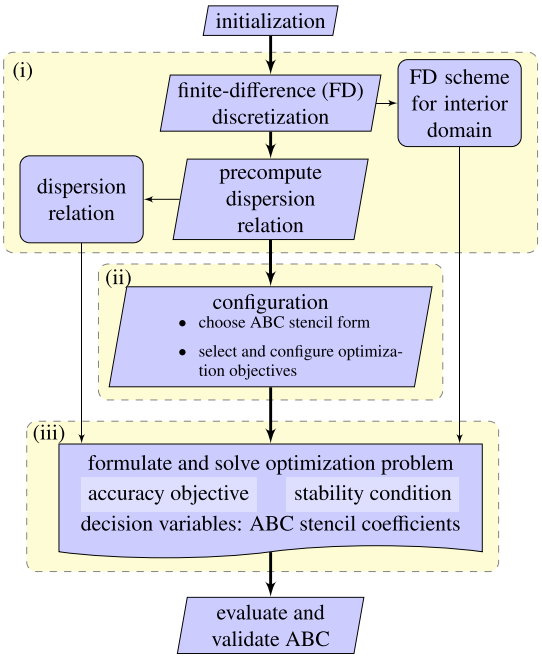

Fig. 1. Block diagram of the proposed method to obtain optimized ABC stencil coefficients.

The main contributions of this work are (a) a generic optimization approach to the determination of the ABC; (b) two accuracy objectives as well as one stability condition to allow the optimization to be carried out for generic wave propagation problems; and (c) the demonstration of the proposed method for two common engineering problems: the EBB equation *under axial load*, which to the best authors' knowledge has not yet been investigated in terms of ABCs in this configuration, and the two-dimensional scalar wave equation.

In contrast to the approaches available in literature, where the ABCs are typically developed for a specific PDE (and often in the continuous domain), here a generic method is proposed to directly obtain discrete ABC realizations for given discretization schemes of PDEs. This is done intentionally to avoid additional errors produced by discretizing a continuous ABC. Also, the method is generic in the sense that any large-scale reference system's solution could be utilized to fit the truncated system's response to. However, we make some basic assumptions in order to exploit problem structure and improve the method's efficiency. These assumptions are the PDE is linear with constant coefficients, has no (or, sufficiently low) damping, has a *harmonic traveling wave solution* [23,24], and its so-called *discrete dispersion relation* [6] can be derived (see Section 2.4).

The proposed optimization approach (main contribution (a)) consists of three major steps ((i), (ii) and (iii)) as illustrated in Fig. 1.

In step (i) the investigated PDE is approximated by standard central differences [25] using evenly spaced grids in space and time directions to obtain a set of algebraic equations. We denote the range of grid points that can be approximated by central differences as *interior domain* and the remaining grid points as *boundary points*. Each algebraic equation describes a relation between the unknown future (one-step-ahead) values and the known values of the solution. The pattern of these relations of points in the space–time grid is called *stencil* and the corresponding coefficients are called *stencil coefficients*. To perform numerically stable simulations the constant distances between two grid points in time and space directions — the so-called *step sizes* — have to be chosen appropriately. This choice of the space and the time step size is common to all FD problems and is, for example, guided by the von Neumann stability analysis or the Courant–Friedrich–Lewy's condition [2]. At this point, the dispersion relation can be precomputed and stored.

In step (ii) first the form of the *ABC stencil* for the boundary points has to be chosen. This choice is problem-dependent and may require a priori knowledge of the physical conditions under which the problem needs to be solved. Various stencil forms can be tested and optimized to obtain the best performing out of a limited number of candidates. For each time and space step size couple $\{\Delta t, \Delta x\}$ the ABC stencil has to be recomputed (or stored in advance) before running a simulation. Then an accuracy objective and a stability condition are selected and configured.

In step (iii) the optimization problem with the stencil coefficients as *decision variables* is formulated. One way is to set-up a single-objective optimization where just the accuracy of the ABCs is improved and stability is enforced through imposing a constraint. Standard single-objective optimization methods [26] such as pattern search [27] can then be utilized. The other possibility is to consider a multi-objective optimization (MOO) problem and to treat accuracy and stability as conflicting objectives. The MOO problem can, for example, be solved by population-based algorithms such as multi-objective genetic algorithms [28,29]. It is noted that population-based methods offer a set of solutions after the optimization which shows efficient trade-offs (of accuracy vs. stability). Either way, each solution defines a set of ABC stencil coefficients which directly constitute an ABC realization.

Two accuracy objectives and a stability condition are proposed (main contribution (b)). The first accuracy objective, here denoted as *reflection error*, expresses the magnitude of the reflection coefficient (RC) [30], which is ideally zero for all frequencies fulfilling the discrete dispersion relation of the interior domain stencil. The second proposed accuracy objective quantifies the amount of reflections of the harmonic wave solution of the FD scheme by the ABCs in an *output-error* sense [31].

In Refs. [32–34] FD-ABCs were used to stabilize simulations of wave propagation phenomena on unbounded domains over long time durations. To verify stability, eigenvalue analyses have been carried out in these references. However, the authors observed that optimizing ABCs using direct optimization (with accuracy objectives only) may lead to ABCs stencils that destabilize the system. Similar observations – concerning long-duration instabilities – have been made by Rabinovich in Ref. [35] in the field of elastodynamics for analytically derived ABCs. These instabilities have been delayed by introducing numerical damping in the same paper and eliminated by using special operators in Ref. [36]. In this paper, we adopt the eigenvalue analysis of the Refs. [32–34] for a fully discretized PDE. On that basis a stability objective evaluates the locations of the eigenvalues of a sufficiently large test system in state-space representation with the ABCs in place. In order to obtain an asymptotically stable FD scheme, all eigenvalues of the corresponding system matrix must lie inside the unit circle (see e.g. Ref. [37]).

The outline of this paper is: First, the basic effect of ABCs compared to standard Dirichlet and Neumann BCs is shown for the EBB under axial load by simulation. The influence of the two proposed accuracy objectives on the actual absorption properties is discussed, the choice of a stability objective vs. constraint is discussed, and the influence of frequency-weighting of the accuracy objective on the obtained ABC behavior is illustrated. Furthermore eigenvalue and sensitivity analyses will be performed for the one-dimensional case. The second example highlights the proposed method on the two-dimensional wave equation where the ABC stencil coefficients are optimized for certain angles of incidence and frequencies. The method is compared with the well-known Engquist–Majda-ABCs from Ref. [3].

2. Finite difference approximation of PDEs

The proposed method for obtaining the ABCs as an output of an optimization problem is directly applicable to PDEs being linear with constant coefficients, having no damping terms and for which harmonic traveling wave solutions exist (see Section 2.4). Additionally, some basic analytical treatment of the underlying PDE is performed. The necessary steps will be illustrated for the case of the EBB in this section, but are easily applicable to other PDEs modeling wave propagation phenomena. Furthermore, it is assumed that the update equation for the future time step can be written in an explicit form.

2.1. EBB under axial load

The PDE describing the dynamic behavior of a homogeneous EBB under axial load without damping is given by [38]

$$\begin{aligned} \rho A\frac{\partial^2 u}{\partial t^2} &= -EI\frac{\partial^4 u}{\partial x^4}+T\frac{\partial^2 u}{\partial x^2},\\ u=u(x,t),\quad x\in[0,L]\subseteq\mathbb{R},\quad t&\in\mathbb{R}^+\cup\{0\}, \end{aligned} \tag{1}$$

where the constant coefficients are the axial load T, the mass per unit length ρA, and the bending stiffness EI. The spatial variable is x, time is denoted by t, and the beam length is L. $u(x,t)$ denotes the vertical displacement of the beam.

2.2. Approximation of the interior domain

To numerically solve a PDE with the FD method the partial derivatives have to be approximated. To do so, the solution domain is divided into a uniform grid in space and time: $x\times t=[0,\Delta x,\ldots,N_x\Delta x]\times[0,\Delta t,\ldots,N_t\Delta t]$. Consequently, the variable $u(x,t)$ is only defined at each grid point ($u(x_k,t_n)=u_k^n$). The partial derivatives in (1) can then, for example, be approximated by finite differences [25]:

$$\frac{\partial^2 u}{\partial x^2}(x_k,t_n)\approx\frac{u_{k-1}^n-2u_k^n+u_{k+1}^n}{\Delta x^2}, \tag{2a}$$

$$\frac{\partial^2 u}{\partial t^2}(x_k,t_n)\approx\frac{u_k^{n-1}-2u_k^n+u_k^{n+1}}{\Delta t^2}, \tag{2b}$$

$$\frac{\partial^4 u}{\partial x^4}(x_k,t_n)\approx\frac{u_{k-2}^n-4u_{k-1}^n+6u_k^n-4u_{k+1}^n+u_{k+2}^n}{\Delta x^4}. \tag{2c}$$

Using central differences leads to symmetric stencil coefficients and it is assumed that the update equation producing the solution at each grid point for the next time step can explicitly be written as

$$u_k^{n+1}=\sum_{i=0}^{N_t^{\mathrm{INT}}-1}\sum_{j=-(N_x^{\mathrm{INT}}-1)/2}^{(N_x^{\mathrm{INT}}-1)/2}a_j^i u_{k+j}^{n-i}, \tag{3}$$

which is the case for central differences if no mixed derivatives appear in the PDE. Thereby, a_j^i are the stencil coefficients (see Fig. 2) and N_t^{INT}, N_x^{INT} are the numbers of time steps and spatial values needed to obtain the next solution value, respectively. In case of the EBB PDE (1), discretized with central differences (2), $N_t^{\mathrm{INT}}=2$ and $N_x^{\mathrm{INT}}=5$ hold. The coefficients a_j^i of (3) for the

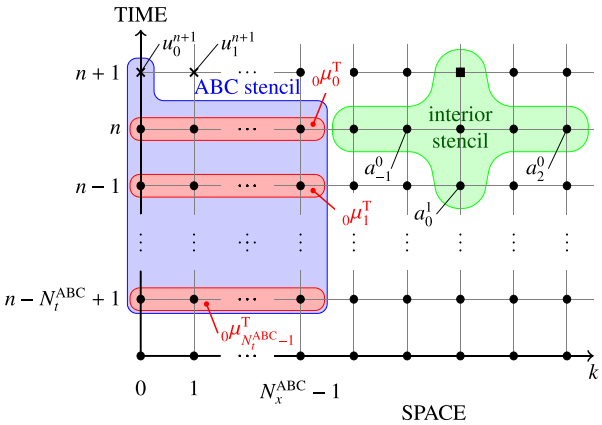

Fig. 2. Generic form of an explicit boundary condition stencil for $k=0$ (left) and an explicit interior stencil (right).

EBB PDE (1) are:

$$a^0_{\pm 2} = -\frac{EI\,\Delta t^2}{\rho A\,\Delta x^4}, \quad a^0_{\pm 1} = \frac{\Delta t^2\left(4\,EI + T\Delta x^2\right)}{\rho A\,\Delta x^4},$$
$$a^0_0 = \frac{-6\,EI\,\Delta t^2 - 2\,T\Delta x^2\Delta t^2 + 2\,\rho A\,\Delta x^4}{\rho A\,\Delta x^4},$$
$$a^1_0 = -1, \quad a^1_{\pm 1} = a^1_{\pm 2} = 0. \tag{4}$$

An example of such interior stencil structure is shown on the right side in Fig. 2.

2.3. Bounds for the time step size Δt

The FD scheme obtained above is conditionally stable [25]. For given physical parameters and spatial step size Δx, the time step size needs to fulfill $\Delta t \le \Delta t_{\max}$ to result in a stable scheme where numeric errors are not amplified over time. In case of a linear PDE with constant coefficients defined on an unbounded domain, the von Neumann stability analysis [25] can be applied to obtain this maximal time step size $\Delta t_{\max}$. For the EBB PDE (1) discretized by central differences (2), the following bound is obtained:

$$\Delta t_{\max} = \sqrt{\frac{\Delta x^4}{\frac{T}{\rho A}\Delta x^2 + 4\frac{EI}{\rho A}}}. \tag{5}$$

Remark 1. It is noted that $\Delta t_{\max}$ denotes a stability bound for the explicit FD time-marching scheme for the unbounded domain. Thus, the spatial and temporal step sizes are chosen a priori and are kept fixed during the optimization. To verify stability of the system with ABCs in place an eigenvalue analysis is performed (see Section 3.3). Moreover, Eq. (5) matches exactly the Courant–Friedrich–Lewy's condition (see Ref. [39]) for $EI = 0$.

2.4. Dispersion relation

For a PDE with traveling-wave-solutions the so-called *dispersion relation* on an unbounded domain can be derived if a harmonic wave of the form [23]

$$u(x,t) = \mathrm{e}^{\mathrm{I}(\omega_x x + \omega_t t)} \tag{6}$$

is a solution of the homogeneous PDE, where I is the imaginary unit and $\omega_x, \omega_t \in \mathbb{R}$. It is noted that this corresponds to an oscillatory traveling wave solution of an undamped problem. The dispersion relation describes the connection between the spatial frequency or wave number $\omega_x \in \mathbb{R}$ (or the wave vector $k = [\omega_x, \omega_y, \ldots]^{\mathrm{T}}$ in the higher-dimensional case) and the temporal frequency $\omega_t \in \mathbb{R}$. The general form of this relation is

$$f(\omega_t, \omega_x) = 0. \tag{7}$$

Likewise, using the discrete counterpart of (6),

$$u^n_k = \left(\mathrm{e}^{\mathrm{I}\omega_x \Delta x}\right)^k \left(\mathrm{e}^{\mathrm{I}\omega_t \Delta t}\right)^n = \kappa^k \tau^n, \tag{8}$$

the so-called *discrete dispersion relation* [6] can be derived by substituting (8) into an FD-discretized PDE.

To shorten notation, the dependency of κ and τ on ω_x and ω_t, respectively, will not be explicitly written in the remainder of the paper. Also it is noted that because of the linearity of the PDEs under investigation, the sum of harmonic waves is again a solution, hence the full solution can be written as a superposition of (infinitely) many harmonic wave solutions. Here, evanescent modes are not considered relevant in the formulation of ABC accuracy (as also argued in[11]).

For the EBB the discrete dispersion relation is obtained by combining (3), (4) and (8) and leads after simplifications to:

$$\sin^2\left(\frac{\omega_t \Delta t}{2}\right) = \frac{T}{\rho A}\frac{\Delta t^2}{\Delta x^2}\sin^2\left(\frac{\omega_x \Delta x}{2}\right) + \frac{EI}{\rho A}\frac{\Delta t^2}{\Delta x^4}\sin^4\left(\frac{\omega_x \Delta x}{2}\right). \tag{9}$$

2.5. Boundary conditions

In order to obtain a well-posed PDE problem, suitable initial conditions (ICs) and BCs are needed. These ICs and BCs have to be discretized as well if the solution is approximated using discrete numerical methods such as FD.

Fig. 2 shows a possible computation grid where an interior stencil is shown on the right side. This stencil cannot be used to compute the solution values at the boundary because it would rely on undefined grid points outside the computational domain. The number of boundary grid points N_{ABC} to compute depends on the spatial width of the interior stencil. For the explicit computation of the boundary grid points a generic explicit ABC stencil (on the left of Fig. 2) is introduced (here,

shown for the left boundary formulation throughout):

$$u_k^{n+1} = \sum_{i=0}^{N_t^{\mathrm{ABC}}-1} {}_k\boldsymbol{\mu}_i^{\mathrm{T}} \begin{bmatrix} u_0^{n-i} \\ \vdots \\ u_{N_x^{\mathrm{ABC}}-1}^{n-i} \end{bmatrix}, \quad k = 0, \ldots, N_{\mathrm{ABC}} - 1, \tag{10}$$

where ${}_k\boldsymbol{\mu}_i^{\mathrm{T}} \in \mathbb{R}^{N_x^{\mathrm{ABC}}}$ denotes the vector of stencil coefficients for the $(n-i)$th time instant needed for the computation of the kth spatial grid point's value. N_t^{ABC} is the number of time instants that are needed for the ABC stencil computation and N_{ABC} is the number of boundary grid points. ABC stencils on the right boundary are defined analogously by spatially mirroring the entries of ${}_k\boldsymbol{\mu}_i^{\mathrm{T}}$.

3. Methodology

3.1. Basic considerations

Unlike the common approaches in the literature, where the ABCs are derived by physical considerations, in this work the determination of the stencil coefficients of the ABCs is formulated as an optimization problem. Therefore, two different accuracy objectives and one stability condition are introduced. Only taking accuracy objectives into account may lead to well-performing ABCs that, however, possibly introduce unstable dynamics. In these cases a stable parameter set can be enforced by adding a stabilizing objective or a stabilizing constraint. On the one side, using a stabilizing constraint a single objective optimization problem occurs and its solution is a stable candidate (ABC stencil). Depending on the single-objective optimization method and the starting point of the optimization a global minimum of the accuracy objective can be obtained. On the other side, formulating a stabilizing objective instead results in a MOO problem. Its solution is a set of candidates, where accuracy and stability can be traded against each other.Additionally, a number of different stencil forms can be tested and the trade-off between complexity, accuracy, and stability margin becomes clearly visible.

Moreover, the accuracy objectives can include weighting functions, introducing additional design degrees of freedom and thus the possibility to optimize the ABCs for specific application needs. Examples are the frequency of waves or the angle of incidence of waves reaching the boundary for the two-dimensional wave equation.

The proposed objective functions will be shown and derived for the one-dimensional case to simplify notation. However, their generalization to the higher-dimensional case is straightforward and will be sketched in Section 4.2.1.

3.2. Accuracy objectives

Two accuracy objectives are proposed that are based on the error made at the boundary with respect to the outgoing harmonic wave solutions, and thus they quantify the difference between the bounded and unbounded domain solutions.

3.2.1. Accuracy objective — reflection coefficient (RC)

The reflection coefficient (RC) was introduced in Ref. [6] to describe the reflection properties of ABCs. The derivation of the RC will be outlined here and extended for arbitrary boundary points u_k^{n+1}, with $k = 0, \ldots, N_{\mathrm{ABC}} - 1$. The basic idea is to

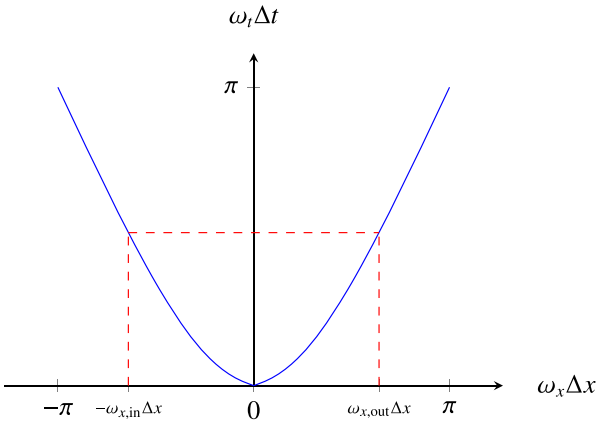

Fig. 3. The discrete dispersion relation for EBB equation for positive $\omega_t \Delta t$ with $EI = 150$ N m^2, $T = 15{,}000$ N/m, $\rho A = 1$ kg/m, $\Delta t = 9.9 \times 10^{-5}$ s and $\Delta x = 0.05$ m.

consider boundary conditions of the following form:

$$B_k(\tau,\kappa)u_k^{n+1}=0,\quad k=0,\ldots,N_{\mathrm{ABC}}-1 \tag{11}$$

$B_k(\tau,\kappa)$ is obtained by inserting (8) into (10) and expressing the boundary point of interest. This leads to

$$B_k(\tau,\kappa)=1-\sum_{n=0}^{N_t^{\mathrm{ABC}}-1} {}_k\boldsymbol{\mu}_n^{\mathrm{T}}\begin{bmatrix}\tau^{-(n+1)}\kappa^{-k}\\ \tau^{-(n+1)}\kappa^{-k+1}\\ \vdots\\ \tau^{-(n+1)}\kappa^{-k+N_x^{\mathrm{ABC}}-1}\end{bmatrix}. \tag{12}$$

To study the reflection properties, one considers the linear combination

$$u_k^n=c_{\mathrm{in}}\kappa_{\mathrm{in}}^k\tau^n+c_{\mathrm{out}}\kappa_{\mathrm{out}}^k\tau^n \tag{13}$$

where $\kappa_{\mathrm{in}}^k=\exp(I\omega_{x,\mathrm{in}}\Delta x)$ and $\kappa_{\mathrm{out}}^k=\exp(I\omega_{x,\mathrm{out}}\Delta x)$ are chosen to correspond with the incoming and outgoing wave components (understood as having positive and negative group velocities, respectively [6]) with amplitudes c_{in} and c_{out}. The spatial frequencies $\omega_{x,\mathrm{in}}$ and $\omega_{x,\mathrm{out}}$ are obtained from the discrete dispersion relation (7). The discrete dispersion relation for the EBB (9) is displayed in Fig. 3. The $\omega_t\Delta t(\omega_x\Delta x)-$branch with different signs of $\omega_t\Delta t$ and $\omega_x\Delta x$ represents the incoming and the branch with the same sign the outgoing wave components, with positive and negative group velocities, respectively. The group velocity is defined as

$$v_{\mathrm{group}}=-\frac{\partial\omega_t}{\partial\omega_x}. \tag{14}$$

Finally, one obtains the RC by inserting (12) into (13) which leads to

$$c_{\mathrm{in}}B_k(\tau,\kappa_{\mathrm{in}})+c_{\mathrm{out}}B_k(\tau,\kappa_{\mathrm{out}})=0 \tag{15}$$

or

$$c_{\mathrm{in}}=\underbrace{-\frac{B_k(\tau,\kappa_{\mathrm{out}})}{B_k(\tau,\kappa_{\mathrm{in}})}}_{R_k(\omega_t\Delta t,\omega_x\Delta x)}c_{\mathrm{out}}. \tag{16}$$

with the RC R_k. It is evident that the RC is a function of κ and τ and is evaluated for certain pairs of $(\omega_t\Delta t,\omega_x\Delta x)$, which are related by the discrete dispersion relation. The goal for the optimization is to minimize $|R_k|$. Consequently, the first proposed accuracy criterion aggregates (16) over all relevant frequencies $\omega_x\in[0,\pi/\Delta x]$ (up to the Nyquist frequency) with a user-defined frequency weighting $w(\omega_x)\geq 0$:

$$J_{\mathrm{perf,RC}}=\sum_{k=0}^{N_{\mathrm{ABC}}-1}\int_0^{\pi/\Delta x} w(\omega_x)|R_k(\omega_x)|\,\mathrm{d}\omega_x. \tag{17}$$

In the particular cases of the EBB and the two-dimensional wave equation the dispersion relation is symmetric with respect to the ω_t-axis (see Fig. 3) and $\omega_x=-\omega_{x,\mathrm{in}}=\omega_{x,\mathrm{out}}$. Thus, the integral in (17) needs only be evaluated in the given interval.

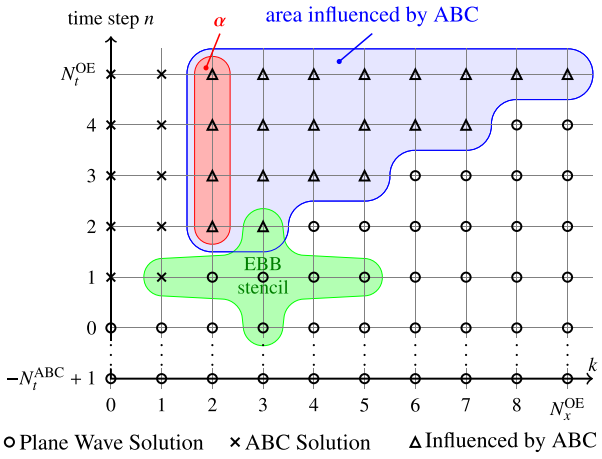

Fig. 4. Influence of an ABC stencil for the EBB into the interior domain.

3.2.2. Accuracy objective — output-error (OE)

The second proposed accuracy objective is based on simulating a harmonic wave solution on a (small) test domain with ABCs in place for several time steps and comparing a selected region of the solution to that of the unbounded domain which is directly available from (8). While the RC accuracy objective (16) minimizes the reflection of the boundary points for the frequency pairs (ω_t, ω_x) of the discrete dispersion relation (7), the OE accuracy objective minimizes the harmonic wave solution error in an output-error sense [31]. The concept behind the OE accuracy objective is sketched in Fig. 4 for the example of an EBB explicit interior stencil. Each grid point u_k^n at the time instants $n = 0, -1, \ldots, -N_t^{\mathrm{ABC}}+1$ is initialized with the harmonic wave solution (8). These grid points are marked by circles (○). The boundary grid points (see Fig. 4, $k = 0, 1$) where the solution is computed using the ABC stencils are indicated by crosses (×). Grid points that are influenced by boundary point values are marked by triangles (△) in Fig. 4. The idea is to minimize the difference of the solution marked with △ or a restricted area (e.g. α with $k = 2$ in Fig. 4) and the harmonic wave solution (8) on the unbounded domain. The output error of one harmonic wave solution is thus expressed as

$$e_{\mathrm{OE}} = \sum_{n=2}^{N_t^{\mathrm{OE}}} \sum_{k=2}^{N_x^{\mathrm{OE}}} \left| u_k^n - \kappa^k \tau^n \right|^2, \tag{18}$$

and the solutions u_k^n are obtained from numeric solution of the test system. It is noted that the solution is let to evolve over N_t^{OE} time steps (in contrast to the 1-step evaluation of the RC accuracy objective (17)). The proposed OE objective again is obtained by aggregating the error function (18) over frequency:

$$J_{\mathrm{perf,OE}} = \int_0^{\pi/\Delta x} w(\omega_x) e_{\mathrm{OE}}(\omega_x)\, \mathrm{d}\omega_x. \tag{19}$$

3.3. Stability condition

Eq. (5) stated the von Neumann (Fourier) stability criterion for the EBB as an upper bound on the step size Δt to guarantee a stable FD scheme on an unbounded domain. Specific BCs can, however, still introduce instability. Therefore, a dedicated stability condition is introduced.

Thisstability condition evaluates the eigenvalues of the state-space system associated to an FD-approximated test system with applied ABCs. Every solution value at the time instant n is collected into

$$\mathbf{u}^n = \left[u_0^n,\ u_1^n,\ \ldots,\ u_{N_x-1}^n \right]^{\mathrm{T}}. \tag{20}$$

Since there are two time steps involved in (4) for the EBB and possibly more for the ABC stencil (10), the state vector has to contain earlier values as well, depending on the highest number N_t^{up} of time steps appearing in the update equations:

$$\mathbf{v}^n = \left[\left(\mathbf{u}^n\right)^{\mathrm{T}},\ \left(\mathbf{u}^{n-1}\right)^{\mathrm{T}},\ \ldots,\ \left(\mathbf{u}^{n-N_t^{\mathrm{up}}+2}\right)^{\mathrm{T}} \right]^{\mathrm{T}}. \tag{21}$$

This augmented state vector then consists of $(N_t^{\mathrm{up}}-1)N_x$ elements and the update equation can be written in the following form:

$$\mathbf{v}^{n+1} = \mathbf{A}\mathbf{v}^n, \tag{22}$$

with the discrete-time system matrix $\mathbf{A} \in \mathbb{R}^{((N_t^{\mathrm{up}}-1)N_x)\times((N_t^{\mathrm{up}}-1)N_x)}$, incorporating the discretized PDE (3), as well as the update equation (10) for the boundary grid points and the past time steps $\mathbf{u}^{n-1}, \ldots, \mathbf{u}^{n-N_t^{\mathrm{up}}+2}$.

The solution eigendynamics on each grid point is entirely described by $\mathbf{A}$ and linear system theory can readily be applied to study stability. In fact, a discrete-time system of the form (22) is asymptotically stable if and only if all eigenvalues of the state matrix $\mathbf{A}$ lie within the unit circle, i.e. have magnitude smaller than one [37], leading to the stability constraint

$$\rho(\mathbf{A}) = \max_i |\lambda_i(\mathbf{A})| < 1, \tag{23}$$

which can also be addressed in the optimization in the form of a stability objective:

$$J_{\mathrm{stab}} = \rho(\mathbf{A}). \tag{24}$$

It is noted that the value $J_{\mathrm{stab}} < 1$ corresponds to a positive stability margin and quantifies the global exponential decay rate. The accuracy/stability margin trade-off is made visible by taking on the MOO formulation. Furthermore, this condition evaluates asymptotic stability for a concrete implementation. However, it is assumed that the stability properties of the boundary region affect small and large systems in the same way which has been empirically observed by the authors.

For the undamped wave and EBB PDEs, central differences with applied Dirichlet/Neumann BCs lead to a unimodal system (all eigenvalues have magnitude one), independent of the number of interior grid points.

Remark 2. The ABC stencils may also be formulated implicitly, leading additionally to stencil coefficients ${}_k\boldsymbol{\mu}_1^{\mathrm{T}}$ on the left hand side of Eq. (10). Consequently this leads to an implicit state space representation $\mathbf{M}\mathbf{v}^{n+1} = \mathbf{A}\mathbf{v}^n$ (compare Eq. (22)).

3.4. Single-objective optimization

By choosing one of the accuracy objectives (17) or (19) together with the stability constraint (24), a suitable optimization problem for the determination of well-performing and stable ABCs can be stated. Mathematically, a parameter vector $\mathbf{p} = \{{}_k\boldsymbol{\mu}_i\}$, $k = 0, \ldots, N_{\mathrm{ABC}} - 1$, $i = 0, \ldots, N_t^{\mathrm{ABC}} - 1$, consisting of the $N_p = N_{\mathrm{ABC}} \times N_t^{\mathrm{ABC}} \times N_x^{\mathrm{ABC}}$ stencil coefficients in the ${}_k\boldsymbol{\mu}_i^{\mathrm{T}}$ vectors of (10) is sought that minimizes a cost function $J = J_{\mathrm{perf}}(\mathbf{p})$:

$$\begin{aligned} \min_{\mathbf{p}} \quad & J(\mathbf{p}) \\ \text{subject to} \quad & \rho(\mathbf{A}) < 1 \end{aligned} \tag{25}$$

where $\mathbf{p} \in \mathbb{R}^{N_p}$ and $J \in \mathbb{R}$. In this work a pattern-search algorithm [27] was utilized for solving the optimization problem. Pattern-search belongs to the class of gradient-free optimization methods but only one solution candidate is considered. This solution is iteratively improved by evaluating the objective function in its neighborhood at points having a fixed distance to the current solution, called mesh size. If a better point is found, it is denoted as the new solution and the mesh size is doubled (exploration). If, after evaluating the neighborhood, the current point is still optimal, the mesh size is reduced (intensification). This process is repeated until the mesh size reaches a lower tolerance value.

3.5. Multi-objective optimization (MOO)

By incorporating the stability objective (24) into the optimization problem and treating it equally to the accuracy objective MOO results. Stencil coefficients are sought that minimize a vector-valued cost function $\mathbf{J} = [J_{\mathrm{perf}}(\mathbf{p}),\ J_{\mathrm{stab}}(\mathbf{p})]^{\mathrm{T}}$ in the Pareto sense [40]:

$$\min_{\mathbf{p}} \mathbf{J}(\mathbf{p}), \quad \mathbf{p} \in \mathbb{R}^{N_p}, \ \ \mathbf{J} \in \mathbb{R}^2. \tag{26}$$

Typically, the two objectives are conflicting. Each solution candidate that cannot be further improved in one objective without deteriorating the other objective is called Pareto optimal [28]. The result of the MOO problem solved by population-based approaches is an approximation of the Pareto-optimal solution set (called Pareto front). In this work the MOO problem (26) is solved by a multi-objective genetic algorithm (NSGA-II [29]). Genetic algorithms belong to the class of evolutionary algorithms and are inspired by nature's evolution process. They use a set of solution candidates, called *population*, and improve it iteratively. Each iteration, called *generation*, is evolved by the operations *selection*, *recombination*, and *mutation*. Initial solutions can be obtained by single-objective optimization, via randomization, or by using already known ABCs.

4. Numerical results

Using an EBB test system, a simulation run illustrates the wave absorption with an ABC in place. The two accuracy objectives will be compared and their properties discussed. Furthermore, the frequency-weighting of the accuracy objectives and its influence on the time-domain results will be illustrated. For the two-dimensional wave equation first the ABC optimization method is adopted to the two-dimensional case and the optimized ABCs are compared with the second-order Engquist–Majda ABCs.

4.1. ABCs for the Euler–Bernoulli Beam (EBB) equation under axial load

The EBB model plays an important role in modeling bending beam dynamics. Its applications are found, for example, in cable car and railway catenary dynamics. Furthermore, the EBB equation is particularly challenging because physical dispersion is significant.

4.1.1. EBB parameters and system setup

For the following studies the coefficients of the EBB equation (1) were chosen corresponding to typical high-speed railway catenary contact wire parameters [41]:

$$T = 1.5 \times 10^4 \text{ N}, \quad \rho A = 1 \text{ kg/m}, \quad EI = 150 \text{ N m}^2,$$

and the beam length is chosen with $L = 100$ m. The simulation setup is structured as follows: ABC stencils are placed at the left boundary ($x = 0$ m) and a clamping BC was chosen for the right boundary ($x = L$). The homogeneous clamping BC is here defined as

$$u(L, t) = 0, \quad \frac{\partial u}{\partial x}(L, t) = 0, \tag{27}$$

and can be realized by using FDs as

$${}_{Nx}\boldsymbol{\mu}_0^{\mathrm{T}} = [0 \ \ 0 \ \ 0 \ \ 0], \quad {}_{Nx-1}\boldsymbol{\mu}_0^{\mathrm{T}} = [0 \ \ 0 \ \ 0 \ \ 0]. \tag{28}$$

Because of the fourth derivative in the EBB PDE (1) which is discretized by (2), two boundary grid points on each side arise, and so two ABC stencils need to be optimized. The stencil size parameters of the ABCs are chosen as $N_x^{\mathrm{ABC}}=4$ and $N_t^{\mathrm{ABC}}=1$ (see Fig. 2). Furthermore, the spatial step size of the computational grid was chosen with $\Delta x=0.05$ m, and $\Delta t=\Delta t_{\max}=9.9\times10^{-5}$ s was determined from (5). The simulation runs are started with the ICs

$$u(x,0)=\begin{cases}\sin^2\left(\pi\left(\dfrac{x-x_c}{d}-\dfrac{1}{2}\right)\right) & -\dfrac{d}{2}\le x-x_c\le\dfrac{d}{2}\\ 0 & \text{elsewhere,}\end{cases} \tag{29a}$$

$$\frac{\partial u}{\partial t}(x,0)=0, \tag{29b}$$

with $x_c=25$ m and $d=0.5$ m. The IC is displayed in Fig. 5 as the topmost curve.

Remark 3. Setting $\Delta t=\Delta t_{max}$ may cause numerical problems as floating point computations made by computers during the simulations can introduce small errors possibly leading to $\Delta t>\Delta t_{max}$.

4.1.2. MOO parameters and objectives

Throughout this example the MOO problem (26) is utilized for obtaining the ABC stencil coefficients. If not stated otherwise, the MOO parameters and objectives are configured as follows:

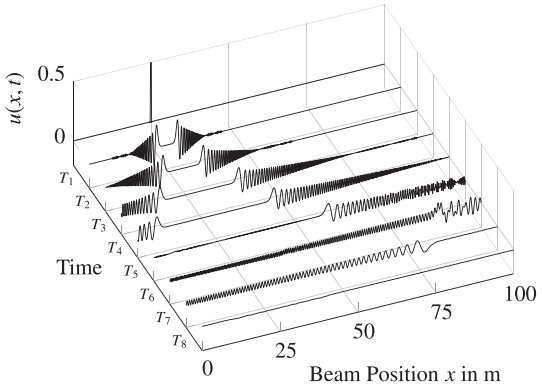

Fig. 5. Displacements $u(x,t)$ of the pretensioned EBB for selected simulation times. $x=0$ m: ABC applied, $x=100$ m: clamping BC applied

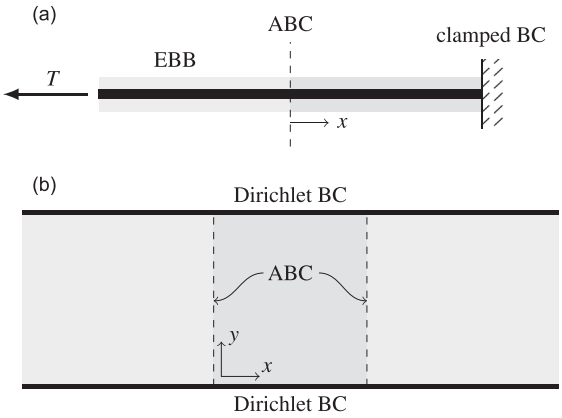

Fig. 6. Elongated reference domains (light gray) and ABC-bounded computational domains (dark gray) for the two examples: (a) EBB under axial load, (b) two-dimensional wave equation.

- The MOO problem is solved by a multi-objective genetic algorithm with a population size of 100 individuals. Thus, the solution represents that of a single objective (best accuracy) optimization problem with a stability constraint (24), however, the MOO treatment allows direct insight into the accuracy/stability-margin trade-off.
- Only the best performing stable solution of the optimized, final solution set is considered.
- The RC (17) and OE (19) accuracy objectives are evaluated at a frequency grid $\omega_x \in [0, \pi/10\Delta x, 2\pi/10\Delta x, \ldots, \pi/\Delta x]$.
- The stability objective (24) is calculated using a small test system ($\mathbf{A} \in \mathbb{R}^{10\times 10}$ of the system (22)).
- The OE accuracy objective (19) is evaluated using $N_t^{\mathrm{OE}} = 5$ and $N_x^{\mathrm{OE}} = 15$ (see Fig. 4).
- Frequency weighting is only considered in Section 4.1.6, in all other sections it is set to $w(\omega_x) = 1$.

4.1.3. Quantification of the absorption properties and long-term stability

The absorption properties of the ABCs are quantified by means of the time-dependent approximated error [35]

$$e(t) = \frac{\|\mathbf{u}(t) - \mathbf{u}_{\mathrm{ref}}(t)\|_{[0,L]}}{L} \tag{30}$$

and the approximated global relative space–time error

$$E = \frac{\|\mathbf{u} - \mathbf{u}_{\mathrm{ref}}\|_{[0,L],[0,T_{\mathrm{SIM}}]}}{\|\mathbf{u}_{\mathrm{ref}}\|_{[0,L],[0,T_{\mathrm{SIM}}]}}. \tag{31}$$

Therefore a reference solution $\mathbf{u}_{\mathrm{ref}}$ – based on the same interior discretization – is computed using a one-sided elongated simulation setup (see Fig. 6a). The elongated setup $-mL \le x \le L$ has clamped boundary condition on both sides. Its elongation factor $m \in \mathbb{N}\backslash\{0\}$ is chosen such that no reflection of the left boundary enter the truncated simulation domain ($0 < x < L$) during the simulation time T_{sim}. The errors (30) and (31) are calculated using the L_2-norm $\|\cdot\|_{\mathcal{M}}$ evaluated on the manifold $\mathcal{M}$.

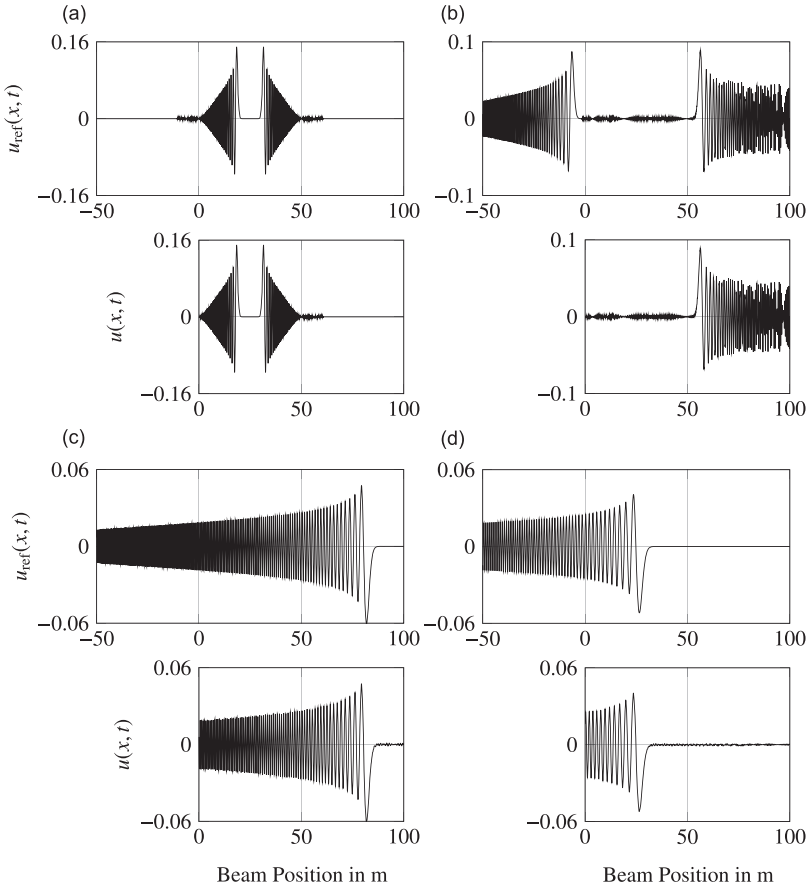

Fig. 7. Comparison of the reference solution $u_{\mathrm{ref}}(x,t)$ (top) and solution with applied ABCs $u(x,t)$ (bottom) at: (a) $t = 0.05$ s, (b) $t = 0.25$ s, (c) $t = 0.75$ s and (d) $t = 1.25$ s.

In comparison to the one-dimensional time-dependent error in Ref. [35], here the error (30) is normalized by L instead of $\sqrt{L}$. This choice renders $e(t)$ dimensionless.

To verify that the proposed ABCs are stable, long-term simulations will be performed and quantified by the total energy remaining in the system. The total energy remaining in the system is defined as the sum of kinetic energy E_{kin} and potential energy E_{pot} (see in Ref. [23])

$$E_{\mathrm{tot}}(t) = E_{\mathrm{kin}}(t) + E_{\mathrm{pot}}(t) = \int_0^L \underbrace{\left(\epsilon_{\mathrm{kin}}(x,t) + \epsilon_{\mathrm{pot}}(x,t)\right)}_{\epsilon_{\mathrm{tot}}(x,t)} \mathrm{d}x, \tag{32a}$$

with the total energy per unit length $\epsilon_{\mathrm{tot}}(x,t)$ and its kinetic and potential contributions

$$\begin{aligned} \epsilon_{\mathrm{kin}}(x,t) &= \frac{1}{2}\rho A\left(\frac{\partial u(x,t)}{\partial t}\right)^2, \\ \epsilon_{\mathrm{pot}}(x,t) &= \frac{1}{2}\left[T\left(\frac{\partial u(x,t)}{\partial x}\right)^2 + EI\left(\frac{\partial^2 u(x,t)}{\partial x^2}\right)^2\right]. \end{aligned} \tag{32b}$$

$E_{\mathrm{tot}}(t)$ is computed by approximating the derivatives by central differences and the integration by the trapezoidal rule.

4.1.4. Demonstration of wave absorption

The wave absorption properties of an optimized ABC are demonstrated. The ABC stencil coefficients

$${}_0\boldsymbol{\mu}_0^{\mathrm{T}} = \left[2.3401 \times 10^{-1} \;\; 9.9202 \times 10^{-1} \;\; -2.3323 \times 10^{-1} \;\; -1.6615 \times 10^{-3}\right], \tag{33a}$$

$${}_1\boldsymbol{\mu}_0^{\mathrm{T}} = \left[6.3487 \times 10^{-2} \;\; 2.5289 \times 10^{-1} \;\; 9.3493 \times 10^{-1} \;\; -2.5498 \times 10^{-1}\right], \tag{33b}$$

are applied on the left boundary ($x = 0$ m) and were obtained by solving the MOO (26) using the RC accuracy objective (17) and the stability objective (24). The stability margin for the ABC stencil (33) is $1 - J_{\mathrm{stab}} \approx 9.6769 \times 10^{-5}$ and the accuracy objective value is $J_{\mathrm{perf,RC}} \approx 8.6661 \times 10^{-2}$. The clamped BC (28) is applied on the right boundary ($x = 100$ m).

Fig. 5 visualizes the displacement of the EBB at selected time instances $T_1 < T_2 < \cdots < T_8$, where the topmost curve depicts the IC (29a).

Time T_1 shows that the initial wavelet has split into two wave packets, traveling leftward and rightward. Additionally, the physical dispersion of the EBB which separates low- and high-frequency content due to differing propagation speeds is clearly visible. Here, high frequency components travel faster than low frequency components. At times T_2, T_3 and T_4 the wave packet running leftward towards the ABC at $x = 0$ m is absorbed while the right wave packet (running towards $x = 100$ m) disperses further (seen at times T_2, T_3) and at time T_4 it starts to be totally reflected by the clamping BC (28). At times $T_5, \ldots, T_8$ the total reflection at the right boundary and the subsequent absorption on the left is shown.

A more detailed view is given in Fig. 7, where the solution $u(x,t)$ with ABCs applied and the reference solution $u_{\mathrm{ref}}(x,t)$ are shown for selected time instances. Each plot therein consists of the reference solution (top) and the truncated ABC-bounded solution (bottom). It is noted that $u_{\mathrm{ref}}(x,t)$ has been calculated on a significantly elongated domain $-1000\ \mathrm{m} \le x \le 100\ \mathrm{m}$, but only $-50\ \mathrm{m} \le x \le 100\ \mathrm{m}$ are shown for clarity. As one can see in Fig. 7, the IC (29a) has a rich

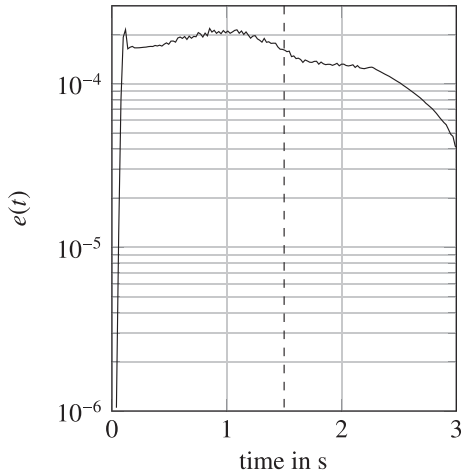

Fig. 8. Time-dependent error $e(t)$ of the EBB ABC. The dashed line marks the time when the IC has entirely left the truncated domain ($t = 1.5$ s).

frequency content. However, the agreement of the reference solution and the truncated solution is very good. The time-dependent error $e(t)$ is given in Fig. 8 and quantifies the degree of absorption. It is initially zero until the leftwards traveling wave packet reaches the boundary at $x = 0$ m ($t \approx 0.05$ s). Then, the value of $e(t)$ stays approximately constant as long as significant signal content remains in the truncated domain ($0\text{ m} \leq x \leq 50\text{ m}$). For $t \geq 1.5$ s the displacement of the reference solution is equal to zero inside the truncated domain (dashed line in Fig. 8) and the error $e(t)$ decreases again over time.

One important aspect of ABC quality is long-term stability. Ref. [35] reports on the asset of long-term stability. To verify that no such behavior occurs a simulation run of 200 s (two orders of magnitude longer than the time the IC needs to leave the truncated domain in this example) was performed and the total energy $E_{\text{tot}}(t)$ (32a) was calculated. The result is displayed in Fig. 9, demonstrating that the total energy E_{tot} decays and the ABC-bounded system remains stable. Additionally, an eigenvalue analysis for a particular test system is given by the stability condition (Section 3.3) and in the included ABC sensitivity analysis in Section 4.1.7. As all considered, nominal stencils fulfill the stability condition, they yield stable system behavior and are long-term stable.

This simulation example demonstrates that the proposed methodology is capable of producing well-performing and stable ABCs for the EBB. A comparison of the absorption quality RC (17) and the OE (19) performance objective for the optimization of ABCs will be given in the following section.

4.1.5. *Comparison of the accuracy objectives*

In this section the absorption properties of ABCs resulting from the optimization with respect to the RC accuracy objective (17) and the OE accuracy objective (19) will be compared by means of global relative space–time error (31). Because of the random nature of the genetic algorithm, each run of the MOO leads to a different solution set. To obtain a

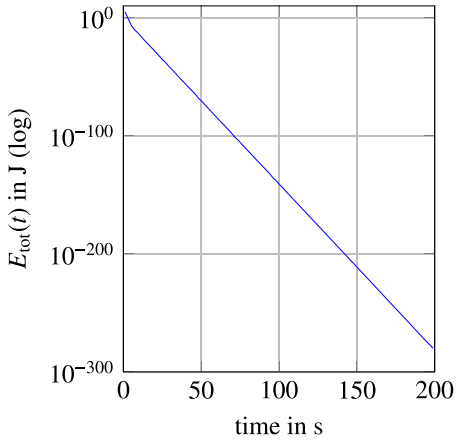

Fig. 9. Long-term energy decay of the optimized ABC for the EBB.

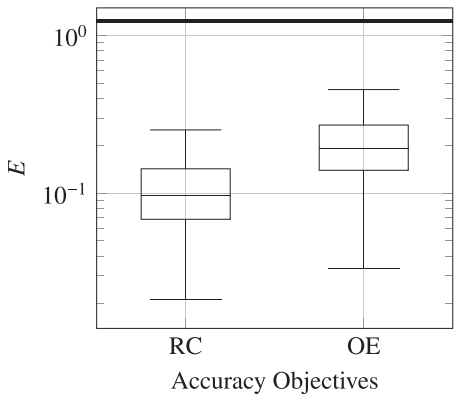

Fig. 10. Box plot comparison for ABCs optimized by the RC (17) (left) and OE (19) (right) accuracy objectives.

statistically relevant statement, 200 optimization runs are carried out. The best stable ABC of each run is applied to the EBB system.

The result is illustrated in Fig. 10 by means of box plots. The horizontal bold line at the top of the plot shows the global relative space–time error for the IC (29a) with clamping BCs at both boundaries ((27) at $x=0$ and $x=L$). These box plots show that utilizing the RC accuracy objective (17) during optimization yields on average better accuracy than using the OE accuracy objective (19) for $T_{\mathrm{SIM}} = 1.5$ s. The global relative space–time error E of the best optimized ABC is 1.72 percent for the RC-optimized and 2.87 percent for the OE-optimized ABCs (relative to the clamped-clamped setup). The average time of solving the MOO problem was slightly larger in the OE case (180.56 s vs. 153.31 s) on a modern office PC (Intel i7).

4.1.6. Frequency weighting

Frequency weighting of the OE accuracy objective (19) and its effect on the optimized ABCs are illustrated. For that purpose, the MOO problem (26) is solved twice using the stability objective (24) and the frequency-weighted OE accuracy objective (19) with the weightings

$$w_{\mathrm{high}}(\omega_x) = \begin{cases} 1 & \omega_x = 0, \ldots, \dfrac{7\pi}{10\Delta x} \\ 5000 & \omega_x = \dfrac{8\pi}{10\Delta x}, \ldots, \dfrac{\pi}{\Delta x} \end{cases} \tag{34a}$$

and

$$w_{\mathrm{low}}(\omega_x) = \begin{cases} 5000, & \omega_x = 0, \ldots, \dfrac{2\pi}{10\Delta x} \\ 1 & \omega_x = \dfrac{8\pi}{10\Delta x}, \ldots, \dfrac{\pi}{\Delta x} \end{cases} \tag{34b}$$

for high and low frequency weighting, respectively.

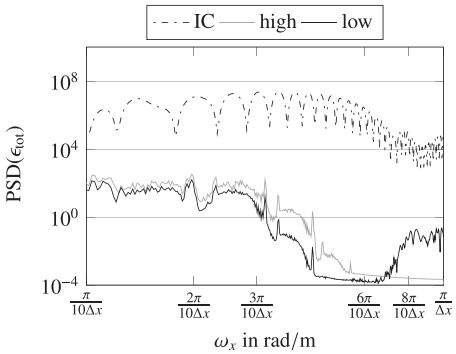

Fig. 11. Power spectral density of ϵ_{tot} (32a) for the IC and residual signal after absorption through the high- and low-frequency-weighted ABCs, respectively.

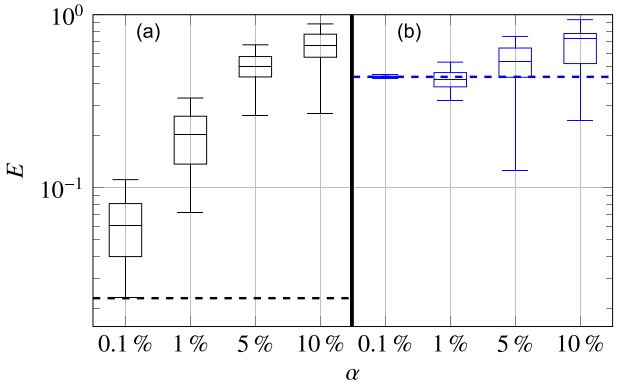

Fig. 12. Evaluation of ABC stencils with (a) $J_{\mathrm{perf}} = 8.6661 \times 10^{-2}$ and $J_{\mathrm{stab}} = 9.9990 \times 10^{-1}$ (black), b) $J_{\mathrm{perf}} = 1.1528 \times 10^{-1}$ and $1 - J_{\mathrm{stab}} = 5.3909 \times 10^{-2}$ (blue). (For interpretation of the references to color in this figure caption, the reader is referred to the web version of this paper.)

The results are displayed in Fig. 11 in terms of the power spectral density (PSD) of the total energy per unit length $\epsilon_{\text{tot}}(x,t)$ (32a) of the EBB (obtained by Welch's method [42]). The PSD of the IC $\epsilon_{\text{tot}}(x,0)$ and $\epsilon_{\text{tot}}(x,T)$ for the solution of the high- and low-frequency-weighted ABC cases ('high' and 'low') are shown.

As expected, the frequency weighting (34) used in the optimization influences the absorption properties of the ABCs such that the residual frequency content has smaller magnitudes at the low and high frequencies for the weightings w_{low} and w_{high}, respectively.

4.1.7. Sensitivity analysis of the ABC stencil

The sensitivity analysis of the ABC stencil (33) will be performed by considering stability (eigenvalue analysis) and accuracy (approximated global relative space–time error (31) and the setup from Section 4.1.1). For that each stencil value is relatively and randomly varied by $\alpha = \pm 0.1$ percent, $\alpha = \pm 1$ percent, $\alpha = \pm 5$ percent and $\alpha = \pm 10$ percent, where α is the perturbation level. Additionally, a second ABC stencil

$$ {}_0\boldsymbol{\mu}_0^{\mathrm{T}} = \left[2.3417 \times 10^{-1} \;\; 9.6807 \times 10^{-1} \;\; -1.8969 \times 10^{-1} \;\; -5.1449 \times 10^{-3}\right], \tag{35a} $$

$$ {}_1\boldsymbol{\mu}_0^{\mathrm{T}} = \left[6.3472 \times 10^{-2} \;\; 2.6482 \times 10^{-1} \;\; 9.0721 \times 10^{-1} \;\; -2.5508 \times 10^{-1}\right], \tag{35b} $$

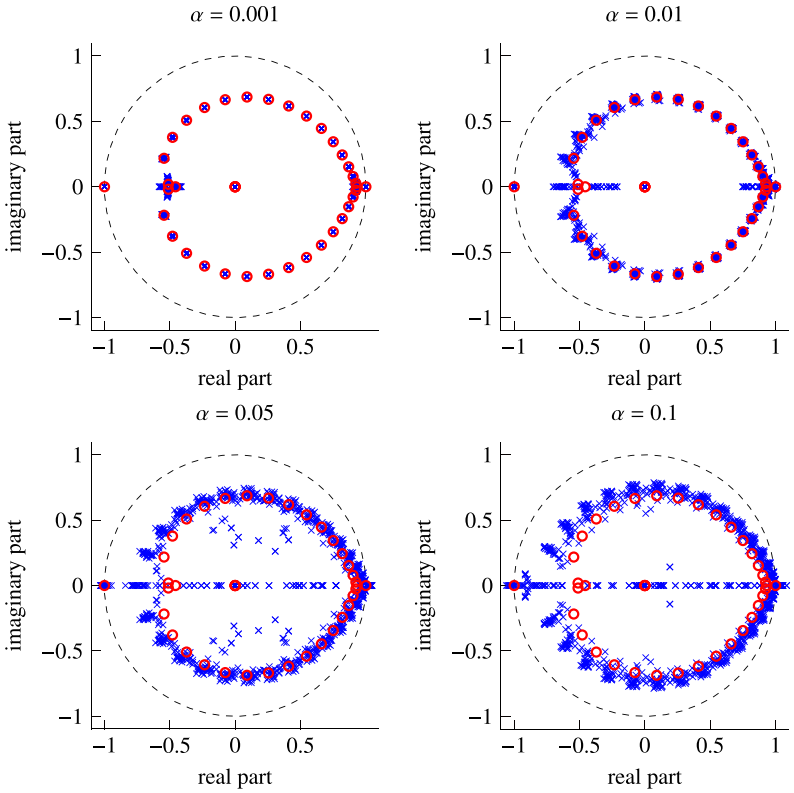

Fig. 13. Eigenvalue distribution of a small (N_x=20) test setup. The eigenvalues of the nominal stencil (○) and the perturbed stencils (×).

Table 1
Number of unstable ABCs for different perturbation levels α.

α	$\pm 0.1\%$	$\pm 1\%$	$\pm 5\%$	$\pm 10\%$
ABC (33)	24	35	28	29
ABC (35)	0	0	12	19

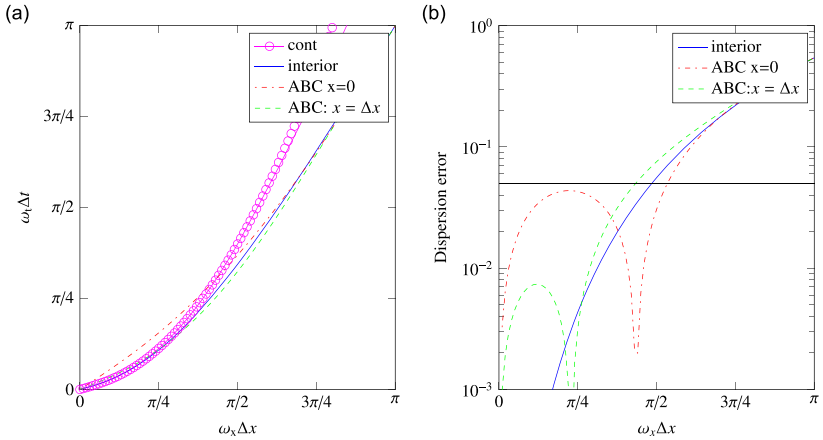

Fig. 14. (a) Dispersion relation of the continuous PDE, using interior stencil (blue solid) and using the ABC stencils (red dashed dotted at $x=0$ and green dashed at $x=\Delta x$). (b) Dispersion error in logarithmic scale. (For interpretation of the references to color in this figure caption, the reader is referred to the web version of this paper.)

with the stability margin $1-J_{\text{stab}} \approx 5.3909 \times 10^{-2}$ and accuracy objective value is $J_{\text{perf,RC}} \approx 1.1528 \times 10^{-1}$ is considered. This stencil has a larger stability margin and reflection coefficient and is thus excepted to be more robust concerning stability, but less accurate.

Starting with the accuracy for each perturbation level $N_{\text{perturb}} = 50$ perturbations were applied to the nominal stencils (33) and (35). Taking only stable perturbed stencils into account, the errors are displayed by means of box plots in Fig. 12. The results are displayed the in (a) and (b) for the ABCs stencils (33) and (35), respectively. The bold dashed horizontal lines in both figures mark the errors of the nominal ABC stencils. As expected, the stencil (33) is more accurate and perturbations lead to an increase of the error. The perturbation of stencil (35) leads for small perturbations (± 0.1 percent) to no significant change in accuracy. Increasing the perturbation level the median of the error increases, but some stable stencils outperform the nominal stencil (35).

For the sensitivity analysis of the stability the eigenvalue distribution for the same $N_{\text{perturb}} = 50$ stencils of the ABC stencil (33) is considered (see Fig. 13). In this figure the nominal eigenvalues are marked by circles ($\circ$) and those of the perturbed ABC stencil eigenvalue are marked by crosses ($\times$). The number of perturbed unstable ABCs is quantified in Table 1 for both ABC stencils. Summarizing the result, one can see that the increase of the perturbation level α leads to a stronger deviation of the eigenvalues and also to more eigenvalues outside the unit circle (see Fig. 13). However, because of the larger stability margin the ABC stencil (35) is more robust and all ABCs are stable for $\alpha = \pm 0.1$ percent and $\alpha = \pm 1$ percent. Then the number of unstable ABCs increases. In contrast, the number of unstable ABCs for (33) is typically above 50 percent.

The eigenvalue distribution of the ABC stencil (35) is omitted here, because it yields qualitatively similar results. The major differences have been summarized in Table 1.

4.1.8. Comparison of the continuous and discrete dispersion relation

In comparison to literature (e.g. Refs. [34,33,43]), where the dispersion relation (DR) is considered for a specific stencil (space and time discretization separately), here the DR of the entire PDE is considered as used in Ref. [6]. The dispersion relation of the continuous EBB (1) is calculated as

$$\rho A \omega_t^2 = \omega_x^4 EI + \omega_x^2 T. \tag{36}$$

The considered DRs are displayed in Fig. 14(a). One can clearly see that for the interior and ABCs at $x=0$ stencils are in good agreement with the continuous DR up to $\omega_x \Delta x \approx \pi/2$. For high frequencies all discrete DRs diverge similarly from the continuous DR. To compare the ABC and interior stencils quantitatively for a chosen error level E_{DISP} typically the quantity Points-per-Wavelength (PPW) is used (see Refs. [43,44]). Here, a reasonable choice is $E_{\text{DISP}} = 5$ percent (the bold horizontal line in Fig. 14(b)) leading to 4.13, 3.74 and 4.61 PPWs for the interior, the ABC at $x=0$ and the ABC at $x=\Delta x$, respectively. In Refs. [43] and [44], 7 and between 3.36 and 4.22 PPWs were achieved for high-order stencils approximating the first derivative $\partial/\partial x$ using $E_{\text{DISP}} = 0.3$ percent with $N_x^{\text{INT}} = 7$ and $E_{\text{DISP}} = 0.5$ percent with $N_x^{\text{INT}} = 9 \ldots 13$, respectively.

4.2. ABCs for the two-dimensional wave equation

The scalar two-dimensional wave equation is given by [38]

$$\frac{\partial^2 u}{\partial t^2} = c^2 \left(\frac{\partial^2 u}{\partial x^2} + \frac{\partial^2 u}{\partial y^2} \right), \tag{37}$$

with the vertical displacement $u(x,y,t)$, the wave propagation speed c and two spatial variables x and y. Here it is assumed that the PDE models small-amplitude waves in a membrane, and for the following numerical results the physical parameters were arbitrarily chosen as

$$\rho = 1\ \mathrm{kg/m^2}, \quad f = 100\ \mathrm{N/m}, \quad c = \sqrt{f/\rho} = 10\ \mathrm{m/s}, \tag{38}$$

where c is the wave propagation speed, f is the tensile line load (force per unit length) applied at the boundary of the membrane and ρ is the area density of the membrane material.

4.2.1. Implementation for the two-dimensional wave equation

Some modifications to the methods described in Sections 2 and 3 have to be made to investigate higher-dimensional problems. They will be sketched for the case of the two-dimensional wave equation (37).

The FD approximation of partial derivatives with respect to y is obtained analogously to (2) for an evenly spaced grid $y = [0, \Delta y, \ldots, N_y \Delta y]$ with $\Delta y \in \mathbb{R}^+$ and $N_y \in \mathbb{N}$. The generic stencil (3) now contains an additional sum in the y-direction

$$u_{k,m}^{n+1} = \sum_{i=0}^{N_t^{\mathrm{INT}}-1} \sum_{j=-(N_x^{\mathrm{INT}}-1)/2}^{(N_x^{\mathrm{INT}}-1)/2} \sum_{p=-(N_y^{\mathrm{INT}}-1)/2}^{(N_y^{\mathrm{INT}}-1)/2} a_{j,p}^{i} u_{k+j,m+p}^{n-i}, \tag{39}$$

and the boundary stencils are modified analogously. Using central differences on the two-dimensional wave equation (37) leads to $N_x^{\mathrm{INT}} = N_y^{\mathrm{INT}} = 3$ and $N_t^{\mathrm{INT}} = 2$. The harmonic wave solution is extended in the y-direction:

$$u_{k,m}^{n} = \left(\mathrm{e}^{\mathrm{i}\omega_x \Delta x}\right)^k \left(\mathrm{e}^{\mathrm{i}\omega_y \Delta y}\right)^m \left(\mathrm{e}^{\mathrm{i}\omega_t \Delta t}\right)^n = \kappa^k \zeta^m \tau^n. \tag{40}$$

Consequently, a second spatial wave number, ω_y, arises and the dispersion relation now connects ω_x, ω_y, and ω_t. Additionally, the angle $\varphi = f(\omega_x, \omega_y)$ describes the traveling direction of the wave and the dispersion relation can be parametrized in φ and ω_t.

The necessary adoptions to the objective functions will be demonstrated on the OE accuracy objective (19) and thestability objective (24). The output-error (18) for the two-dimensional wave equation is

$$e_{\mathrm{OE}}(\varphi, \omega_t) = \sum_{n=2}^{N_t^{\mathrm{OE}}} \sum_{k=1}^{N_x^{\mathrm{OE}}} \sum_{m=1}^{N_y^{\mathrm{OE}}} \left| u_{k,m}^{n} - \kappa^k \zeta^m \tau^n \right|^2, \tag{41}$$

and the objective function is obtained by aggregating this error function over the parameters φ and ω_t:

$$J_{\mathrm{perf,OE}} = \int_0^{\pi/2} \int_0^{\pi/\Delta x} w(\omega_t, \varphi) e_{\mathrm{OE}}(\omega_t, \varphi)\, \mathrm{d}\omega_t\, \mathrm{d}\varphi. \tag{42}$$

To evaluate thestability objective (24) the state-space representation of a test system needs to be constructed. The $N_x \times N_y$

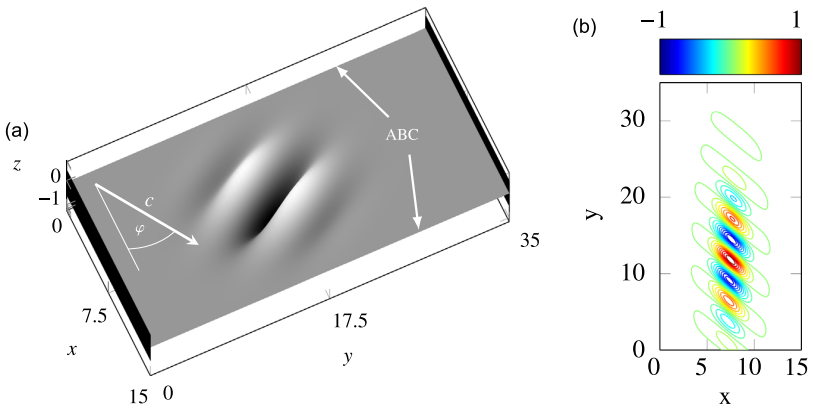

Fig. 15. (a) Problem setup for the two-dimensional wave example. ABCs are applied at $x = 0$ m and $x = 15$ m. At $y = 0$ m and $y = 35$ m Dirichlet BCs are applied. (b) Problem setup as contour plot.

solution values at each relevant time instant have to be organized as a stacked augmented state vector $\mathbf{v} \in \mathbb{R}^N$, with $N = (N_t^{\mathrm{up}} - 1)N_x N_y$, leading to a system matrix $\mathbf{A} \in \mathbb{R}^{N \times N}$.

4.2.2. Available absorbing boundary conditions

The optimized ABC stencils will be compared to already available ABCs from the literature. In 1977, Engquist and Majda [3] developed a method for obtaining absorbing boundary conditions of arbitrary order for the wave equation. However, the original Engquist–Majda boundary conditions are of practical use only in low-order because of their rapid increase in algebraic complexity for high-order formulations [11]. Here, the second-order Engquist–Majda (EM2) boundary conditions are applied:

$$\frac{\partial^2 u}{\partial x \partial t} - \frac{\partial^2 u}{\partial t^2} + \frac{1}{2}\frac{\partial^2 u}{\partial y^2} = 0, \tag{43}$$

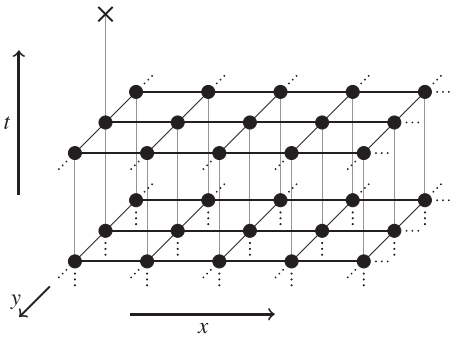

Fig. 16. Sketch of the (5,3,2) ABC stencil structure.

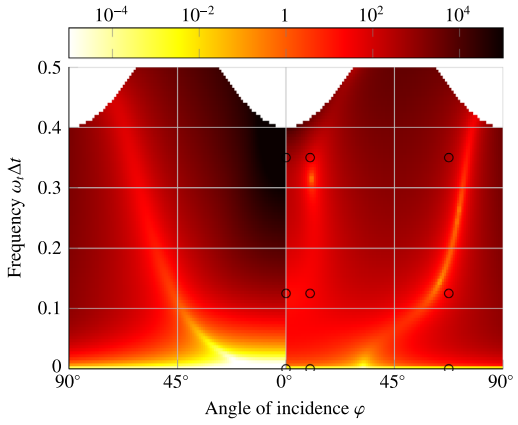

Fig. 17. Log-scaled output error $e_{\mathrm{OE}}(\varphi, \omega_t)$ (41) as a function of the angle of incidence φ and the frequency $\omega_t \Delta t$ for the second-order Engquist–Majda ABC (left) and an optimized (3,3,2) ABC stencil (right). The optimization grid used for obtaining the latter is marked by ○.

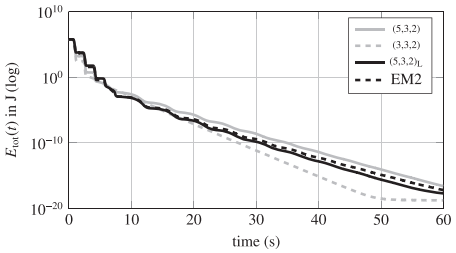

Fig. 18. Long-term energy decay of the optimized ABCs with high-frequency waves ($\omega_t \Delta t = 0.325$) for the two-dimensional wave equation.

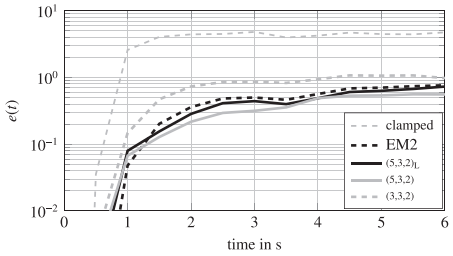

Fig. 19. Total error $e(t)$ for different ABCs with low-frequency waves ($\omega_t \Delta t = 0.035$), arriving with an angle of incidence of $\varphi = 45°$.

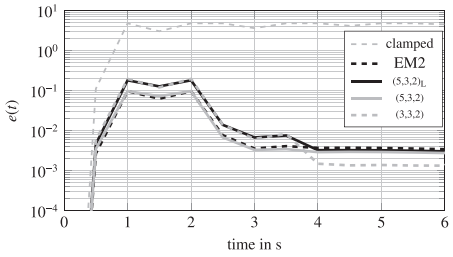

Fig. 20. Total error $e(t)$ for different ABCs with mid-frequency waves ($\omega_t \Delta t = 0.15$), arriving with an angle of incidence of $\varphi = 5°$.

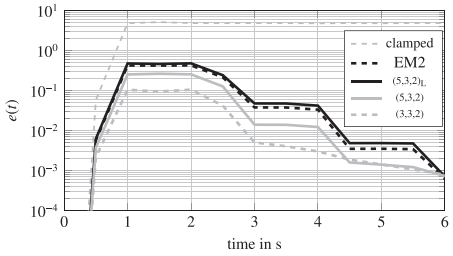

Fig. 21. Total error $e(t)$ for different ABCs with high-frequency waves ($\omega_t \Delta t = 0.325$), arriving with an angle of incidence of $\varphi = 10°$.

where x and y denote the directions in normal and tangential direction on the boundary, respectively. In this work, all derivatives in (43) were discretized using second-order-accurate finite difference schemes.

Another important ABC for wave problems is the Higdon ABC [30]:

$$\prod_{j=1}^{J} \left(\frac{\partial u(x,y,t)}{\partial t} + C_j \frac{\partial u(x,y,t)}{\partial x} \right) = 0, \tag{44}$$

with constants C_j and J denoting the order of the ABC. Higdon proved that every ABC that is based on a symmetric rational approximation of the dispersion relation (for outgoing waves) is either equivalent to (44) or not optimal [30]. Moreover, for $J=2$ and certain values of C_j, the Higdon ABC corresponds to the EM2 ABC (43). Theoretically, the same problems with higher derivatives as for the Engquist–Majda ABCs arises when implementing (44). However, several different methods exist for efficiently applying the Higdon ABCs; see [12] for a corresponding review.

4.2.3. Problem setup

Fig. 15(a) exemplarily shows the simulation setup with a very-low-frequency wave packet that is started with an initial velocity of c in the direction associated with angle φ. In Fig. 15(b) the simulation setup is displayed as a contour plot (compare Appendix B). The initial condition for all simulation runs was chosen as

$$u_{k,m}^0 = \mathrm{Re}\left(\mathrm{e}^{\mathrm{i}\omega_x \Delta x k} \mathrm{e}^{\mathrm{i}\omega_y \Delta y m} \right) \mathrm{e}^{-0.4(k\Delta x - x_c)^2} \mathrm{e}^{-0.015(m\Delta y - y_c)^2}, \tag{45}$$

with appropriately selected centers x_c and y_c. The domain size was chosen as $l_x = 15$ m, $l_y = 35$ m, and the ABCs are applied at $x = 0$ m and $x = 15$ m while the remaining two boundaries are fixed (Dirichlet BCs). The step sizes were chosen as $\Delta x = \Delta y = 0.05$ m and $\Delta t = 0.001$ s.

4.2.4. Optimization setup

Throughout the following examples the OE accuracy objective (42) is utilized to quantify the absorption properties. The stability condition (24) has been evaluated for a test system of size $N_x = N_y = 7$, which leads to a system matrix $\mathbf{A} \in \mathbb{R}^{98\times 98}$, see (22). However, by eliminating zero-states that result from Dirichlet BCs the system matrix is reduced to $\mathbf{A} \in \mathbb{R}^{60\times 60}$.

Especially for larger ABC stencil sizes (due to the large number of decision variables), it was observed that convergence of the MOO genetic algorithm to the actual Pareto front may be difficult to achieve. Throughout this example, only single-objective optimization problems were formulated and solved by a *pattern-search* method [27], where the accuracy objective was multiplied with a large penalty term when the stability objective (24) indicated instability, which corresponds to using a stability constraint (24).

4.2.5. Investigated stencil configurations

The structure of the studied ABC realizations is denoted here by the triplet $(N_x^{\mathrm{ABC}}, N_y^{\mathrm{ABC}}, N_t^{\mathrm{ABC}})$, where N_x^{ABC} and N_y^{ABC} are the spatial widths in normal and tangential direction, respectively (for the ABC along the $x = 0$ m edge), and N_t^{ABC} is the number of time instants that are needed for the computation of the next boundary grid point. Fig. 16 shows the structure of a (5,3,2) stencil where the grid points marked by dots ($\bullet$) are needed for the computation of the future boundary grid point marked by a cross ($\times$).

The following ABCs are further investigated: an EM2 ABC [3] and proposed ABCs of structures (3,3,2), (5,3,2), and $(5,3,2)_{\mathrm{L}}$, where the latter is only optimized for low frequencies. Their numerical values are summarized in Appendix A.

For discretizing the EM2 ABC second-order accuracy approximations were used, yielding a (4,3,2) stencil. The (3,3,2) ABC is optimized over a grid $\varphi \times \omega_t \Delta t = [0^\circ, 10^\circ, 67.5^\circ] \times [0\ \mathrm{rad}, 0.125\ \mathrm{rad}, 0.35\ \mathrm{rad}]$ with a focus on higher frequencies. The (5,3,2) ABC is optimized to obtain an overall well-performing ABC, independent of the angle φ and frequency ω_t of the incoming wave.

4.2.6. ABC comparison by output-error accuracy

The ABC with the structure (3,3,2) is compared to the second-order Engquist–Majda (EM2) ABC [3]. In Fig. 17, the values of the output error function (41) are plotted for a fine grid over φ and $\omega_t \Delta t$. Dark regions indicate a large error, whereas the bright regions correspond to small errors. As can be seen in Fig. 17, the EM2 ABC performs very well in the low-frequency range, while the error made at high-frequency waves arriving in normal direction is very large. However, the EM2 needs a larger stencil (4,3,2) than the optimized (3,3,2) ABC. The optimized (3,3,2) ABC already leads to good overall performance in this configuration. It is noted that for plotting the minimum of the output error function was clipped to 5×10^{-4} to obtain a better scaling in the very-low-frequency range.

4.2.7. True error comparison and long-term stability

In the following, all ABC stencils introduced in Section 4.2.5 are compared. For the quantification of the absorption properties the time-dependent error in analogy to (30) is defined for the two-dimensional case

$$e(t) = \frac{\|\mathbf{u}(t) - \mathbf{u}_{\mathrm{ref}}(t)\|_{[0,l_y][0,l_x]}}{\sqrt{A}} \tag{46}$$

where $A = l_x l_y$ is the computational area and $\mathbf{u}_{\mathrm{ref}}$ is the reference solution computed on a much larger domain ($-40\ \mathrm{m} \le x \le +40\ \mathrm{m}$), see Fig. 6(b). The verification of the long-term stability is carried out by evaluating the total energy remaining inside the computational domain $x \in [0, l_x]$, $y \in [0, l_y]$ [23]:

$$E_{\mathrm{tot}}(t) = E_{\mathrm{kin}}(t) + E_{\mathrm{pot}}(t), \tag{47a}$$

$$E_{\mathrm{kin}}(t) = \frac{\rho}{2} \int_0^{l_x} \int_0^{l_y} \left(\frac{\partial u}{\partial t}\right)^2 \mathrm{d}y\, \mathrm{d}x, \tag{47b}$$

$$E_{\mathrm{pot}}(t) = \frac{f}{2} \int_0^{l_x} \int_0^{l_y} \left[\left(\frac{\partial u}{\partial x}\right)^2 + \left(\frac{\partial u}{\partial y}\right)^2\right] \mathrm{d}y\, \mathrm{d}x. \tag{47c}$$

Long-term simulations of the test system with the obtained ABCs in place showed that they indeed did not render the finite-difference scheme unstable (see Fig. 18).

The results by means of time-dependent error $e(t)$ are plotted in the Figs. 19–21 for different angles and frequencies of the initial waves. Similar to the EBB example the time-dependent error $e(t)$ stays zero until the wave packets reach the boundary and stays then approximately constant. The time-domain plots are displayed in Figs. B1–B3.

These results confirm that the accuracy of the optimized ABCs compares favorably over a wide frequency range with the EM2 ABC, whose stencil is essentially of the same size as those used for the optimized ABCs. Additionally, the flexibility and tunability of the optimization-based approach provides significant design advantages in practice.

5. Conclusion and discussion

A generic method to produce well-performing and stable absorbing boundary conditions (ABCs) for finite-difference approximations of partial differential equations with wave propagation effects has been proposed. The ABC stencil coefficients are utilized as decision variables in an optimization problem in which both absorption accuracy and stability are considered. This approach requires only modest analytical treatment of the underlying partial differential equations and provides great flexibility to tune specific properties of the resulting ABCs.

The versatility of the proposed method is demonstrated at two applications — the Euler–Bernoulli bending beam under axial load (for which no ABCs are yet known) and the two-dimensional wave equation. The proposed accuracy objectives are compared and discussed for the Euler–Bernoulli beam example, well-performing ABCs are obtained, and the effect of a frequency-weighted accuracy formulation is investigated. The ABC optimization method is also applied for the well-known two-dimensional scalar wave problem, and it produces highly absorbing BCs, equivalent in accuracy to those derived by Engquist and Majda [3] analytically. Moreover, the behavior of the optimized ABCs can be directly tuned with respect to frequency and angle-of-incidence which provides a large degree of flexibility.

The numeric approach to obtain high-accuracy ABCs is a powerful complementary approach to the analytic derivation of ABCs. The optimization method can simply be transferred to different types of problems and it is straightforward to tune the ABC's frequency or directional behavior. As a result, well-performing ABCs could become available for a wide class of distributed-parameter problems addressed by the finite-difference method.

In future research work, the presented method to obtain ABCs will be tested on complex boundary geometries (e.g. corners) and on other types of equations (such as the wave equation in moving coordinates). The method could also be extended to linearized Euler equation which is governed by a set of three coupled PDEs leading to three coupled dispersion relations. This requires a careful investigation of this PDE and its dispersion relation, to verify if all necessary assumptions for the proposed method are fulfilled.

Acknowledgment

This work has partially been financed by the Austrian Research Promotion Agency (FFG) under Grant nos. 836449 and 841331.

Appendix A. ABC stencil values two-dimensional wave equation

The ABC stencil coefficient values ${}_{(x,y)}\boldsymbol{\mu}_t^{\mathrm{T}}$ are defined in analogy to the one-dimensional stencil (see Section 2). Numbers are given with power-10 exponential notation e.g. $1.2\times10^{-1}=1.2\mathrm{e}-1$.
For the (3,3,2) stencil one obtains

$$
\begin{aligned}
{}_{(x,0)}\boldsymbol{\mu}_0^{\mathrm{T}} &= \left[1.80717\times10^{-1}\ \ 1.09193e{+}00\ \ 1.82365\times10^{-1}\right]\\
{}_{(x,1)}\boldsymbol{\mu}_0^{\mathrm{T}} &= {}_{(x,-1)}\boldsymbol{\mu}_0^{\mathrm{T}} = \left[-1.81047\times10^{-1}\ \ -6.89779\times10^{-2}\ \ 3.37948\times10^{-1}\right]\\
{}_{(x,0)}\boldsymbol{\mu}_1^{\mathrm{T}} &= \left[-6.99544\times10^{-2}\ \ -4.32682\times10^{-1}\ \ -1.72127\times10^{-1}\right]\\
{}_{(x,1)}\boldsymbol{\mu}_1^{\mathrm{T}} &= {}_{(x,-1)}\boldsymbol{\mu}_1^{\mathrm{T}} = \left[3.60531\times10^{-1}\ \ -6.56820\times10^{-2}\ \ -1.49357\times10^{-1}\right]
\end{aligned}
$$

with $x=0,\ldots,2$. The (5,3,2) and $(5,3,2)_{\mathrm{L}}$ are defined as

$$
\begin{aligned}
{}_{(x,0)}\boldsymbol{\mu}_0^{\mathrm{T}} &= \left[1.70526\times10^{-2}\ \ 1.71110e{+}00\ \ 7.25865\times10^{-3}\ \ 3.20594\times10^{-1}\ \ 2.62183\times10^{-3}\right]\\
{}_{(x,1)}\boldsymbol{\mu}_0^{\mathrm{T}} &= {}_{(x,-1)}\boldsymbol{\mu}_0^{\mathrm{T}} = \left[-8.52673\times10^{-2}\ \ -3.38745\times10^{-4}\ \ -1.69488\times10^{-3}\ \ -3.23486\times10^{-4}\ \ 1.64642\times10^{-3}\right]\\
{}_{(x,0)}\boldsymbol{\mu}_1^{\mathrm{T}} &= \left[-3.38745\times10^{-4}\ \ -7.39300\times10^{-1}\ \ -3.38745\times10^{-4}\ \ -3.47995\times10^{-1}\ \ 1.79749\times10^{-3}\right]\\
{}_{(x,1)}\boldsymbol{\mu}_1^{\mathrm{T}} &= {}_{(x,-1)}\boldsymbol{\mu}_1^{\mathrm{T}} = \left[8.78247\times10^{-2}\ \ -3.38745\times10^{-4}\ \ -1.69373\times10^{-4}\ \ -3.38745\times10^{-4}\ \ -1.69373\times10^{-4}\right]
\end{aligned}
$$

and

$$
\begin{aligned}
{}_{(x,0)}\boldsymbol{\mu}_0^{\mathrm{T}} &= \left[1.74426\times10^{-2}\ \ 1.71133e{+}00\ \ 7.00779\times10^{-3}\ \ 3.18287\times10^{-1}\ \ -1.68786\times10^{-3}\right]\\
{}_{(x,1)}\boldsymbol{\mu}_0^{\mathrm{T}} &= {}_{(x,-1)}\boldsymbol{\mu}_0^{\mathrm{T}} = \left[-7.35061\times10^{-2}\ \ 5.12695\times10^{-5}\ \ -1.71350\times10^{-3}\ \ 5.12695\times10^{-5}\ \ 2.56348\times10^{-5}\right]\\
{}_{(x,0)}\boldsymbol{\mu}_1^{\mathrm{T}} &= \left[5.12695\times10^{-5}\ \ -7.39105\times10^{-1}\ \ 5.12695\times10^{-5}\ \ -3.47800\times10^{-1}\ \ 1.07361\times10^{-3}\right]
\end{aligned}
$$

$$_{(x,1)}\boldsymbol{\mu}_1^{\mathrm{T}} = {}_{(x,-1)}\boldsymbol{\mu}_1^{\mathrm{T}} = \left[8.41440 \times 10^{-2} \;\; 5.12695 \times 10^{-5} \;\; 2.56348 \times 10^{-5} \;\; 5.12695 \times 10^{-5} \;\; 2.56348 \times 10^{-5}\right]$$

with $x = 0, \ldots, 4$, respectively.

Appendix B. Time domain solutions of the two-dimensional wave equation

The following Figs. B1–B3 show the time domain results for the $(5,3,2)_{\mathrm{L}}$, (5,3,2), (3,3,2) stencils for low, mid and high frequency ICs, respectively. The ABC results (middle columns) are compared with the reference solution (left columns) and EM2 result (right columns) at different time instances.

Fig. B1 shows that both ABCs perform well for low frequencies. The third row of this figure shows that there are small differences in the middle ($5 < x < 10, 10 < y < 20$) and the upper-right ($10 < x < 15, 20 < y < 30$) part of the computational domain. The mid frequency solution in Fig. B2 shows again nearly perfect results at $t = 0.75$ s for the ABCs. At $t = 1$ s the

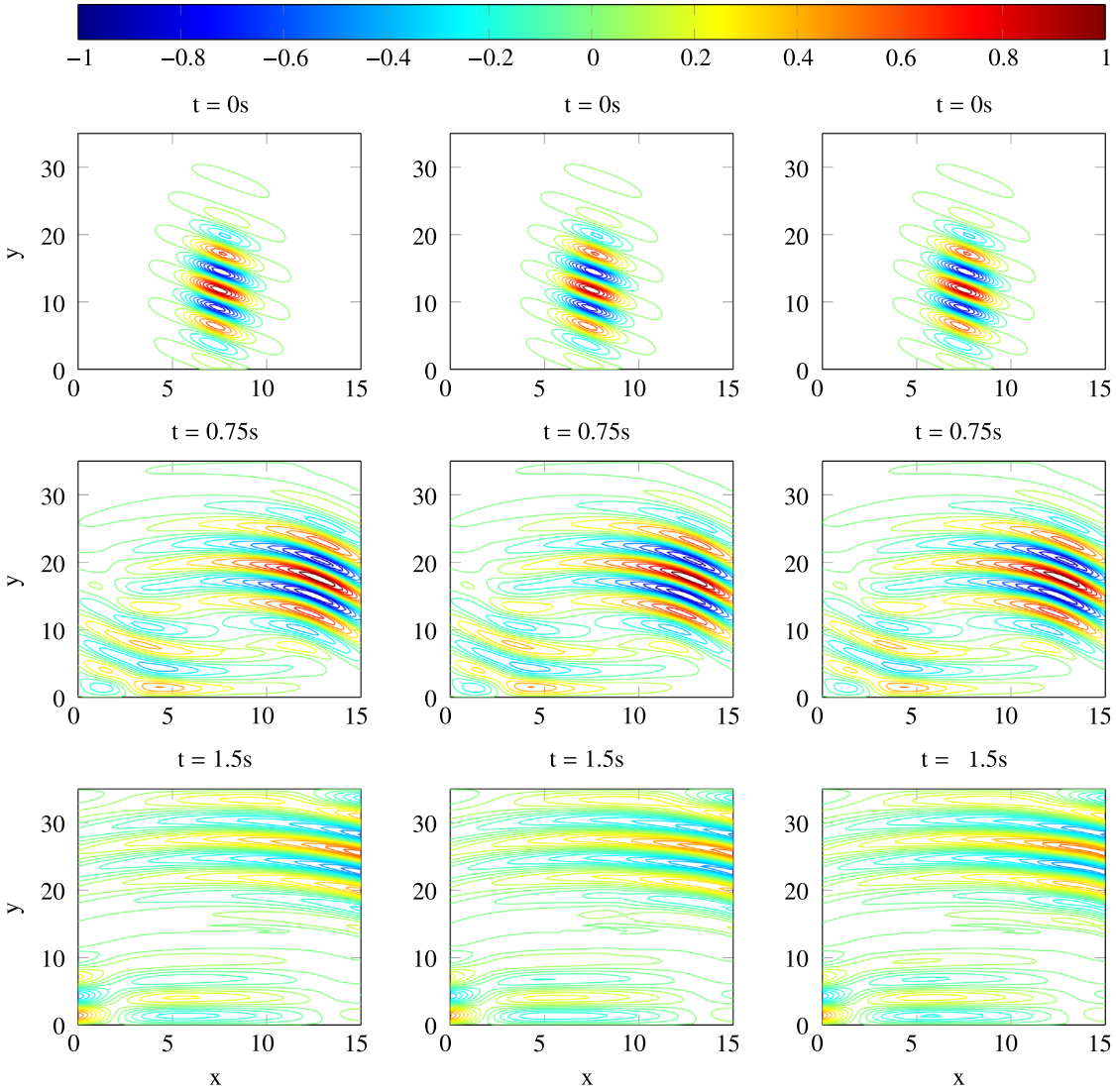

Fig. B1. Time domain solution for the low frequency IC and the $(5,3,2)_{\mathrm{L}}$ stencil: reference solution (left), ABC solution (mid) and EM2 (right).

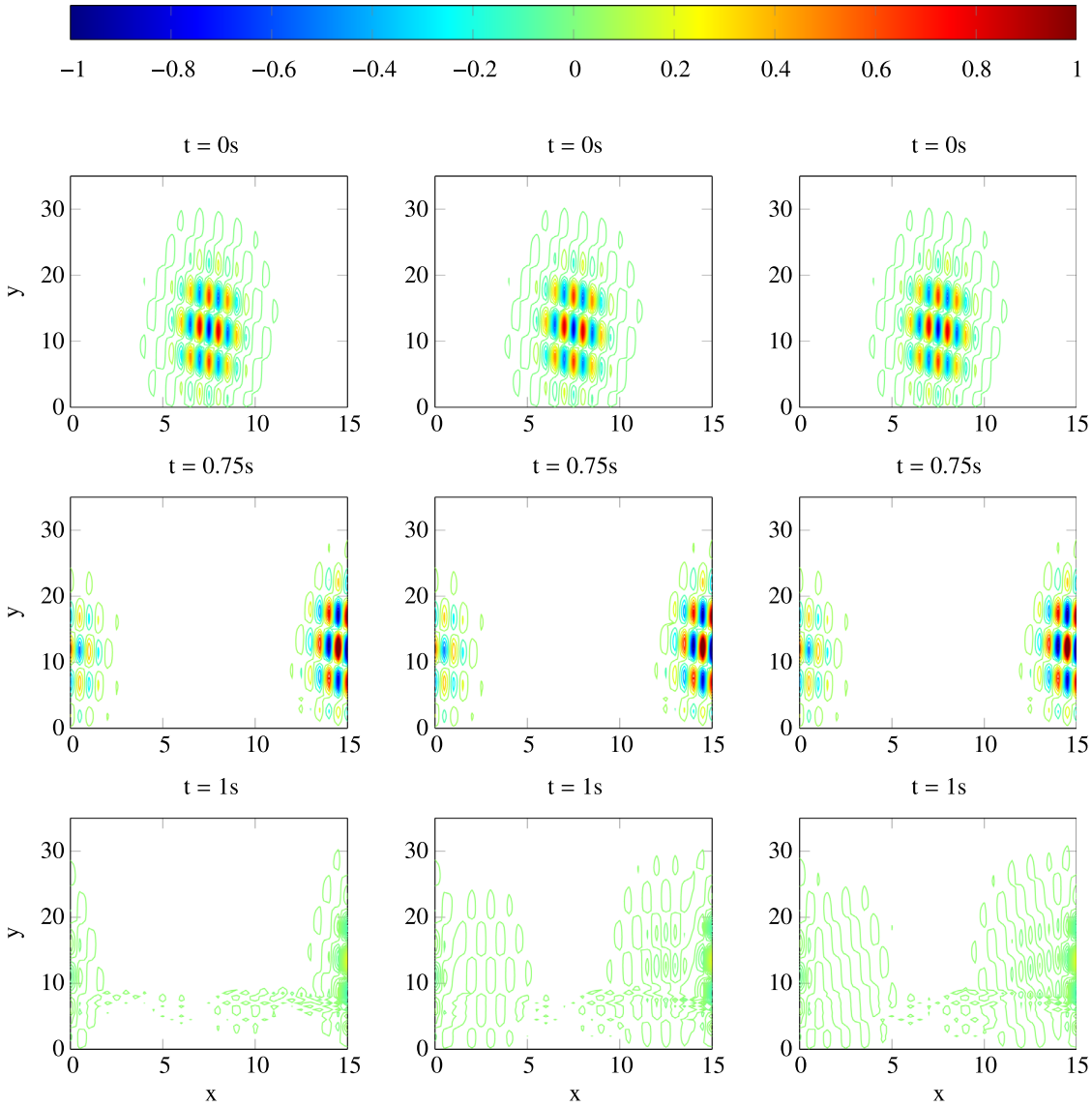

Fig. B2. Time domain solution for the mid frequency IC and the (5,3,2) stencil: reference solution (left), ABC solution (mid) and EM2 (right).

(5,3,2)-stencil reflects more than in the low frequency case, because the ABC is not optimized for mid frequencies. In this case the (5,3,2) and EM2 solution perform equally well. In Fig. B3 one can clearly see that the (3,3,2)-stencil absorbs the greater part of incoming waves and achieves a better result than EM2.

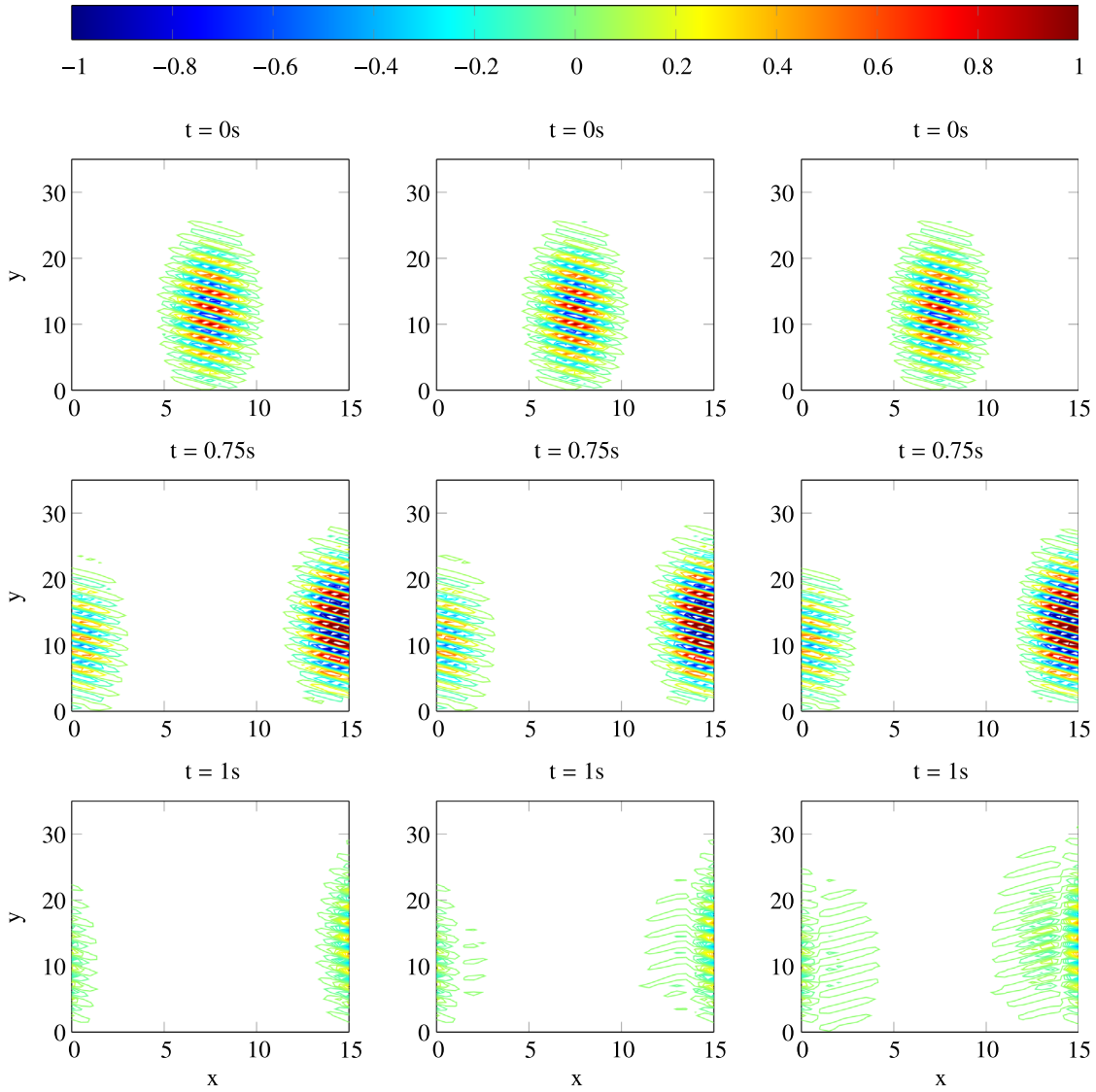

Fig. B3. Time domain solution for the high frequency IC and the (3,3,2) stencil: reference solution (left), ABC solution (mid) and EM2 (right).

Appendix C. Supplementary data

Supplementary data associated with this paper can be found in the online version at http://dx.doi.org/10.1016/j.jsv.2015.12.006.

References

[1] A. Sommerfeld, *Partial Differential Equations in Physics, Pure and Applied Mathematics*, Elsevier Science, New York, 1949.
[2] J. Strikwerda, *Finite Difference Schemes and Partial Differential Equations*, Wadsworth Publ. Co., Belmont, CA, USA, 1989.
[3] B. Engquist, A. Majda, Absorbing boundary conditions for numerical simulation of waves, *Proceedings of the National Academy of Sciences* 74 (5) (1977) 1765–1766.
[4] A. Bayliss, E. Turkel, Radiation boundary conditions for wave-like equations, *Communications on Pure and Applied Mathematics* 33 (6) (1980) 707–725.
[5] I. Shevchenko, M. Kaltenbacher, B. Wohlmuth, Absorbing boundary conditions for a wave equation with a temperature-dependent speed of sound, *Journal of Computational Acoustics* 21 (2) .

[6] R. Higdon, Absorbing boundary conditions for difference approximations to the multi-dimensional wave equation, *Mathematics of Computation* 47 (176) (1986) 437–459.
[7] R. Higdon, Radiation boundary conditions for elastic wave propagation, *SIAM Journal of Numerical Analysis* 27 (4) (1990) 831–869.
[8] R. Higdon, Radiation boundary conditions for dispersive waves, *SIAM Journal of Numerical Analysis* 31 (1) (1994) 64–100.
[9] T. Hagstrom, A. Mar-Or, D. Givoli, High-order local absorbing conditions for the wave equation: *extensions and improvements*, *Journal of Computational Physics* 227 (6) (2008) 3322–3357.
[10] D. Givoli, B. Neta, High-order non-reflecting boundary scheme for time-dependent waves, *Journal of Computational Physics* 186 (1) (2003) 24–46.
[11] D. Givoli, B. Neta, High-order non-reflecting boundary conditions for dispersive waves, *Wave Motion* 37 (3) (2003) 257–271.
[12] D. Givoli, High-order local non-reflecting boundary conditions: *a review*, *Wave Motion* 39 (4) (2004) 319–326.
[13] M. Israeli, S.A. Orszag, Approximation of radiation boundary conditions, *Journal of Computational Physics* 41 (1) (1981) 115–135.
[14] A. Mimani, Z. Prime, C. Doolan, P. Medwell, A sponge-layer damping technique for aeroacoustic time-reversal, *Journal of Sound and Vibration* 342 (2015) 124–151.
[15] J.-P. Bérenger, A perfectly matched layer for the absorption of electromagnetic waves, *Journal of Computational Physics* 114 (2) (1994) 185–200.
[16] W.C. Chew, W.H. Weedon, A 3d perfectly matched medium from modified maxwell's equations with stretched coordinates, *Microwave and Optical Technology Letters* 7 (13) (1994) 599–604.
[17] P. Chobeau, D. Ecoti Aïe, G. Dutilleux, J. Picaut, An absorbing matched layer implementation for the transmission line matrix method, *Journal of Sound and Vibration* 337 (2015) 233–243.
[18] T. Hagstrom, D. Givoli, D. Rabinovich, J. Bielak, The double absorbing boundary method, *Journal of Computational Physics* 259 (2014) 220–241.
[19] J.-P. Bérenger, A historical review of the absorbing boundary conditions for electromagnetics, *Forum for Electromagnetic Research Methods and Application Technologies* 9 (6) (2015).
[20] G. Montseny, J. Audounet, D. Matignon, Fractional integrodifferential boundary control of the Euler Bernoulli beam, *Conference on Decision and Control*, 1997, pp. 4973–4978.
[21] S.-Y. Lee, C. Mote, Wave characteristics and vibration control of translating beams by optimal boundary damping, *Journal of Vibration and Acoustics* 121 (1) (1999) 18–25.
[22] S.-Y. Lee, C. Mote, Vibration control of an axially moving string by boundary control, *Journal of Dynamic Systems, Measurement, and Control* 118 (1) (1996) 66–74.
[23] P. Hagedorn, A. DasGupta, *Vibrations and Waves in Continuous Mechanical Systems*, Wiley, Chichester, UK, 2007.
[24] L. Evans, *Partial Differential Equations, Graduate Studies in Mathematics*, American Mathematical Society, Providence, RI, 2010.
[25] R. LeVeque, *Finite Difference Methods for Ordinary and Partial Differential Equations: Steady-State and Time-Dependent Problems* (Classics in Applied Mathematics Classics in Applied Mathemat), Society for Industrial and Applied Mathematics, Philadelphia, PA, USA, 2007.
[26] D.W. Marquardt, An algorithm for least-squares estimation of nonlinear parameters, *Journal of the Society for Industrial & Applied Mathematics* 11 (2) (1963) 431–441.
[27] C. Audet, J.E. Dennis Jr., Analysis of generalized pattern searches, *SIAM Journal on Optimization* 13 (3) (2002) 889–903.
[28] K. Deb, D. Kalyanmoy, *Multi-Objective Optimization Using Evolutionary Algorithms*, John Wiley & Sons, Inc., New York, NY, USA, 2001.
[29] K. Deb, A. Pratap, S. Agarwal, T. Meyarivan, A fast and elitist multiobjective genetic algorithm: *NSGA-II*, *IEEE Transactions on Evolutionary Computation* 6 (2) (2002) 182–197.
[30] R. Higdon, Numerical absorbing boundary conditions for the wave equation, *Mathematics of Computation* 49 (179) (1987) 65–90.
[31] L. Ljung (Ed.), *System Identification, Theory for the User*, 2nd ed. Prentice Hall PTR, Upper Saddle River, NJ, USA, 1999.
[32] S.K. Lele, Compact finite difference schemes with spectral-like resolution, *Journal of Computational Physics* 103 (1) (1992) 16–42.
[33] R.K. Shukla, M. Tatineni, X. Zhong, Very high-order compact finite difference schemes on non-uniform grids for incompressible Navier–Stokes equations, *Journal of Computational Physics* 224 (2) (2007) 1064–1094.
[34] J.W. Kim, Optimised boundary compact finite difference schemes for computational aeroacoustics, *Journal of Computational Physics* 225 (1) (2007) 995–1019.
[35] D. Rabinovich, D. Givoli, J. Bielak, T. Hagstrom, A finite element scheme with a high order absorbing boundary condition for elastodynamics, *Computer Methods in Applied Mechanics and Engineering* 200 (23–24) (2011) 2048–2066.
[36] D. Baffet, J. Bielak, D. Givoli, T. Hagstrom, D. Rabinovich, Long-time stable high-order absorbing boundary conditions for elastodynamics, *Computer Methods in Applied Mechanics and Engineering* 241 (2012) 20–37.
[37] K. Ogata, *Discrete-time Control Systems*, vol. 2, Prentice Hall, Englewood Cliffs, NJ, 1995.
[38] S. Rao, *Vibration of Continuous Systems*, Wiley, Hoboken, NJ, 2007.
[39] R. Courant, K. Friedrichs, H. Lewy, On the partial difference equations of mathematical physics, *IBM Journal of Research and Development* 11 (2) (1967) 215–234.
[40] R. Marler, J. Arora, Survey of multi-objective optimization methods for engineering, *Structural and Multidisciplinary Optimization* 26 (6) (2004) 369–395.
[41] M. Arnold, B. Simeon, Pantograph and catenary dynamics: *a benchmark problem and its numerical solution*, *Applied Numerical Mathematics* 34 (4) (2000) 345–362.
[42] P.D. Welch, The use of fast Fourier transform for the estimation of power spectra: *a method based on time averaging over short, modified periodograms*, *IEEE Transactions on Audio and Electroacoustics* 15 (2) (1967) 70–73.
[43] C.K. Tam, Computational aeroacoustics-issues and methods, *AIAA Journal* 33 (10) (1995) 1788–1796.
[44] C. Bogey, C. Bailly, A family of low dispersive and low dissipative explicit schemes for flow and noise computations, *Journal of Computational Physics* 194 (1) (2004) 194–214.

Publication C

Guilherme Aschauer, Emir Talic, Alexander Schirrer, Martin Kozek and Stefan Jakubek.
Catenary Emulation for Hardware-in-the-Loop Pantograph Testing with a Model Predictive Energy-Conserving Control Algorithm
Mechatronics, accepted with minor revision

Author's contribution

Problem analysis, development and programming of algorithms, consideration of implementation aspects, performing simulation studies, and structuring, writing and editing of the manuscript was done by the applicant.

Catenary Emulation for Hardware-in-the-Loop Pantograph Testing with a Model Predictive Energy-Conserving Control Algorithm

A. Schirrer[a,*], G. Aschauer[a], E. Talic[a], M. Kozek[a], S. Jakubek[a]

[a]*Inst. of Mechanics & Mechatronics, Technische Universität Wien, Getreidemarkt 9, 1060 Vienna, Austria*

Abstract

Pantograph current collectors, especially for high-speed trains, need to ensure safe contact with the catenary under stringent requirements on the dynamic contact force. A novel, high-dynamic pantograph test rig with accurate virtual catenary emulation is presented that allows for efficient, realistic, and reproducible testing. The complex dynamics of the pantograph/catenary interaction is modeled by a real-time-capable distributed-parameter description in moving coordinates. The proposed test rig controller incorporates model-predictive impedance control to match the desired catenary dynamics. Additionally, it keeps the exchange of the conserved quantities energy and momentum between the real pantograph and the virtual catenary consistent to increase physical trustworthiness of the results, even in high-dynamic test scenarios. The proposed methods are experimentally validated on the full-scale pantograph test rig.

Keywords: hardware-in-the-loop, impedance control, conserved-quantities, catenary modeling, pantograph testing

1. Introduction

In recent years, railway current collectors (pantographs) have become a limiting factor when pushing the velocity limits of high-speed trains. They need to ensure a steady contact with the catenary's contact wire to maintain the train's energy supply. Loss of contact must be avoided to prevent arcing (and thus heavy wear). As a result, modern pantographs have to fulfill high requirements: small contact force variations, highly reliable operation, and long life cycles. The main problem in the development process of high-performance, high-speed pantographs is the complexity of the interaction dynamics with the catenary. Therefore, physical trustworthiness of simulations is limited, requiring laborious actual track tests. One way to reduce the need for measurement runs that also allows for reproducible testing is to deploy the pantograph on a test bed and examine its behavior in advance. This concept is called hardware-in-the-loop (HiL) testing whereby the real, full-size pantograph is the unit under test (UUT) that is being put into interaction with a virtual catenary model.The goal thereby is to emulate a real-world train ride already in the laboratory by applying realistic, dynamically generated load patterns that emerge from the coupled interaction of the virtual catenary and the UUT.

Simplified pantograph HiL testing can be realized by exciting the pantograph with a predefined motion trajectory, such as the static pre-sag of the catenary's contact wire [1]. However, the pantograph/catenary interaction is crucial to obtain realistic test results. To consider the catenary's dynamic response, it has to be either modeled in a simplified way by oscillators (ordinary differential equations, ODEs) or by high-fidelity models (based on partial differential equations, PDEs) [2, 3].

Controlling the test rig so that it dynamically responds to the UUT in the same way as the catenary model is accomplished by impedance control [4, 5], where a dynamic behavior rather than a predefined reference trajectory is tracked. Nowadays, impedance control is not only applied in robotics for handling tasks but also used, for example, in engine testbed control [6] or battery emulation [7]. The closely related field of bilateral teleoperation is reviewed in Refs. [8, 9].

Accurate, realistic emulation of the pantograph/catenary interaction needs a real-time-capable model in sufficient details, and so high-fidelity PDE modeling is imperative for accurate dynamics, especially at high speeds. A typical catenary configuration consists of a carrier and a contact wire which are

*Corresponding author. Tel.: +43 158801 325521
Email address: alexander.schirrer@tuwien.ac.at (A. Schirrer)

coupled via so-called droppers. The carrier wire is additionally attached to inertia-fixed masts. Each wire can be modeled as an Euler-Bernoulli beam under axial tension, and due to the droppers the resulting equations that need to be solved are two coupled PDEs with constraints [10]. Both wires are weakly damped, and typically a large computational domain is needed in order to capture wave propagation phenomena correctly without distortion by spurious reflections at the boundaries.

Since the early 2000s HiL pantograph testing has been described, e.g. in Ref. [3]. There, the pantograph has been excited with two hydraulic actuators from the top and the bottom to additionally take the train's vertical displacement into account. The tests have been performed using a passive pantograph at simulated velocities of up to 180 km/h. Facchinetti and various coauthors have published a series of papers showing the progress and newest results of their pantograph test rig from 2004 to 2013 ([2, 11–14]). The improvements were made in terms of the catenary model's complexity (separate carrier and contact wires, as well as dropper slackening [12]), a novel shifting procedure in Ref. [14], a lateral actuator to incorporate stagger [14], and finally an actively controlled pantograph pan head [13]. In each of the aforementioned contributions a modal approach was used to model the catenary's dynamics. In Ref. [15] an HiL test rig is proposed using two actuators for the vertical and one actuator for the horizontal contact wire displacement. The catenary dynamics is modeled in a simplified way (physical mass-spring-damper system at the contact point and pre-recorded displacement trajectories). A commercial pantograph HiL test rig can be found in Ref. [16], where the pantograph is contacted with a spinning disc actuator enabling wear, arcing and temperature tests of the contact strips. Therein the catenary is modeled as a time-varying stiffness, similar as in Ref. [15].

However, the described test rigs face actuation limits in large-displacement tests, e.g. when emulating tunnel entries, and the measured contact force is directly fed into the virtual simulation environment (VSE; here the virtual catenary dynamics) and the reaction (the contact wire's displacement at the pantograph position) is utilized as a tracking reference. Classical tracking control with its intrinsic phase lag fails to provide state-of-the-art control performance as achieved by, for example, predictive control approaches.

Furthermore, ubiquitous test rig imperfections and limitations are not adequately addressed by classical control designs in terms of physical trustworthiness. It was shown in Ref. [17] that the consideration of energy and momentum balances on an HiL test rig can eliminate systematic errors in test results.

The quality of impedance control is always determined by the quality of the underlying model, and the catenary models used so far are either highly simplified, or require large computational domains or artificial damping to avoid spurious unphysical boundary effects.

The main contributions of this paper solve these issues as follows:

a) an HiL actuation concept consisting of a high-dynamic linear drive and a six-degree-of-freedom industry robot that allows for high-dynamic maneuvers in a large operating area;

b) a novel impedance control strategy incorporating energy and momentum conservation, solved by a model predictive control approach to consider constraints and predict the complex catenary dynamics;

c) an efficient real-time-capable Eulerian approach [18] (a fixed pantograph interacts with a moving catenary) to solve the distributed-parameter catenary dynamics combined with special absorbing boundary layers.

In contrast to the control approaches of existing pantograph HiL test rig designs, impedance control in this work is realized via model predictive control (MPC). The basis of the controller is a model of the underlying plant (the test rig actuator) and the VSE (the catenary dynamics), and the future behavior of both is predicted in each time step, where the upcoming control moves are the decision variables in an optimization problem. This allows to incorporate constraints into the control problem and leads to superior control performance by eliminating the phase lag that emerges in classical state feedback laws. For efficiently solving this optimization problem in real time, the size of the underlying models of the MPC is limited. Hence, the proposed catenary model is formulated in a novel efficient form where a special case of controlled boundaries is used. The computational domains of the contact and carrier wires are extended by small controlled boundary layers that absorb all outgoing waves [19]. The periodic excitation emerging from the train ride in combination with the catenary is modeled as a time-varying periodic system.

The importance of obeying physical conservation laws in an impedance-controlled test rig was already shown in Ref. [17] at a combustion engine test rig. There, the fuel consumption on the real track and in the virtual representation were not consistent because small

energy errors emerging from limited control bandwidth accumulated. It was shown that these errors could be eliminated by considering conserved quantities by control.

One major challenge in HiL applications is to establish a robustly stable, yet highly transparent coupling of VSE and UUT. These objectives are conflicting [9], and in Ref. [20] it is shown that causality conflicts result in instability. For haptic interfaces, passivity-based techniques [21, 22] have been proposed to ensure stability of VSE/ UUT coupling. Ref. [23] proposes to combine active and passive actuators with a hybrid control algorithm to improve the stable attainable impedance range.

In power-electronic HiL testing the coupling between the VSE and the UUT was already under investigation in recent papers, but not in terms of conserved quantities' consistency. In Ref. [24] different possible interfacing concepts are discussed and it is also stated that the conservation of energy has to be enforced, although this topic is not pursued further there. In Ref. [25] a circuit for electronic power-HiL simulations is described that relies on perfectly controlled voltage or current sources.

In contrast, the method proposed here guarantees the conservation of energy by introducing a correction term (interpreted as a virtual force) acting on the VSE. This allows the formulation of both energy and momentum conservation laws directly as control goals.

The outline of this paper is as follows: In Section 2 the test rig system setup, the VSE and their interconnection are outlined. All relevant signals, the conserved quantities, as well as the general control goals are specified. Section 3 lays the theoretical foundation for impedance control and presents the control in form of a model predictive controller. As VSE model an efficient railway catenary model structure is described in Section 4. Finally, Section 5 demonstrates the functionality of the proposed control concept with experimental results, followed by conclusions.

2. Problem Description

2.1. High-Dynamic Pantograph Test Rig

The novel high-speed pantograph test rig considered in this work is displayed in Fig. 1. It consists of a linear drive that is attached to a robot arm. A full-size pantograph current collector represents the UUT. This test rig setup allows for large-scale maneuvers such as to emulate tunnel entries and exits (via the robot's motion) as well as vertical displacements in a broad frequency range (achieved via the linear drive) as needed for high-fidelity catenary emulation. In this work, only the linear drive is considered as actuator.

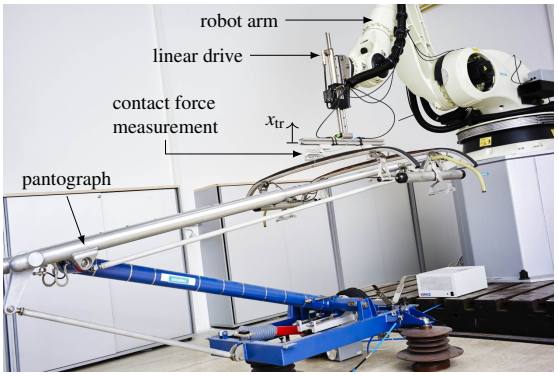

Figure 1: Testbed setup and the UUT (property of Siemens AG Austria, MO MLT BG PN)

The available measurements are the position of the linear drive as well as the contact force at the slider's end position where contact with the pantograph is made.

A mathematical description of the test rig dynamics can be obtained by physical modeling approaches where the relevant dynamics are described by the equations of motion. The parameters are either taken from data sheets or obtained by parameter identification based on measurement data. Another possibility is to describe the input/output behavior of the system solely based on measurement data without any structural assumptions (black-box model). In the following, the test rig dynamics are assumed to be described by a linear time-invariant (LTI) discrete-time state-space system:

$$\begin{aligned} \mathbf{x}_{\mathrm{tr}}(k+1) &= \mathbf{A}_{\mathrm{tr}}\mathbf{x}_{\mathrm{tr}}(k) + \mathbf{B}_{\mathrm{tr}}u_{\mathrm{tr}}(k) \\ \mathbf{y}_{\mathrm{tr}}(k) &= \begin{bmatrix} x_{\mathrm{tr}}(k) \\ \dot{x}_{\mathrm{tr}}(k) \end{bmatrix} = \mathbf{C}_{\mathrm{tr}}\mathbf{x}_{\mathrm{tr}}(k)\,, \end{aligned} \tag{1}$$

with x_{tr} and $\dot{x}_{\mathrm{tr}}$ being the position and velocity of the test rig at the pantograph's contact point, respectively, and $u_{\mathrm{tr}}(k)$ as input signal to the system. The sampling time is denoted by T_{s}. Furthermore, $\mathbf{A}_{\mathrm{tr}}$, $\mathbf{B}_{\mathrm{tr}}$ and $\mathbf{C}_{\mathrm{tr}}$ are the appropriate dynamic, input, and output matrices, respectively.

Remark 1. *Here, the assumption of LTI system dynamics is justified because all nonlinear effects (fricion, cogging force) are already compensated in the underlying test rig control system.*

2.2. Virtual Simulation Environment

The virtual simulation environment (VSE), in this case a dynamic catenary model, is assumed to be available as a linear-time-varying (LTV) discrete-time state-

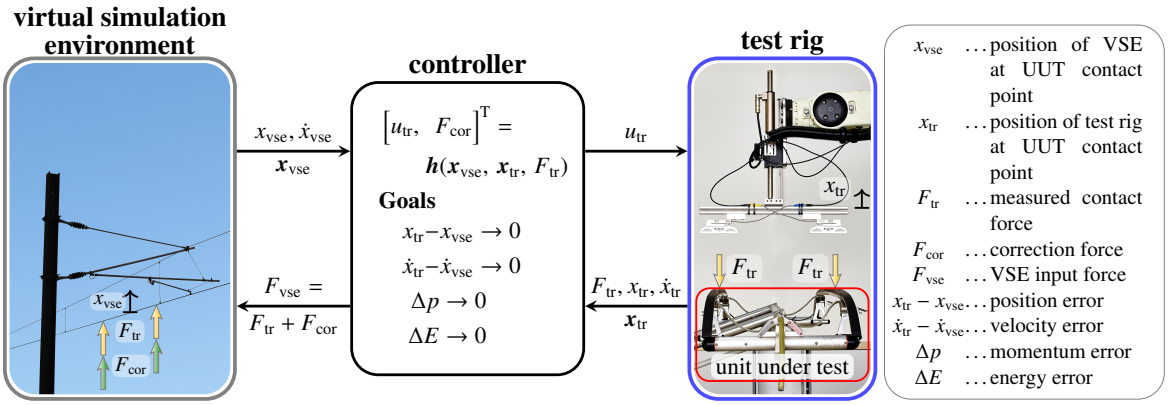

Figure 2: HiL testing control concept: The proposed controller realizes an accurate coupling of the pantograph (unit under test, *right*) and the virtual catenary (VSE, *left*) via the test rig. The controller minimizes the position, velocity, momentum, and energy errors by using both the test rig control input u_{tr} and the virtual correction force F_{cor}, based on model predictions of the test rig and the VSE models.

space model with sampling time T_s realizing the catenary equations of motion as outlined in Section 4:

$$\begin{aligned} \mathbf{x}_{vse}(k+1) &= \mathbf{A}_{vse}(k)\mathbf{x}_{vse}(k) + \mathbf{B}_{vse}(k)F_{vse}(k)\,, \\ \mathbf{y}_{vse}(k) &= \begin{bmatrix} x_{vse}(k) \\ \dot{x}_{vse}(k) \end{bmatrix} = \mathbf{C}_{vse}(k)\mathbf{x}_{vse}(k)\,. \end{aligned} \tag{2}$$

The signals $x_{vse}(k)$ and $\dot{x}_{vse}(k)$ denote the position and velocity of the catenary at the pantograph's contact point at time $t = kT_s$, and F_{vse} is the force input signal into the VSE at the pantograph contact position. The time-varying system matrices are the dynamic matrix $\mathbf{A}_{vse}(k)$, the input matrix $\mathbf{B}_{vse}(k)$ and the output matrix $\mathbf{C}_{vse}(k)$.

2.3. Realization of Accurate Coupling between UUT and VSE

To perform accurate HiL testing, a physically correct coupling between the UUT and the VSE has to be accomplished by control as seen in Fig. 2.

In each sampling interval, the contact force between test rig and pantograph is measured, modified if necessary, and fed into the VSE model as force input. The VSE is set in motion by the forcing, and its response (in terms of catenary vertical displacement x_{vse} and velocity $\dot{x}_{vse}$ at the contact point) serve as reference trajectories to be tracked by the test rig's physical contact point (x_{tr}, $\dot{x}_{tr}$).

This way, the VSE dynamics can be realistically emulated for the UUT.

2.4. Control Tasks

The first task of the controller is to track the position x_{vse} and velocity $\dot{x}_{vse}$ signals of the VSE on the test rig in the UUT/test rig contact point, so that the position and velocity errors are ideally zero:

$$\begin{aligned} e_{pos}(k) &= x_{tr}(k) - x_{vse}(k)\,, \\ e_{vel}(k) &= \dot{x}_{tr}(k) - \dot{x}_{vse}(k)\,. \end{aligned} \tag{3}$$

However, both quantities are different from zero because of test rig limitations, measurement noise and unmodeled system dynamics. This leads to discrepancies in the energy extracted from the UUT and injected into the VSE (also observed in [17]).

To counteract this effect the controller is allowed to modify the measured contact force F_{tr} by adding a correction force F_{cor}:

$$F_{vse}(k) = F_{tr}(k) + F_{cor}(k)\,. \tag{4}$$

Using F_{cor} the controller has the authority to achieve its second task: energy and momentum conservation. Energy conservation is achieved by keeping the difference in energy extracted from the UUT and the energy injected into the VSE small,

$$\Delta E(k) = E_{tr}(k) - E_{vse}(k)\,, \tag{5}$$

where $E_{tr}(k)$ denotes the discretized, cumulated energy exchanged at the contact point between UUT and test rig, and $E_{vse}(k)$ is the energy introduced into the VSE:

$$\begin{aligned} E_{tr}(k) &= \sum_{j=0}^{k} T_s F_{tr}(j)\dot{x}_{tr}(j)\,, \\ E_{vse}(k) &= \sum_{j=0}^{k} T_s \left(F_{tr}(j) + F_{cor}(j)\right)\dot{x}_{vse}(j)\,. \end{aligned} \tag{6}$$

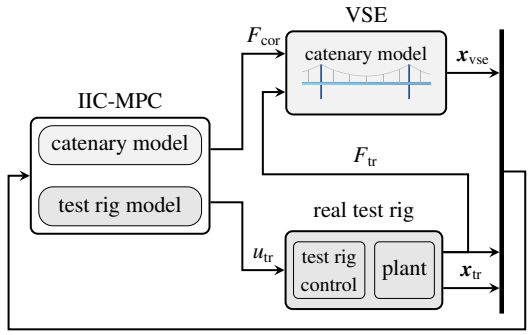

Figure 3: Block diagram of the integrated impedance control (IIC) MPC concept. The MPC controls both the test rig as well as the VSE, thereby optimizing for tracking, momentum, and energy control goals simultaneously.

Thereby, the discrete-time approximations of the energy and momentum integral quantities are used throughout. As can be seen from Eqs. (5) and (6), the energy balance is affected by the choice of F_{cor}. Moreover, a momentum error now emerges due to the different values of F_{tr} and F_{vse}:

$$\begin{aligned}\Delta p(k) &= \sum_{j=0}^{k} T_s F_{tr}(k) - \sum_{j=0}^{k} T_s \left(\underbrace{F_{tr}(k) + F_{cor}(k)}_{F_{vse}(k)} \right) \\ &= \sum_{j=0}^{k} T_s F_{cor}(k)\,. \end{aligned} \tag{7}$$

As a consequence, both momentum and energy conservation have to be considered by control.

Summarizing the controls tasks described in this section, the controller has to minimize the position/velocity errors Eq. (3) while keeping the errors in energy ΔE Eq. (5) and momentum Δp Eq. (7) sufficiently small, as indicated in Fig. 2. This is achieved using both F_{cor} and u_{tr} as control variables and results in a multivariable control law.

3. Control Methodology

3.1. Proposed Integrated Impedance Control Structure

The proposed controller structure is illustrated in Fig. 3. In this variant of an *integrated impedance control* (IIC) architecture [26], the MPC is based on models of both, the test rig dynamics Eq. (1) and the VSE dynamics Eq. (2). Additionally, the controller is given access to two control signals: the test rig control input $u_{tr}(k)$ and the virtual correction force $F_{cor}(k)$.

In contrast to a classical *cascaded* impedance control scheme (in which the controller only tracks the response of the VSE by controlling the test rig), the IIC concept allows predictive lag-free tracking, and the controller's access to the VSE excitation via $F_{cor}(k)$ adds the possibility to control tracking, momentum error, and energy error simultaneously.

A linear time-varying MPC problem is formulated to achieve tracking and momentum error control. This control problem is then augmented by a constraint formulation that results in a reduction of the energy error.

3.2. Linear time-varying MPC formulation for tracking and momentum conservation

The combined prediction model composed of the LTI test rig dynamics Eq. (1), the LTV VSE dynamics Eq. (2), and including the momentum error Eq. (7) reads:

$$\begin{aligned} \mathbf{x}(k+1) &= \mathbf{A}(k)\mathbf{x}(k) + \mathbf{B}(k)\mathbf{u}(k) + \mathbf{E}(k)z(k)\,, \\ \mathbf{y}(k) &= \mathbf{C}(k)\mathbf{x}(k) = \begin{bmatrix} e_{pos}(k) \\ e_{vel}(k) \\ \Delta p(k) \end{bmatrix}, \\ \mathbf{x}(k) &= \begin{bmatrix} \mathbf{x}_{tr}(k) \\ \mathbf{x}_{vse}(k) \\ \Delta p(k) \end{bmatrix}, \mathbf{u}(k) = \begin{bmatrix} u_{tr}(k) \\ F_{cor}(k) \end{bmatrix}, z(k) = F_{tr}(k) \end{aligned} \tag{8}$$

with

$$\begin{aligned} \mathbf{A}(k) &= \begin{bmatrix} \mathbf{A}_{tr} & \mathbf{0} & \mathbf{0} \\ \mathbf{0} & \mathbf{A}_{vse}(k) & \mathbf{0} \\ \mathbf{0} & \mathbf{0} & 1 \end{bmatrix}, \quad \mathbf{B}(k) = \begin{bmatrix} \mathbf{B}_{tr} & \mathbf{0} \\ \mathbf{0} & \mathbf{B}_{vse}(k) \\ \mathbf{0} & T_s \end{bmatrix}, \\ \mathbf{E}(k) &= \begin{bmatrix} \mathbf{0} \\ \mathbf{B}_{vse}(k) \\ 0 \end{bmatrix}, \quad \mathbf{C} = \begin{bmatrix} \mathbf{C}_{tr} & -\mathbf{C}_{vse} & \mathbf{0} \\ \mathbf{0}^T & \mathbf{0}^T & 1 \end{bmatrix}. \end{aligned} \tag{9}$$

The disturbance $z(k)$ acting via $\mathbf{E}$ is the contact force $F_{tr}(k)$.

The vector of future control moves is defined as:

$$\mathbf{U} = \begin{bmatrix} \mathbf{u}^T(k) & \mathbf{u}^T(k+1) & \dots & \mathbf{u}^T(k+N_c-1) \end{bmatrix}^T \tag{10}$$

with the control horizon N_c. This vector is then used in a quadratic cost function to penalize the upcoming control moves and control errors,

$$\begin{aligned} &J(\mathbf{U}, \mathbf{x}, k) = \\ &= \sum_{i=1}^{N_p} \mathbf{x}^T(k+i)\mathbf{Q}\mathbf{x}(k+i) + \sum_{i=0}^{N_c-1} \mathbf{u}^T(k+i)\mathbf{R}\mathbf{u}(k+i) \end{aligned} \tag{11}$$

where N_p and N_c are the prediction and control horizons, respectively. The weighting matrices $\mathbf{Q}$ and $\mathbf{R}$ (both symmetric and positive-definite) are used to penalize the control errors and the input amplitudes, respectively.

To obtain the sequence of optimal future control moves Eq. (10), the optimization problem

$$\mathbf{U}^* = \arg\min_{\mathbf{U}} \quad J(\mathbf{U}, \mathbf{x}(k), k) \tag{12}$$

is solved in each sampling interval. For the unconstrained optimization problem Eq. (12) a closed-form analytic solution can be obtained by solving $\frac{\partial}{\partial \mathbf{U}} J(\mathbf{U}, \mathbf{x}(k), k)\big|_{\mathbf{U}^*} = \mathbf{0}$ for $\mathbf{U}^*$. However, the resulting control moves may not be applicable because of test rig limitations. Linear inequality constraints are incorporated, yielding the constrained convex quadratic programming problem

$$\begin{aligned} \mathbf{U}^* = \arg\min_{\mathbf{U}} \quad & J(\mathbf{U}, \mathbf{x}(k), k) \\ \text{subject to} \quad & \mathbf{M}_\mathbf{U}\mathbf{U} \leq \gamma_\mathbf{u}, \text{ and} \\ & \mathbf{M}_\mathbf{x}\mathbf{X} \leq \gamma_\mathbf{x}\,, \end{aligned} \tag{13}$$

where $\mathbf{M}_\mathbf{U}(k)$ and $\mathbf{M}_\mathbf{x}(k)$ are constraint coefficient matrices that together with the right-hand-side vectors $\gamma_\mathbf{u}$ and $\gamma_\mathbf{x}$ allow to formulate linear input, state, and output inequality constraints with

$$\mathbf{X} = \begin{bmatrix} \mathbf{x}^\mathrm{T}(k) & \mathbf{x}^\mathrm{T}(k+1) & \dots & \mathbf{x}^\mathrm{T}(k+N_\mathrm{p}-1) \end{bmatrix}^\mathrm{T} \tag{14}$$

denoting the stacked vector of predicted states. These states can be calculated by knowledge of the current state vector $\mathbf{x}(k)$, the prediction model Eqs. (8)–(9), and $\mathbf{U}$ from Eq. (10). Since it is in general not possible to obtain a closed-form solution to problems of the form Eq. (13), iterative solvers have to be used, see Ref. [27] for a comprehensive review.

3.3. Energy conservation via constraints

Unlike the momentum error (that can be directly considered in a linear MPC problem), the energy error Eq. (5) depends nonlinearly on the correction force F_cor. The incorporation of energy conservation Eq. (5) directly in the MPC optimization problem (13) would lead to a quadratic optimization problem with nonlinear constraints. This would increase the computational demand significantly and thus render this option unsuitable for real-time MPC with high sampling rates. Instead, suitable constraints on the correction force are formulated that lead to a reduction of the energy error Eq. (5):

$$|\Delta E(k)| < |\Delta E(k-1)|\,. \tag{15}$$

The main result allowing energy conservation in the closed loop is formulated in the following.

Assumption 1. *The closed-loop system realized by Eqs.* (12) *and* (9) *is internally asymptotically stable.*

Theorem 1. *Consider the MPC problem defined in Eqs.* (12) *and* (9) *for which Assumption 1 holds. Then there exist bounds $F^-_\mathrm{cor}(k), F^+_\mathrm{cor}(k)$ for the virtual correction force, $F^-_\mathrm{cor}(k) \leq F_\mathrm{cor}(k) \leq F^+_\mathrm{cor}(k)$, so that the discrete-time energy error $\Delta E(k) = E_\mathrm{tr}(k) - E_\mathrm{vse}(k) \to 0$ as $k \to \infty$.*

Proof of Theorem 1. By considering Eq. (6) the only unknown is $F_\mathrm{cor}(k)$. All other values can either be measured or constructed. For example, the VSE contact point velocity $\dot{x}_\mathrm{vse}(k)$ is expressed as:

$$\begin{aligned} \dot{x}_\mathrm{vse}(k) =& \mathbf{C}^\mathrm{vel}_\mathrm{vse}\mathbf{x}_\mathrm{vse}(k) = \\ & \mathbf{C}^\mathrm{vel}_\mathrm{vse}\mathbf{A}_\mathrm{vse}(k-1)\mathbf{x}_\mathrm{vse}(k-1) + \\ & \mathbf{C}^\mathrm{vel}_\mathrm{vse}\mathbf{B}_\mathrm{vse}(k-1)(F_\mathrm{tr}(k-1) + F_\mathrm{cor}(k-1))\,. \end{aligned} \tag{16}$$

Now a constant $0 < \alpha < 1$ is introduced denoting the decay rate of the energy error. For the case $\Delta E(k-1) > 0$ the following inequality should be met:

$$0 \leq \Delta E(k) \leq \alpha \Delta E(k-1)\,. \tag{17}$$

Starting from Eq. (17) and using Eq. (6) the bounds

$$F^-_\mathrm{cor}(k) \leq F_\mathrm{cor}(k) \leq F^+_\mathrm{cor}(k)\,, \tag{18}$$

can be derived such that Eq. (17) holds. For $\dot{x}_\mathrm{vse}(k) > 0$ this leads to the following expressions for the lower and upper bounds on the correction force $F_\mathrm{cor}(k)$:

$$\begin{aligned} F^-_\mathrm{cor}(k) &= \frac{(1-\alpha)\Delta E(k-1)}{\dot{x}_\mathrm{vse}(k) T_s} + F_\mathrm{tr}(k)\left(\frac{\dot{x}_\mathrm{tr}(k)}{\dot{x}_\mathrm{vse}(k)} - 1\right), \\ F^+_\mathrm{cor}(k) &= \frac{\Delta E(k-1)}{\dot{x}_\mathrm{vse}(k) T_s} + F_\mathrm{tr}(k)\left(\frac{\dot{x}_\mathrm{tr}(k)}{\dot{x}_\mathrm{vse}(k)} - 1\right). \end{aligned} \tag{19}$$

The bounds resulting from the cases $\dot{x}_\mathrm{vse}(k) < 0$ or $\Delta E(k-1) < 0$ are derived analogously, and utilizing a correction force in the corresponding range leads to a reduction in energy error. □

Corollary 1. *The virtual force $F_\mathrm{cor}(k)$ can be used by the proposed MPC via suitable constraints to guarantee long-term energy conservation $\Delta E \to 0$ at the UUT/VSE interface.*

The magnitude of the correction force necessary to decrease the energy $\Delta E(k)$ may grow to arbitrarily large values as $|\dot{x}_{\mathrm{vse}}(k)| \to 0$, as can readily be seen by inspecting Eq. (19). A natural extension of Theorem 1 is to introduce a threshold velocity $\dot{x}_{\mathrm{vse}}^{\mathrm{thr}} > 0$ and impose the bounds Eq. (18) on the correction force only if $|\dot{x}_{\mathrm{vse}}(k)| > \dot{x}_{\mathrm{vse}}^{\mathrm{thr}}$. The threshold has to be chosen small enough so that it is sufficiently often exceeded in order to guarantee energy error reduction.

Theorem 2. *Given an MPC problem Eqs.* (12) *and* (9) *with closed-loop stable test rig and VSE dynamics by Assumption 1, that is excited by an arbitrary force input* $F_{\mathrm{tr}}(k)$ *with* $\lim_{k\to\infty} F_{\mathrm{tr}}(k) = c$, $c \in \mathbb{R}$ *that leads to a system response such that* $|\dot{x}_{\mathrm{vse}}(k)| < \dot{x}_{\mathrm{vse}}^{\mathrm{thr}}\ \forall k$ *(i.e. the energy conserving bounds are never activated), then the resulting energy error Eq.* (6) *stays bounded.*

Proof of Theorem 2. With the system at rest at $k = 0$: $\mathbf{x}(0) = \mathbf{0}$ and assuming a step force input $F_{\mathrm{tr}}(k) = \varphi\sigma(k)$ such that $|\dot{x}_{\mathrm{vse}}(k)| < \dot{x}_{\mathrm{vse}}^{\mathrm{thr}}\ \forall k$ holds from the optimization problem Eq. (12) together with the state-space system Eq. (9) and the step input size φ, the system response can be computed by usage of a linear state-feedback law with a gain matrix $\mathbf{K}_{\mathrm{mpc}}(k)$ (unconstrained MPC problem equivalent to a state-feedback law, see [28])

$$\mathbf{x}(k+1) = \Big(\mathbf{A}(k) - \mathbf{B}(k)\mathbf{K}_{\mathrm{mpc}}(k)\Big)\,\mathbf{x}(k) + \mathbf{E}(k)\varphi\,. \tag{20}$$

The state trajectory defined by Eq. (20) is linearly scaled by the step height φ and therefore the system can be expressed as a discrete-time transfer function $\mathbf{G}(z)$, respectively a convolution summation including its weighting sequence $\mathbf{g}(k) = \mathcal{Z}^{-1}\{\mathbf{G}(z)\}$:

$$\mathbf{x}(k) = \sum_{j=0}^{k} F_{\mathrm{tr}}(j)\mathbf{g}(k-j) = \sum_{j=0}^{k} \varphi\mathbf{g}(k-j)\,. \tag{21}$$

From asymptotic stability of the system (including the summation of F_{cor} in the last state) the vector-norm of the weighting sequence approaches zero:

$$\lim_{k\to\infty} \|\mathbf{g}(k)\| = 0\,. \tag{22}$$

The correction force F_{cor} is then just dependent on φ and can be expressed utilizing the derived weighting sequence $\mathbf{g}(k)$:

$$F_{\mathrm{cor}}(k+1) = \begin{bmatrix}\mathbf{0}^{\mathrm{T}} & 1\end{bmatrix}\mathbf{K}_{\mathrm{mpc}}(k)\mathbf{x}(k) \tag{23}$$

$$= \begin{bmatrix}\mathbf{0}^{\mathrm{T}} & 1\end{bmatrix}\mathbf{K}_{\mathrm{mpc}}(k)\sum_{j=0}^{k}\mathbf{g}(k-j)\varphi \tag{24}$$

$$= \tilde{K}_{\mathrm{mpc}}(k)\varphi\,. \tag{25}$$

$\tilde{K}_{\mathrm{mpc}}(k)$ is used to obtain the value of the correction force at time instant $k+1$ and because of the asymptotic closed-loop stability following limits with exponential decay hold:

$$\lim_{k\to\infty} \left\|\tilde{K}_{\mathrm{mpc}}(k)\right\| = 0\,, \tag{26}$$

$$\lim_{k\to\infty} \dot{x}_{\mathrm{vse}}(k) = 0\,, \tag{27}$$

$$\lim_{k\to\infty} \dot{e}_{\mathrm{vel}}(k) = 0\,, \tag{28}$$

$$\lim_{k\to\infty} F_{\mathrm{cor}}(k) = 0\,. \tag{29}$$

The energy error Eq. (5) then is:

$$\Delta E(k) = \sum_{j=0}^{k}\left[F_{\mathrm{tr}}(j)\dot{e}_{\mathrm{vel}}(j) - F_{\mathrm{cor}}(j)\dot{x}_{\mathrm{vse}}\right]T_{\mathrm{s}} \tag{30}$$

$$< C(\varphi) < \infty\,, \tag{31}$$

where $C(\varphi)$ is a constant only depending on φ and not on k. The inequalities are valid because all summation terms in Eq. (30) are dependent on φ and are exponentially decaying and thus their sum is bounded. □

Corollary 2. *For any sufficiently small and norm-bounded persistent excitation* $F_{\mathrm{tr}}(k)$*, the velocity of the VSE never exceeds the threshold (*$|\dot{x}_{\mathrm{vse}}(k)| < \dot{x}_{\mathrm{vse}}^{\mathrm{thr}}\ \forall k$*). In this case the proposed energy error reduction constraint is never imposed. However, from a convolution summation based on the elementary test case in Theorem 2 it follows that the energy error is Lipschitz-bounded.*

3.4. Robustification Heuristics

In HiL experiments on the pantograph test rig it was observed that ensuring energy conservation through bounds obtained by Eqs. (18) and (19) occasionally led to high-frequency oscillations. It was found that the F_{cor} values needed for energy error reduction can show strong oscillations which induce such high-frequency oscillations in the VSE and subsequently in the test rig.

One way to address these issues is to impose rate constraints on F_{cor}. However, simply imposing constraints on rate and absolute values on F_{cor} together with bounds obtained from energy conservation Eq. (18) may render the optimization problem Eq. (13) infeasible. Therefore, a heuristic relaxation technique is devised to ensure feasibility and consequently to robustify HiL testing by suppressing unwanted high-frequency oscillations. The necessary concept is defined as constraint hierarchy:

Definition 1. *A **constraint hierarchy** $C(\mathcal{A},\mathcal{B})$ is defined as*

$$C(\mathcal{A},\mathcal{B}) = \begin{cases} \mathcal{A}\cap\mathcal{B} & \text{if } \mathcal{A}\cap\mathcal{B}\neq\{\emptyset\} \\ x\in\mathcal{A} : d(\{x\},\mathcal{B}) = d(\mathcal{A},\mathcal{B}) & \text{otherwise} \end{cases} \tag{32}$$

where $\mathcal{A},\mathcal{B}\subset\mathbb{R}$ are nonempty sets, $\{\emptyset\}$ denotes the empty set, and the minimum set distance d is defined as

$$d(\mathcal{A},\mathcal{B}) = \min_{x,y} |x-y|\,,\ x\in\mathcal{A}\,,\ y\in\mathcal{B}. \tag{33}$$

It is noted that for interval constraints represented by $\mathcal{A},\mathcal{B}$, the set C corresponds to that region satisfying both constraints if possible; otherwise preference is given to fulfill constraint $\mathcal{A}$, and $C(\mathcal{A},\mathcal{B})$ is that subset of $\mathcal{A}$ having minimal distance to $\mathcal{B}$.

Proposition 1. *A specific implementation of the constraint hierarchy in Definition 1 is proposed, so that high-frequency oscillations are significantly reduced and energy error reduction is still achieved. The user-defined intervals of the correction force $F_{\mathrm{cor}}(k)$ and its rate are denoted by $\mathcal{F}_{\mathrm{cor,usr}} = \left[F^{\min}_{\mathrm{cor,usr}},\ F^{\max}_{\mathrm{cor,usr}}\right]$ and $\Delta\mathcal{F}_{\mathrm{cor,usr}} = \left[\Delta F^{\min}_{\mathrm{cor,usr}},\ \Delta F^{\max}_{\mathrm{cor,usr}}\right]$, respectively. The bounds obtained by Eqs. (18) and (19) in order to decrease the energy error are denoted by the set $\mathcal{F}^{\mathrm{THM1}}_{\mathrm{cor}} = \left[F^{-}_{\mathrm{cor}}(k),\ F^{+}_{\mathrm{cor}}(k)\right]$. To guarantee feasibility of the constraints, the following constraint hierarchy on $F_{\mathrm{cor}}(k)$ is proposed:*

A. $C_1 = C(\mathcal{F}_{\mathrm{cor,usr}}, \mathcal{F}^{\mathrm{THM1}}_{\mathrm{cor}})$

B. $C_2 = C(F_{\mathrm{cor}}(k-1) + \Delta\mathcal{F}_{\mathrm{cor,usr}}, C_1)$

where the set C_2 defines the admissible interval of $F_{\mathrm{cor}}(k)$.

By implementing the constraint hierarchy concept in Proposition 1, the MPC optimization problem is guaranteed to be feasible and it is assured that no strong, high-frequency excitation input into the VSE is being generated. The rate constraints on F_{cor} are always obeyed. If feasible, also the absolute value constraints on F_{cor} are obeyed. Finally, if also the energy error reduction constraints retain feasibility, then those are also obeyed. This technique may deteriorate energy error minimization performance, but it retains stability and robustness in the application.

4. VSE Model: A Railway Catenary System

For the proposed HiL pantograph test rig a dynamic catenary model of the catenary vertical dynamics is used as VSE model. A typical catenary-pantograph setup is displayed in Fig. 4. Each catenary span is comprised of a carrier wire attached to two masts. Additionally, a contact wire is connected to the carrier wire via several droppers to minimize the static pre-sag. Typically, the wires are modeled as Euler-Bernoulli beams (EBBs) under axial tension in resting coordinates. The pantograph contact is then modeled as a force input signal moving along the catenary and acting on the contact wire [10]. This approach has the disadvantage that model size and thus simulation duration have to be chosen a-priori, which is not suitable for HiL applications. In Ref. [14] a shifting-scheme of the virtual catenary representation to realize a pantograph HiL test rig has been developed. Thereby the catenary model is periodically re-initialized. However, this approach suffers from several disadvantages:

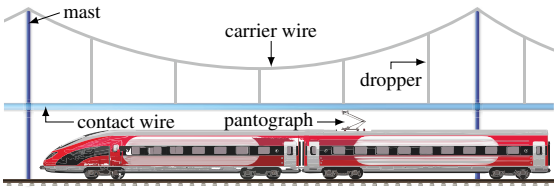

Figure 4: Typical catenary setup

- model size, since for correct computation at least three spans were needed,
- increased implementation effort to avoid periodic shocks due to the shifting procedure.

In this paper the catenary is described in pantograph-fixed coordinates ("Eulerian description") and the underlying PDEs are discretized by finite differences as proposed in Ref. [18]. Additionally, controlled absorbing boundary layers as developed in Ref. [19] were added to both ends of the computational domain to absorb outgoing waves (see Fig. 5). The catenary is assumed periodic in the mast distance (span length), hence a periodic time-varying model structure is obtained where the masts and droppers travel through the domain described in pantograph-fixed coordinates.

In this work, dropper slackening is disregarded, so the catenary model becomes linear. This reduces the computational demands and allows to pre-compute the prediction matrices of the MPC. Additionally, in contrast to Refs. [10, 18] static effects (static solution, pre-sag) are omitted within the catenary model, but instead treated separately as time-varying signal offsets. The resulting system structure is a linear periodically time-

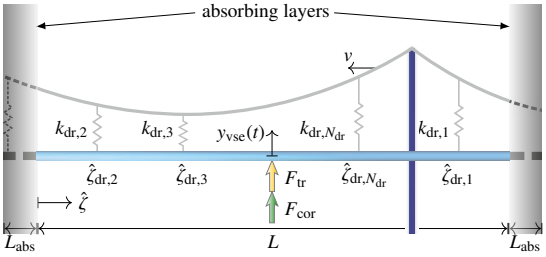

Figure 5: Railway catenary system description where one span is modeled and extended by absorbing layers. In the pantograph-fixed coordinates, the masts and droppers move through the computational domain.

varying (LPTV) system which will be derived in the following sections.

4.1. Equations of Motion

The catenary's dynamics is described by a system of coupled axially loaded EBBs in moving (i.e., pantograph-fixed) coordinates:

$$\begin{aligned}\rho A_{co}\ddot{w}_{co} + \beta_{co}\dot{w}_{co} &= -EI_{co}w''''_{co} + (T_{co} - \rho A_{co}v^2)w''_{co}\\ \ldots + \beta_{co}vw'_{co} - 2\rho A_{co}v\dot{w}'_{co} &+ f_{dr}(\hat{\zeta},t) + f_{contact}(\hat{\zeta}_F,t)\,,\end{aligned} \tag{34}$$

$$\begin{aligned}\rho A_{ca}\ddot{w}_{ca} + \beta_{ca}\dot{w}_{ca} &= -EI_{ca}w''''_{ca} + (T_{ca} - \rho A_{ca}v^2)w''_{ca}\\ \ldots + \beta_{ca}vw'_{ca} - 2\rho A_{ca}v\dot{w}'_{ca} &- f_{dr}(\hat{\zeta},t)\,,\end{aligned} \tag{35}$$

$$\hat{\zeta} \in [0, L + 2L_{abs}]\ , t \in \mathbb{R}^+.$$

Thereby, the fields $w(\hat{\zeta},t)$ denote the vertical displacements as deviations from the stationary deformation of the catenary obtained without pantograph contact. They are functions of time t and the *moving* spatial coordinate $\hat{\zeta} = \zeta + vt$, with the resting spatial coordinate ζ and the velocity of the pantograph v. The constant parameters are the mass per unit length ρA, viscous damping coefficient β, bending stiffness EI, axial load T, and span length L_{span}. The length of the domain interior is L, the length of the computational domain is $L+2L_{abs}$ (see Fig. 5). Additionally, the abbreviations $\dot{w} = \frac{\partial w}{\partial t}$ and $w' = \frac{\partial w}{\partial \hat{\zeta}}$ have been used. The subscripts co and ca denote the parameters and displacements of the contact and carrier wires, respectively. The distributed contact force between the catenary and pantograph is defined in moving coordinates as

$$f_{contact}(\hat{\zeta},t) = F_{vse}(t)\delta_\epsilon(\hat{\zeta}_F)\,, \tag{36}$$

where $\delta_\epsilon(\hat{\zeta}_F)$ is a finite support membership function (see Ref. [10]) at the pantograph position $\hat{\zeta}_F$ (fixed in the moving spatial coordinate). The coupling by means of droppers — here modelled as springs with stiffness $k_{dr,j}$, $j = 1,\ldots,N_{dr}$ (see Fig. 5) — is described by the force distribution

$$\begin{aligned}&f_{dr}(\hat{\zeta},t) = \\ &\sum_{j=1}^{N_{dr}} k_{dr,j}\left(w_{ca}(\hat{\zeta}_{dr,j}(t),t) - w_{co}(\hat{\zeta}_{dr,j}(t),t)\right)\delta_\epsilon(\hat{\zeta}_{dr,j}(t))\end{aligned} \tag{37}$$

where $\hat{\zeta}_{dr,j} = \hat{\zeta}^0_{dr,j} - vt$ is the current position and $\hat{\zeta}^0_{dr,j}$ the starting position of the j-th dropper. Thus the droppers periodically leave and enter the computational domain ($\hat{\zeta}_{dr,j} \in [0, L+2L_{abs}]$). The equations Eqs. (34)–(37) result in a linear periodically time-varying (LPTV) system with $F_{vse}(t)$ being the only exogenous input.

The dynamics of a catenary in a fixed coordinate system can be described by Eqs. (34) and (35) when v is set to 0 m/s and considering that the dropper and mast positions are now time-invariant, whereas the contact force position $\zeta_F(t) = \zeta_{F0} + vt$ now varies as the train is moving under a fixed catenary system:

$$\begin{aligned}\rho A_{co}\ddot{w}_{co} + \beta_{co}\dot{w}_{co} &= -EI_{co}w''''_{co} + T_{co}w''_{co}\\ \ldots + f_{dr}(\zeta,t) &+ f_{contact}(\zeta_F(t),t)\,,\end{aligned} \tag{38}$$

$$\begin{aligned}\rho A_{ca}\ddot{w}_{ca} + \beta_{ca}\dot{w}_{ca} &= -EI_{ca}w''''_{ca} + T_{ca}w''_{ca}\\ \ldots - f_{dr}(\zeta,t)\,.\end{aligned} \tag{39}$$

4.2. Discretization by Finite Differences

To obtain a real-time catenary model as VSE model, the system Eqs. (34)–(37) is first discretized using second-order central differences (see e.g. Ref. [29]) on an equidistant mesh in time and space with suitable mesh sizes Δt and $\Delta\hat{\zeta}$, respectively. These step sizes are typically chosen according to requirements on accuracy, stability, real-time-capability, and memory limits. Thereby, the clamped boundary conditions

$$\begin{aligned}w_{ca}(x=0,t) = w_{ca}(x=L+2L_{abs},t) &= 0\\ w_{co}(x=0,t) = w_{co}(x=L+2L_{abs},t) &= 0\\ w'_{ca}(x=0,t) = w'_{ca}(x=L+2L_{abs},t) &= 0\\ w'_{co}(x=0,t) = w'_{co}(x=L+2L_{abs},t) &= 0\end{aligned}$$

are assumed (for the deviations from the static solution).

Then, the absorbing layers are implemented according to the method described in [19], where a state feedback control law is used to calculate forces acting on each node in the boundary layers so that they mimic the

behavior of perfectly matched layers and avoid reflections of outgoing wave packets back into the domain interior.

Denoting the time index of the Δt-sampled system by n ($t = n\Delta t$), the implicit LPTV system is obtained as:

$$\mathbf{A}_{+1}(n)\,\mathbf{w}(n+1) = \mathbf{A}_0(n)\,\mathbf{w}(n) + \mathbf{A}_{-1}\mathbf{w}(n-1) + \mathbf{B}(n)F_{\mathrm{vse}}(n)\,. \quad (40)$$

Thereby, the collocated localized displacements are defined as

$$\mathbf{w}(n) = \begin{bmatrix}\mathbf{w}_{\mathrm{ca}}^{\mathrm{T}}(n) & \mathbf{w}_{\mathrm{co}}^{\mathrm{T}}(n)\end{bmatrix}^{\mathrm{T}} \text{ and}$$
$$\mathbf{w}_l(n) = \begin{bmatrix}w_l(0, n\Delta t), w_l(\Delta\zeta, n\Delta t), \ldots, w_l(L, n\Delta t)\end{bmatrix}^{\mathrm{T}},$$

with $l = \{\mathrm{co}, \mathrm{ca}\}$. The matrices $\mathbf{A}_{+1}(n)$ and $\mathbf{A}_0(n)$ are time-varying due the dropper movement and a Crank-Nicolson-type [30] implicit formulation of the dropper stiffness terms was utilized to improve stability if high-stiffness droppers were modeled. Aggregating the states as

$$\mathbf{x}_{\mathrm{vse}}(n) = \begin{bmatrix}\mathbf{w}^{\mathrm{T}}(n) & \mathbf{w}^{\mathrm{T}}(n-1)\end{bmatrix}^{\mathrm{T}}$$

and solving Eq. (40) explicitly for $\mathbf{x}_{\mathrm{vse}}(n+1)$, one obtains the discrete-time LPTV system

$$\begin{aligned}\mathbf{x}_{\mathrm{vse}}(n+1) &= \mathbf{A}_{\mathrm{vse}}(n)\mathbf{x}_{\mathrm{vse}}(n) + \mathbf{B}_{\mathrm{vse}}(n)F_{\mathrm{vse}}(n)\,, \quad (41)\\ \mathbf{y}_{\mathrm{vse}}(n) &= \mathbf{C}_{\mathrm{vse}}\mathbf{x}_{\mathrm{vse}}(n)\,.\end{aligned}$$

The system dynamics in Eq. (41) is sampled with sampling time Δt. However, to allow for faster computation several time steps can be aggregated with the input held constant. If so, an integer down-sampling factor $m_\downarrow$ is defined with $T_\mathrm{s} = m_\downarrow \Delta t$, $m_\downarrow \in \mathbb{N}$ and the time steps are chosen so that, additionally, the system is periodic in an integer number of samples N_{per} in either time base:

$$\begin{aligned}N_{\mathrm{per},\Delta t} &= \frac{L_{\mathrm{span}}}{v\Delta t} \in \mathbb{N} \text{ and}\\ N_{\mathrm{per},T_\mathrm{s}} &= \frac{N_{\mathrm{per},\Delta t}}{m_\downarrow} = \frac{L_{\mathrm{span}}}{vT_\mathrm{s}} \in \mathbb{N}\,.\end{aligned} \quad (42)$$

To express Eq. (2) in the down-sampled time base T_s, Eq. (41) is applied $m_\downarrow$ times to express $\mathbf{x}_{\mathrm{vse}}(n + m_\downarrow) = \mathbf{x}_{\mathrm{vse}}(k+1)$ with $k = m_\downarrow n$ (see Ref. [31] for the time-invariant down-sampling; the time-varying case is notably more tedious notationally and omitted here). The input force is kept constant over the down-sampling duration $F_{\mathrm{vse}}(n) = F_{\mathrm{vse}}(n+i)\,, i = 1 \ldots m_\downarrow - 1$.

Remark 2. *It is noted that the matrices $\mathbf{A}_{+1}(n)$, $\mathbf{A}_0(n)$ and $\mathbf{A}_{-1}(n)$ are sparse matrices, whereas the resulting matrix $\mathbf{A}_{\mathrm{vse}}(n)$ is densely populated.*

wire	ρA kg/m	β kg/s/m	EI N m^2	T N
contact	1.35	0	150	20×10^3
carrier	1.35	0	150	20×10^3
dropper j	1	2	3	4
$\hat{\zeta}_{\mathrm{dr},j}$ in m	5	21.67	38.33	55
$k_{\mathrm{dr},j}$ in N/m	1000	1000	1000	1000
	F_{static}	T_s	$\Delta\zeta$	$\Delta t = \frac{T_\mathrm{s}}{m_\downarrow}$
pantograph-fixed	120 N	1/170 s	1.54 m	1/850 s
catenary-fixed	120 N	1/68 000 s	0.24 m	-

Table 1: Parameters of both catenary models.

In the following section, the down-sampled version of model Eq. (41) will be compared to a catenary-fixed reference formulation to show that the described reductions (absorbing layers and down-sampling) are indeed suitable to model the main catenary dynamics in a frequency range up to 20 Hz.

4.3. Real-Time Catenary Model Parameters and Basic Validation

To demonstrate the test rig control concept, in this work a simplified real-time pantograph-fixed catenary model is utilized that is briefly validated against a catenary-fixed reference simulation from Ref. [32]. The reference model framework fulfills the requirements of the simulation validation part of EN50318 [33][1]. It utilizes a much smaller sampling time and element discretization and the parameter values and catenary setup are summarized in Table 1. As a simplified choice, based on EN50318 [33] both wires' parameters were chosen identical. However, the catenary setup can easily be generalized to arbitrary catenary parameters but then requires additional tuning of the absorbing layers' parameters specifically for each wire.

The sampling time of the LPTV catenary model is chosen according to the available computational power and memory resources of the deployed real-time computer, see Section 5. The total length of the computational domain was set to the length of one span $L + 2L_{\mathrm{abs}} = L_{\mathrm{span}} = 60\,\mathrm{m}$. The length of each absorbing layer was chosen to $L_{\mathrm{abs}} = 4.62\,\mathrm{m}$.

[1] The validation in this standard consists of two parts: first by means of a reference simulation and second by means of measurement data. The first part of the EN50318 could be met, the second part could not be performed due the lack of suitable measurement data.

For validation of the reduced LPTV model against the high-fidelity reference simulation a pantograph based on the model used in [33] with a reduced contact stiffness and a static uplift force of 120 N is moving with a speed of 60 m/s. Fig. 6 shows the displacement of the contact wire at the pantograph's position of both models in the time domain and the resulting contact force in the frequency domain. It can be seen that the pantograph-fixed model shows less compliance at the span frequency of 1 Hz, but the relative shape is preserved well. Also, the low-frequency content of the contact force is reproduced well, and higher frequency contents are attenuated compared to the reference solution. Especially when compensating the gain error by correcting the static displacement by a constant factor the position trajectories are in overall good agreement (fit of 88.7 %, respectively 75.5 % in the uncompensated case, both calculated in a normalized mean square error computation).

4.4. Discussion of the LPTV catenary model

In principle, the reduced real-time catenary model's parameter can be arbitrarily chosen as long as the desired model quality is attained. This is valid over a wide range of possible wire parameters and pantograph speeds. In this work the choices on the sampling time Δt (and especially its down-sampled version T_s) and the total length $L+2L_\mathrm{abs}$ were made in close coordination with system limitations of the real-time computer, see Sec. 5. The length L_abs of the absorbing layer should generally be chosen only as large as necessary to sufficiently attenuate the reflections of outgoing wave packets back into the domain.

The observed deviation from the catenary-fixed formulation (visualized in Fig. 6) arises mainly from a substantially coarser spatial discretization (see bottom of Table 1) as well as the small computational area where the absorbing layers even attenuate physical relevant contributions of the pantograph-catenary interaction. Further comparative simulation studies revealed that increasing the length L enhances model quality significantly. Here, the small lengths of L and L_abs were necessary to meet memory requirements of the real-time hardware. For the same reason the down-sampling to the slower T_s-time-base was introduced, drastically reducing the amount of matrices needed to describe the catenary dynamics in Eq. (2).

A significant simplification decision is to disregard dropper slackening, yielding a linear model and, in turn, allowing to employ the subsampling procedure as outlined in Sec. 4.2. Under such aggregation over time (producing densely populated system matrices in Eq. (41)), an online re-computation is currently not feasible in real time (which would allow to consider dropper slackening). Disregarding dropper slackening is also assumed to be the main reason of the relatively small asymmetry of the trajectory of the contact wire's displacement at the pantograph position, even for higher tested speeds.

One alternative approach to consider dropper slackening during computation is utilized in a finite-element catenary code reviewed in Ref. [34]: there the slackening is considered by right-hand-side correction forces determined iteratively in each time step. Yet another approach is to directly perform online adaptations of the sparse stiffness matrices in each time step, which is currently under investigation by this work's authors.

Having mentioned the considered model's limitations, in turn, the moving-coordinate (pantograph-fixed) formulation shows the following significant advantages over a classical formulation:

- 6.25 times fewer states per span for similar fidelity,
- strongly shortened computational domain: For this setup a 5 s-run of the catenary-fixed formulation requires a simulation area of 15 spans (900 m) to avoid reflections versus 1 span (60 m) of the pantograph-fixed formulation.
- each second simulated takes about 460 s (catenary-fixed) compared to ≈ 83 ms of the pantograph-fixed formulation[2].

Taking these facts into account, the proposed coordinate transform and the use of absorbing layers (see Fig. 5) lead to a good trade-off between computational effort and accuracy and is thus well-suited for real-time applications. Especially the linear time-varying structure of the real-time model allows to directly employ a high-fidelity catenary model in an MPC algorithm. This allows to use, for example, a nonlinear finite-elements-based high-fidelity catenary model as an on-line reference from whose states the MPC's linear catenary model (as shown here) is initialized in each time instance.

5. Experimental Results

In this Section the methods presented so far will be demonstrated on a real-world pantograph test rig. An

[2] on a standard PC (Intel i7 3.2 GHz)

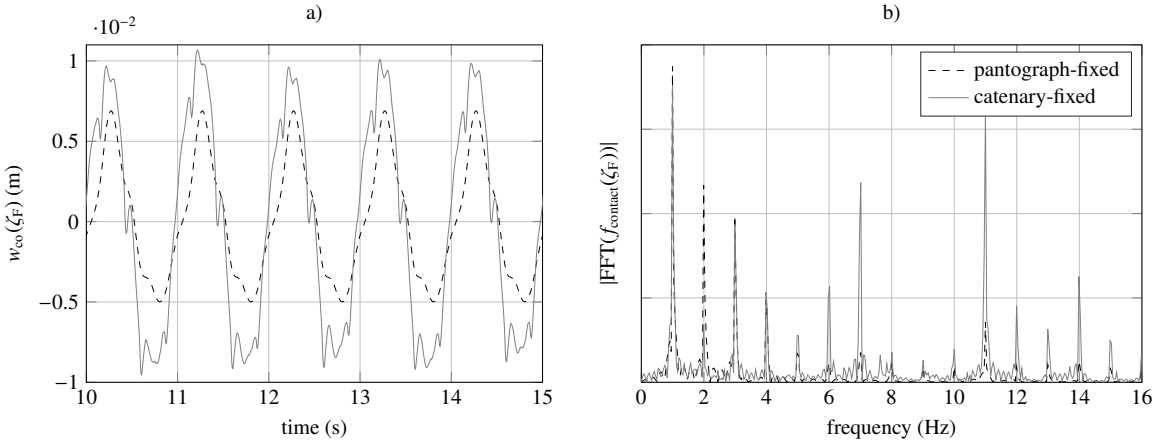

Figure 6: Validation of the catenary model: a) displacement over time (left) and b) the frequency domain representation of the contact force (right) obtained by a Fast Fourier Transform (FFT).

extended IIC-MPC as described in Section 3 is implemented with energy and momentum conservation capabilities. The VSE is a high-order, linear, periodically time-varying state-space model of a catenary that represents a train ride at $v = 60\,\mathrm{m/s}$.

5.1. Implementation Details

The test rig depicted in Fig. 1 consists of an industrial robot with an attached linear drive. In this work, only the latter was actuated because the regular operating conditions (no tunnel entries) can already be captured in its operating range. A classic LQR control law with a sampling rate of 5000 Hz is used as the inner test rig control loop, where the motor current was the control variable. The LTI state-space system of the test rig Eq. (1) as used for the model predictive impedance control is thus already a controlled subsystem. The sampling rate of the LQR controlled system was chosen as fast as possible to allow for best possible tracking control and disturbance rejection. The linear drive positions as well as the contact force are available as measurements. The MPC as well as the test rig control are implemented on a dSPACE DS1006 real-time platform with a 2.8 GHz quad-core processor. Table 2 summarizes MPC implementation details, whereby the weighting matrix $\mathbf{Q}$ is calculated as

$$\mathbf{Q} = \mathbf{C}^{\mathrm{T}}\tilde{\mathbf{Q}}\mathbf{C}\,. \tag{43}$$

Low control weights are put on the velocity error when designing the MPC, so controlling the position and momentum errors are the main control goals. Furthermore,

$1-\alpha$	$\dot{x}_{\mathrm{vse}}^{\mathrm{thr}}$	$N_{\mathrm{p}}, N_{\mathrm{c}}$
6×10^{-6}	0.01 m/s	25
$\tilde{\mathbf{Q}}$	$\mathbf{R}$	T_{s}
$\begin{bmatrix}1&0&0\\0&10^{-4}&0\\0&0&10^{3}\end{bmatrix}$	$\begin{bmatrix}1&0\\0&50\end{bmatrix}$	1/170 s

Table 2: MPC parameters

$1-\alpha$ (the energy error decay factor, see Eq. (17)) is arbitrarily chosen as $(1-\alpha)/T_{\mathrm{s}} = 0.001$ corresponding to a time constant of $\tau = 1000\,\mathrm{s}$. Its value is chosen so as not to significantly affect the VSE dynamics at relevant frequencies. Additionally, a velocity threshold is chosen which deactivates constraints $F_{\mathrm{cor}}^{-}(k)$, $F_{\mathrm{cor}}^{+}(k)$ on the correction force $F_{\mathrm{cor}}(k)$ for $|\dot{x}_{\mathrm{vse}}(k)| < \dot{x}_{\mathrm{vse}}^{\mathrm{thr}}$ as described by Theorem 2.

5.2. HiL Results

To demonstrate energy and momentum correcting properties of the MPC an HiL test run is started with **deactivated** energy conservation in the controller (no bounds on $F_{\mathrm{cor}}(k)$ are imposed, but high input weighting on $F_{\mathrm{cor}}(k)$, so that almost exclusively the test rig input $u_{\mathrm{tr}}(k)$ is utilized for classical impedance tracking).

Due to the neglected dynamics of the pantograph as the UUT, the limited test rig bandwidth as well as imperfections such as noise or uncertainties, a small velocity error emerges and thus an energy error $\Delta E(k)$ accumulates. Then, the MPC correction force con-

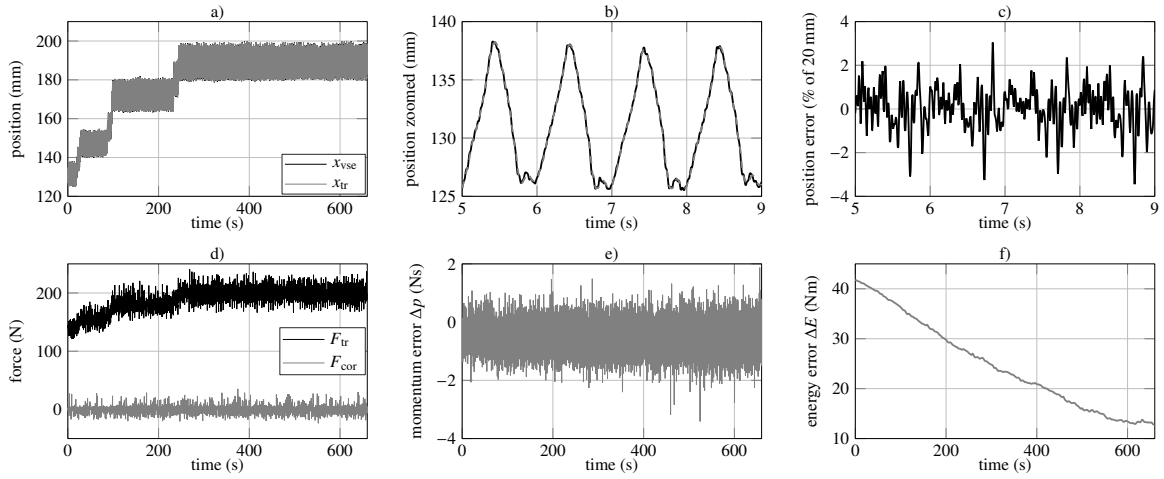

Figure 7: Results of a typical HiL test run demonstrating functional catenary impedance tracking, as well as energy and momentum conservation between the UUT and the VSE. Subplot a) shows the position trajectories over a large time span with varying pantograph uplift force, demonstrating the method's robustness. Subplot b) shows a zoomed view of the trajectories and c) the corresponding position error in percent. Subplot d) shows the contact, respectively the correction force and e) shows that the momentum error stays bounded while the energy error between the UUT and the VSE is decreasing.

straints are globally **activated**, except for small velocities: $|\dot{x}_{\mathrm{vse}}(k)| < \dot{x}_{\mathrm{vse}}^{\mathrm{thr}}$ (see Theorem 2). The results from this time instant on are displayed in Fig. 7. The first row of Fig. 7 shows the impedance tracking behavior. The main task of impedance control, namely tracking the VSE's dynamic behavior by the test rig is excellently achieved: high position tracking performance with no phase-lag even under high dynamic movements can be observed in Fig. 7b, which shows a detailed view of the position trajectories of the test rig respectively the VSE from Fig. 7a. Fig. 7c depicts the corresponding normalized tracking error.

To demonstrate the method's robustness in terms of altered UUT dynamics, the pantograph's contact force is varied in the range of 130 N to 220 N by changing the pantograph's bellow pressure, as visualized in Fig. 7d. There it is also demonstrated that only modest control action on F_{cor} is applied at the catenary. Additionally, the momentum error shown in Fig. 7e introduced by the artificial correction force stays bounded (its integral was not part of the control goal and thus a nonzero steady-state error remains). The energy error Eq. (5) is visualized in Fig. 7f, and for the first 600 s it is continuously decreasing. In contrast to Theorem 1, however, the energy error is not strictly monotonically decreasing because of the threshold on the VSE's velocity, as well as the constraint hierarchy described in Section 3.4. The energy error decays faster than the chosen time constant of τ =1000 s, which has been defined as an upper bound in Eq. (17). For times $t > 600$ s, a residual energy error remains and no further reduction is possible by the proposed test rig controller with the current settings. Noting that in Eq. (19) the magnitude of the correction force is scaled by the magnitude of the energy error, the authors attribute the nonzero energy error to the fact that the energy error reduction (via F_{cor}) is outweighed by the energy errors generated by model errors and imperfections. To investigate this phenomenon further, the MPC constraint hierarchy is considered. To do so, the energy error is split into two parts:

$$\Delta E(k) = \Delta E_{\mathrm{ON}}(k) + \Delta E_{\mathrm{OFF}}(k)\,, \tag{44}$$

where at each sampling interval only one of these elements contributes (is non-zero). The term $\Delta E_{\mathrm{ON}}(k)$ sums up all changes in the energy error when bounds obtained via Eq. (19) were active on $F_{\mathrm{cor}}(k)$, i.e. energy error minimization was active. In contrary, if the threshold velocity was not exceeded ($|\dot{x}_{\mathrm{vse}}(k)| < \dot{x}_{\mathrm{vse}}^{\mathrm{thr}}$) or the constraint hierarchy prevented the use of energy conserving constraints on $F_{\mathrm{cor}}(k)$, the change in the energy error was summed up in $\Delta E_{\mathrm{OFF}}(k)$. These accumulated energy error contributions $\Delta E_{\mathrm{ON}}(k)$ and $\Delta E_{\mathrm{OFF}}(k)$ are defined as

$$\Delta E_{\mathrm{ON}}(k) = \sum_k \epsilon_{\mathrm{ON}}(k) \text{ and } \Delta E_{\mathrm{OFF}}(k) = \sum_k \epsilon_{\mathrm{OFF}}(k)\,, \tag{45}$$

with

$$\epsilon_{\mathrm{ON}}(k) = \begin{cases} \Delta E(k) - \Delta E(k-1) & \text{Eq. (19) activated} \\ 0 & \text{else} \end{cases} \tag{46}$$

and

$$\epsilon_{\mathrm{OFF}}(k) = \begin{cases} \Delta E(k) - \Delta E(k-1) & \text{Eq. (19) deactivated} \\ 0 & \text{else}\,. \end{cases} \tag{47}$$

Fig. 8 shows the computed accumulated errors $\Delta E_{\mathrm{OFF}}(k)$ and $\Delta E_{\mathrm{ON}}(k)$ with dashed lines. Furthermore $\Delta E(k)$ and a zoomed segment of $\Delta E(k)$ where sequences with activated (black) and deactivated (gray) constraints are shown.

These results show, based on the accumulated error, that the energy error is increasing when the constraints are deactivated and is decreasing when the constraints are activated.

The proposed heuristics enables a robust implementation of high-dynamic test rig control that keeps momentum and energy errors small despite model imperfections and disturbances, while at the same time achieving excellent impedance tracking performance.

Remark 3. *As a final remark, considering the energy error in the control concept is seen to strongly improve the stability of the coupled system. Coupling the system to a moderately stiff environment (here, by simulating a contacted linear pantograph dynamics) and with typical model errors present, simulation studies show that considering the energy conservation allows safe operation at significantly higher model errors. In turn, if energy errors were ignored by the controller, destabilization at high frequencies quickly emerged. This typical result demonstrates the robustifying effect of considering and controlling energy errors in the impedance controller. It is finally noted that the stabilizing passivity-based schemes in haptic interaction control (such as the energy-bounding algorithm [21]) are closely related to the concept of energy conservation via control.*

6. Conclusions

To obtain physically trustworthy results from an HiL test run, the UUT/VSE coupling has to be tracked accurately, and moreover the physical conservation laws (energy and momentum) have to be made consistent at the UUT/VSE interface. A model-predictive impedance control concept has been proposed that realizes these control tasks for high-dynamic railway catenary emulation in a pantograph current collector test rig. The distributed-parameter virtual catenary dynamics is realized by a high-order time-varying state space description based on a finite difference approximation of the model equations and integrated into the MPC. Specifically, a novel moving-coordinate (pantograph-fixed) Eulerian catenary description combined with absorbing boundaries of the computational domain yield a real-time-capable model with high fidelity.

In order to balance and control momentum and energy errors at the interface simultaneously, the MPC controls both the test rig input as well as the VSE excitation force. Its predictive structure allows to attain lag-free tracking and thus to realize a high-quality interface, which additionally is consistent in the long run in terms of conserved quantities.

Experimental results on the full-scale test rig in contact with a real pantograph validate the proposed method and show the high tracking performance and the conservation properties of the control concept. This allows highly realistic HiL testing of pantographs in virtual test rides on high-speed tracks. Ongoing research work aims at realizing alternative, finite-element-based realtime catenary models to significantly alleviate current computational and memory requirements and further improve HiL testing fidelity.

Acknowledgement

This work was financially supported by the Austrian Research Promotion Agency (projects 836449 and 841331). The authors are grateful for the support of the Siemens pantographs team (Siemens AG Austria, MO MLT BG PN).

References

[1] J. H. Lee, T. W. Park, H. K. Oh, Y. G. Kim, Analysis of dynamic interaction between catenary and pantograph with experimental verification and performance evaluation in new high-speed line, Vehicle System Dynamics 53 (8) (2015) 1117–1134.

[2] A. Facchinetti, L. Gasparetto, S. Bruni, Real-time catenary models for the hardware-in-the-loop simulation of the pantograph/catenary interaction, Vehicle System Dynamics 51 (4) (2013) 499–516. doi:10.1080/00423114.2012.748920.

[3] W. Zhang, G. Mei, X. Wu, Z. Shen, Hybrid simulation of dynamics for the pantograph-catenary system, Vehicle System Dynamics 38 (6) (2002) 393–414.

[4] N. Hogan, Impedance control: An approach to manipulation, in: American Control Conference, 1984, IEEE, 1984, pp. 304–313.

[5] N. Hogan, Impedance control: An approach to manipulation: Part II: Implementation, Journal of dynamic systems, measurement, and control 107 (1) (1985) 8–16.

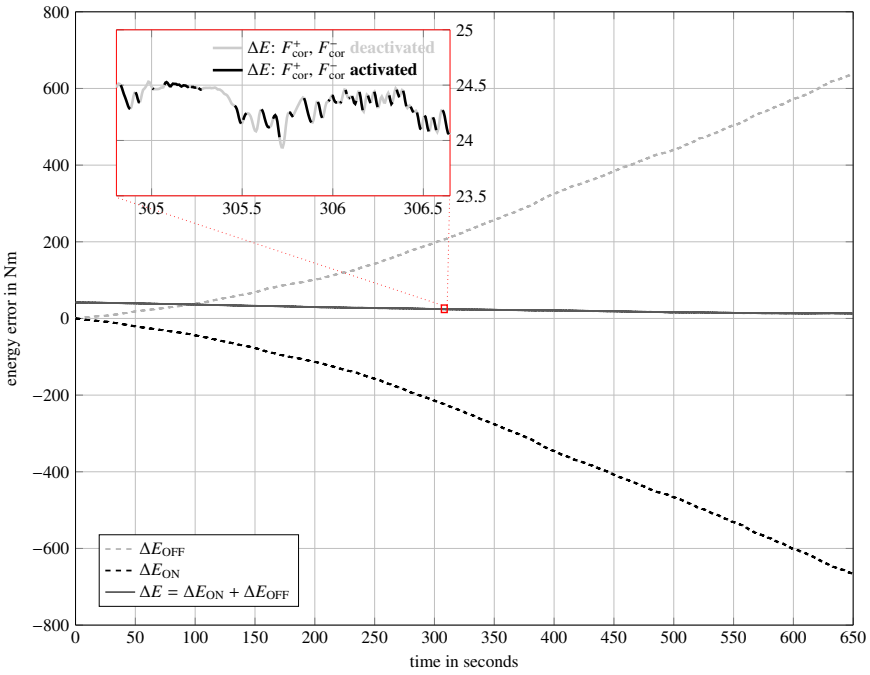

Figure 8: Detailed analysis of the constraint activity with activated energy conversation: 1) Zoomed view shows how ΔE is split into parts with activated (black, solid) and deactivated (gray, solid) F_{cor} constraints. 2) Accumulated energy error contributions ΔE_{ON} (black, dashed) and ΔE_{OFF} (gray, dashed) are decreasing and increasing, respectively.

[6] C. Westermayer, R. Priesner, M. Kozek, R. Bauer, High dynamic torque control for industrial engine test beds, Industrial Electronics, IEEE Transactions on 60 (9) (2013) 3877–3888.

[7] O. König, C. Hametner, G. Prochart, S. Jakubek, Battery emulation for power-HIL using local model networks and robust impedance control, Industrial Electronics, IEEE Transactions on 61 (2) (2014) 943–955.

[8] P. F. Hokayem, M. W. Spong, Bilateral teleoperation: An historical survey, Automatica 42 (12) (2006) 2035–2057.

[9] C. Passenberg, A. Peer, M. Buss, A survey of environment-, operator-, and task-adapted controllers for teleoperation systems, Mechatronics 20 (7) (2010) 787–801.

[10] M. Arnold, B. Simeon, Pantograph and catenary dynamics: A benchmark problem and its numerical solution, Applied Numerical Mathematics 34 (4) (2000) 345–362.

[11] A. Collina, A. Facchinetti, F. Fossati, F. Resta, Hardware in the loop test-rig for identification and control application on high speed pantographs, Shock and Vibration 11 (3-4) (2004) 445–456.

[12] F. Resta, A. Facchinetti, A. Collina, G. Bucca, On the use of a hardware in the loop set-up for pantograph dynamics evaluation, Vehicle System Dynamics 46 (S1) (2008) 1039–1052.

[13] A. Facchinetti, M. Mauri, Hardware-in-the-loop overhead line emulator for active pantograph testing, Industrial Electronics, IEEE Transactions on 56 (10) (2009) 4071–4078.

[14] A. Facchinetti, S. Bruni, Hardware-in-the-loop hybrid simulation of pantograph–catenary interaction, Journal of Sound and Vibration 331 (12) (2012) 2783–2797.

[15] J. Deml, W. Baldauf, A new test bench for examinations of the pantograph-catenary interaction, in: Proc. WCRR, 2001, pp. 25–29.

[16] M. S. Corporation, High-performance pantograph testing, Tech. rep. (02 2010).

[17] S. Jakubek, E. Luchini, A. Oberhummer, F. Pfister, A model-based interfacing concept for accurate power hardware-in-the-loop systems, Mathematical and Computer Modelling of Dynamical Systems (2015) 1–20.

[18] D. Ritzberger, E. Talic, A. Schirrer, Efficient simulation of railway pantograph/catenary interaction using pantograph-fixed coordinates, IFAC-PapersOnLine 48 (1) (2015) 61–66, 8th Vienna International Conference on Mathematical Modelling, MATHMOD 2015.

[19] D. Ritzberger, A. Schirrer, S. Jakubek, Absorbing boundary layer control for axially moving materials, Journal of Vibration and Control (under review).

[20] P. Gawthrop, S. Neild, A. Gonzalez-Buelga, D. Wagg, Causality in real-time dynamic substructure testing, Mechatronics 19 (7) (2009) 1105–1115.

[21] J.-P. Kim, J. Ryu, Robustly stable haptic interaction control using an energy-bounding algorithm, The International Journal of Robotics Research 29 (6) (2010) 666–679.

[22] S. Park, C. Seo, J.-P. Kim, J. Ryu, Robustly stable rate-mode bilateral teleoperation using an energy-bounding approach, Mechatronics 21 (1) (2011) 176–184.

[23] O. Baser, H. Gurocak, E. I. Konukseven, Hybrid control algorithm to improve both stable impedance range and transparency in haptic devices, Mechatronics 23 (1) (2013) 121–134.

[24] S. Lentijo, S. D'Arco, A. Monti, Comparing the dynamic performances of power hardware-in-the-loop interfaces, Industrial Electronics, IEEE Transactions on 57 (4) (2010) 1195–1207.

[25] X. Wu, S. Lentijo, A. Monti, A novel interface for power-hardware-in-the-loop simulation, in: Computers in Power Electronics, 2004. Proceedings. 2004 IEEE Workshop on, IEEE, 2004, pp. 178–182.

[26] R. Priesner, S. Jakubek, Mechanical impedance control of rotatory test beds, Industrial Electronics, IEEE Transactions on 61 (11) (2014) 6264–6274.

[27] P. E. Gill, E. Wong, Methods for convex and general quadratic programming, Mathematical Programming Computation 7 (1) (2014) 71–112.

[28] E. F. Camacho, C. B. Alba, Model predictive control, Springer Science & Business Media, 2013.

[29] R. LeVeque, Finite Difference Methods for Ordinary and Partial Differential Equations: Steady-State and Time-Dependent Problems (Classics in Applied Mathematics Classics in Applied Mathemat), Society for Industrial and Applied Mathematics, Philadelphia, PA, USA, 2007.

[30] J. Crank, P. Nicolson, A practical method for numerical evaluation of solutions of partial differential equations of the heat-conduction type, Mathematical Proceedings of the Cambridge Philosophical Society 43 (1947) 50–67.

[31] K. Ogata, Discrete-time control systems, Vol. 2, Prentice Hall Englewood Cliffs, NJ, 1995.

[32] A. Schirrer, E. Talic, M. Kozek, A flexible MATLAB-based simulation framework for dynamic catenary-pantograph interaction and co-simulation, in: Modelling and Simulation (EUROSIM), 2013 8th EUROSIM Congress on, 2013, pp. 288–293.

[33] EN 50318: Railway applications - current collection systems - validation of simulation of the dynamic interaction between pantograph and overhead contact line., European Committee for Electrotechnical Standardization.

[34] S. Bruni, J. Ambrosio, A. Carnicero, Y. H. Cho, L. Finner, M. Ikeda, S. Y. Kwon, J.-P. Massat, S. Stichel, M. Tur, et al., The results of the pantograph–catenary interaction benchmark, Vehicle System Dynamics 53 (3) (2015) 412–435.

List of scientific publications

International Journals:

1. Emir Talic, Alexander Schirrer, Martin Kozek, Stefan Jakubek
   Multi-objective parameter identification of Euler-Bernoulli beams under axial load
   Journal of Sound and Vibration, Volume 341, 2015, Pages 86-99, ISSN 0022-460X, DOI: 10.1016/j.jsv.2014.12.012

2. Alexander Schirrer, Emir Talic, Guilherme Aschauer, Martin Kozek, Stefan Jakubek,
   Optimization based determination of highly absorbing boundary conditions for linear finite difference schemes
   Journal of Sound and Vibration, Volume 365, 2016, Pages 45–69, ISSN 0022-460X
   DOI: 10.1016/j.jsv.2015.12.006

3. Guilherme Aschauer, Emir Talic, Alexander Schirrer, Martin Kozek and Stefan Jakubek.
   Catenary Emulation for Hardware-in-the-Loop Pantograph Testing with a Model Predictive Energy-Conserving Control Algorithm
   Mechatronics, accepted with minor revision

International Conferences:

1. A. Schirrer, E. Talic, M. Kozek
   A Flexible MATLAB-based Simulation Framework for Dynamic Catenary-Pantograph Interaction and Co-Simulation
   2013 8th EUROSIM Congress on Modelling and Simulation, IEEE, 2013
   ISBN: 978-0-7695-5073-2, S. 288 - 293.

2. M. Fichtinger, E. Talic, A. Schirrer
   Quantification of phase and runtime errors in finite difference approximations of railway catenary systems
   8th European Nonlinear Dynamics Conference ENOC 2014, Wien
   ISBN: 978-3-200-03433-4

3. D. Ritzberger, E. Talic, A. Schirrer
   Efficient simulation of railway pantograph/ catenary interaction using pantograph-fixed coordinates
   MATHMOD 2015 - 8th Vienna International Conference on Mathematical Modelling

4. J. Kopriva, J. Kunovsky, F. Kocina, V. Satek, E. Talic
   Numerical integration in the RNS
   The Proceedings of the 12th Conference Informatics'2013,
   ISBN: 978-80-8143-127-2, 5 S.

Emir Talic

Berufliche Erfahrung

11/2012–12/2015 **Projektassistent**, *TU Wien, Institut für Mechanik und Mechatronik*.
Industrieprojekt mit SIEMENS: Hardware-in-the-Loop Stromabnehmerprüfstand

- Entwicklung und Inbetriebnahme von Regelungsverfahren für verbessertes Stromabnehmerverhalten
- Entwicklung und Programmierung von Software zur Oberleitungssimulation
- Eigenständige Projektsteuerung und –überwachung
- Präsentation und Kommunikation der Projektergebnisse (Workshops, Konferenzen)

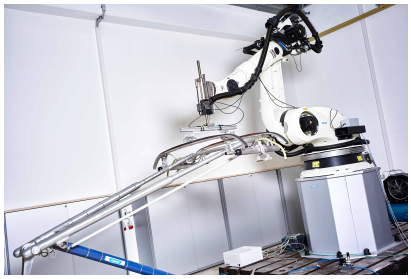

08/2009 **Praktikant**, *Verbund – Austrian Power Grid AG*.
Programmiertätigkeit in der UBM/Betriebsmanagement und Ökostrom

09/2007 **Praktikant**, *Wolek AG; Elektroinstallationen, Stark- und Schwachstromtechnik*.
Aufbau und Test von Sicherungskästen

08/2002& 07/2001 **Praktikant**, *Wolek AG; Elektroinstallationen, Stark- und Schwachstromtechnik*.
Elektroinstallationen

Studium und Ausbildung

05/2013–laufend **TU Wien, Doktoratsstudium**.
Dissertation: A real-time railway catenary model for Hardware-in-the-Loop tests
Voraussichtlicher Abschluss: Ende 2016

08/2010–04/2013 **TU Wien, Masterstudium Automatisierungstechnik**.
Masterarbeit: Simulation und Regelung eines Wärmetauschers

10/2006–07/2010 **TU Wien, Bachelorstudium Elektrotechnik**.

10/2005–06/2006 **Präsenzdienst**.

09/2000–06/2005 **HTL Wien 10, Ettenreichgasse**.
Fachrichtung: Elektronik, Spezialisierung: Technische Informatik
Abschlussarbeit: Laborarbeitsplatz zur digitalen Signalverarbeitung in programmierbarer Logik

Auszeichnungen

Houskapreis 2015, *Top 10 Nominierung*.
Eine integrierte Entwicklungsplattform für Pantographen-Stromabnehmer